The University of Manchester

Ultrafast charge dynamics in novel nanoparticles

A thesis submitted to The University of Manchester for the degree of Doctor of Philosophy in the Faculty of Engineering and Physical Sciences

2015

ALI AL-OTAIFY

The Photon Science Institute

School of Physics and Astronomy

Table of Contents

Word counts: 40739

Table of figures

List of abbreviations

CB	Conduction band
CBM	Conduction band minimum
CQDs	Colloidal quantum dots
CW	Continuous wave
DDT	Dodecanethiol
DHLA	Dihydrolipoic acid
EHP	Electron hole pair
ESA	Excited state absorption
FWHM	Full width at half maximum
IR	Infrared
LED	Light-emitting diodes
LSPR	Localized surface plasmon resonance
MEG	Multiple exciton generation
MPA	Mercaptopropionic acid
NC	Nanocrystal
NQD	Nanocrystal quantum dot
ND	Neutral density
NIR	Near infrared
NP	Nanoparticle
OPA	Optical parametric amplifier
PA	Photo-induced absorption
PL	Photoluminescence
PV	Photovoltaic
QD	Quantum dot
QDSCs	Quantum dot based solar cells
QY	Quantum yield
SHG	Second harmonic generation
TGA	Thioglycolic acid
UTA	Ultrafast transient absorption
UV	Ultraviolet
VB	Valance Band
VBM	Valance band maximum
WLC	White light continuum

Abstract

This thesis is entitled "Ultrafast charge dynamics in novel nanoparticles" and submitted by ALI AL-OTAIFY in May 2015 for the degree of Doctor of Philosophy at The University of Manchester.

The ultrafast charge dynamics in a number of nanostructured materials relevant to the production of renewable energy are investigated using ultrafast transient absorption spectroscopy. The materials include mercury telluride and cadmium mercury telluride quantum dots, and gold nanoparticles loaded on titanium dioxide colloidal spheres. The analysis of the resultant pump-induced transmittance change spectra and transients allow the determination of charge relaxation routes including multiple exciton generation, trion formation and direct-surface trapping.

The investigation of HgTe QDs passivated with thioglycerol, mercaptopropionic acid and dodecanethiol ligands suggests that mercaptopropionic acid ligand results in better passivation of HgTe QDs due to its carboxylic acid group. It allows more electron density donation to the QD surface to passivate the traps related with unsaturated Hg bonds and hence supresses the associated non-radiative processes. The decay lifetimes of the thioglycerol/dodecanethiol-capped QDs in addition to the photo-induced absorption feature in their spectra, are found to be consistent with surface charge trapping observed in CdSe QDs. In comparison, the transients obtained for mercaptopropionic acid passivated QDs coupled with the pump-induced transmittance change spectrum show no sign of any surface-related processes. Therefore, our analyses allow the determination of multiple exciton generation for the first time in these QDs with a quantum yield of 1.36 ± 0.04 when photo-exciting with photons of energy 3.1 times the band gap. Such result should turn researchers' attention to those ligands which could improve the QD solar cell field.

The study of exciton dynamics in $Cd_xHg_{(1-x)}Te$ alloy QDs is also presented here. Their pump-induced transmittance change spectrum show two bleaches: at the shoulder position of the steady state absorption and at the PL peak. The exciton dynamics of these materials are studied using four different wavelengths, two of them are above the MEG threshold. The resultant transmittance transients and the pump-induced transmittance change spectrum are free of any photo-induced absorption or long-lived surface trapping. Hence, the decay of the transients obtained above the MEG threshold for well-stirred samples at low pump fluences is attributed to biexciton recombination. The assessment of multiple exciton generation reveals a quantum yield value of 1.12 ± 0.01 when photo-exciting with 2.6 times the band gap.

Finally, the investigation of the recovery of the plasmon bleach in TiO_2 colloidal spheres decorated with different sizes of Au NPs is presented in this thesis. The pump-induced transmittance change spectra obtained for two different wavelengths show bleaches at the plasmon band maximum superimposed with two wings of absorption features at shorter and longer wavelengths. The resultant transmittance transients for these samples are well-described by bi-exponential decay with a very quick decline of a few ps associated with electron–phonon scattering, followed by a slower decay over a few 10s of ps associated with heat dissipation. Only the heat dissipation rate is found to be dependent on the size of the Au NPs as it rises from 49 ± 3 ps to 128 ± 6 ps when the diameter of the Au NPs is increased from 12.2 ± 2.2 nm to 24.5 ± 2.8 nm, respectively.

Declaration

No portion of the work referred to in the thesis has been submitted in support of an application for another degree or qualification of this or any other university or other institute of learning.

Copyright statement

List of publications and presentations

Journal articles

Ali Al-Otaify, Stephen V. Kershaw, Shuchi Gupta, Andrey L. Rogach, Guy Allan, Christophe Delerue and David. J. Binks, "*Multiple exciton generation and ultrafast exciton dynamics in HgTe colloidal quantum dots*". Physical Chemistry Chemical Physics, 2013. **15**(39): p. 16864-16873.

Ali Al-Otaify, Marina A. Leontiadou, Flavia V. E. dos Reis, Tatiana C. Damato, Pedro H. C. Camargo and David J. Binks, "*Size dependence of ultrafast charge dynamics in monodisperse Au nanoparticles supported on TiO2 colloidal spheres*". Physical Chemistry Chemical Physics, 2014. **16**(27): p. 14189-14194.

Conference presentations

Ali Al-Otaify, Stephen V. Kershaw, Guy Allan, Christophe Delerue and David. J. Binks, "*Ultrafast Transient Absorption Spectroscopy of HgTe Quantum Dots*", Photon12, Durham, UK, (3 - 6 September 2012).

Ali Al-Otaify, Stephen V. Kershaw and David. J. Binks, "*Ultrafast Transient Absorption Spectroscopy of mercury telluride Quantum Dots*", The 6th Saudi Scientific International Conference, London, UK, (14 - 16 October 2012).

Ali Al-Otaify, Marina A. Leontiadou, Pedro H. C. Camargo and David J. Binks, "*Size dependence of ultrafast charge dynamics in monodisperse Au nanoparticles on colloidal TiO2 spheres*" Photon14, Imperial College London, UK, (1 - 4 September 2014) [talk was given by Dr. Marina A. Leontiadou].

Ali Al-Otaify, Marina A. Leontiadou, Pedro H. C. Camargo and David J. Binks, "Ultrafast charge dynamics in monodisperse Au nanoparticles on colloidal TiO2spheres" Colloidal Quantum Dots and Nanocrystals, (CQDN14), University of Manchester, UK, (14 - 15 July 2014) [talk was given by Dr. Marina A. Leontiadou].

Conference posters

Ali Al-Otaify, Stephen V. Kershaw, Guy Allan, Christophe Delerue and David. J. Binks, *"Ultrafast Transient Absorption Spectroscopy of HgTe Quantum Dots"* IOP One-Day Quantum Dot Meeting, London, UK (5th January 2012).

Ali Al-Otaify, Stephen V. Kershaw, Shuchi Gupta, Andrey L. Rogach and David. J. Binks, "*Multiple Exciton Generation in HgTe Colloidal Quantum Dots*", E-MRS Spring Meeting, Strasbourg, France, (28- 30 May 2013).

Ali Al-Otaify, Marina A. Leontiadou, Stephen V. Kershaw and David. J. Binks, "*Ultrafast exciton dynamics in CdHgTe alloy Quantum Dots*", The 8th Saudi Scientific International Conference, Imperial College London, UK, (January 31 – February 1, 2015).

Book contribution

N. McElroy, M. Cadirci, **A. Al-Otaify**, R. Page, and D.J. Binks, "*Chapter 9: Increasing Efficiency with Multiple Exciton Generation*" In "Quantum Dot Solar Cells", 2014. **15**: p. 233-253.

Dedication and acknowledgements

Dedication

To my parents, my wife, my daughters, my siblings, and to everyone is waiting for this moment: I would like to say here is my thesis in your hands, my success is yours.

Acknowledgements

The writer is so grateful to his supervisor, Dr. David Binks, for his invaluable direction, support, advice and help throughout this work, for his special help in results interpretation and for the very important feedback he has given to the thesis.

The writer also wishes to acknowledge the help from all the group members and in particular Dr. Musa Cadirci, Dr. Marina Leontiadou and Daniel Espinbarro-Valesquez for all the valuable discussions and support. Dr. Darren Graham and Dr. Ben Spencer also deserve his thanks for their help in running the UTA experiment. He also would like to thank everyone involved in this successful study either by making samples for the study or for passing knowledge.

The writer sends special warm gratitude to whom without none of this would have been done as he feels speechless when it comes to thank them: his parents, his wife, his daughter and his siblings for all the great prayers, sensory and moral support.

Chapter 1 Introduction and background

1.1 Introduction

Today, the earth is home to more than 7 billion people, all of whom contribute to massive energy consumption (estimated to be about 410 exajoules in 2010 [1]). The sources of this energy are varied, and include expendable resources such as fossil fuels and nuclear power, and renewable energy sources, such as biofuels, solar energy, hydropower and wind power [2]. However, in 2011, fossil fuels accounted for an estimated 78.2% of the global total energy (see Figure 1.1), despite the risk of their exhaustion within decades [3]. Concerns about the limited amount of non-renewable resources remaining are recognised, and changes made accordingly resulted in a shift toward the use of renewable sources in 2012 by about 8.5%, when compared with 2011 [2]. However, the global population is rising, and this is coupled with an increase in per capita use energy, thereby necessitating an urgent search for alternative natural energy sources or improvements to the utilisation of existing renewables to guarantee the availability of sufficient energy to serve humankind in the future.

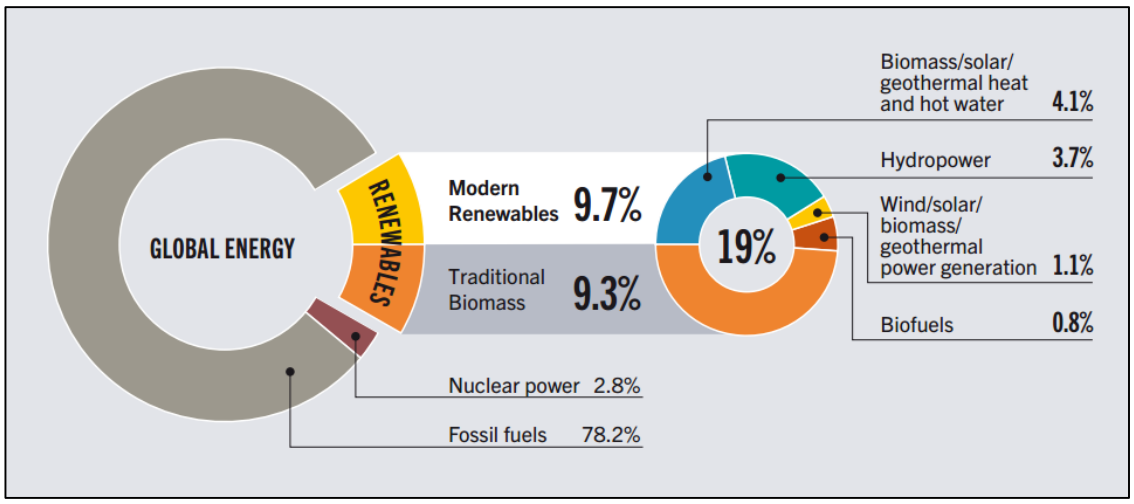

Figure 1.1 Estimation of energy consumption based on energy sources in 2011 (taken with permission from [2]).

Natural energy sources can be divided into stored energy (e.g. fossil and nuclear) and energy derived from solar radiation [3]. The latter is a clean, renewable, and abundant source, as every day the earth receives about 9×10^{22} J [4] with a spectrum covering the range from 0.5 to 3.5 eV (~355 to 2500 nm), as shown in Figure 1.2. This has motivated scientists to conduct extensive searches to exploit this energy, for example in solar cells and hydrogen production which are promising solutions with the potential to meet the future energy demand. Solar cells have an advantage over other fuel supplies, because they are environmentally friendly; however, for solar cells to compete economically with fossil or nuclear fuels they needs to be cheaper and/or more efficient. Solvent-based synthesised nanostructured materials have the potential to be both cheap and efficient. However, to realise this potential, the sub-nanosecond charge dynamics in nanostructures needs to be understood. This thesis will describe investigations into the sub-nanosecond charge dynamics of two such important types of nanostructured materials relevant to the production of renewable energy.

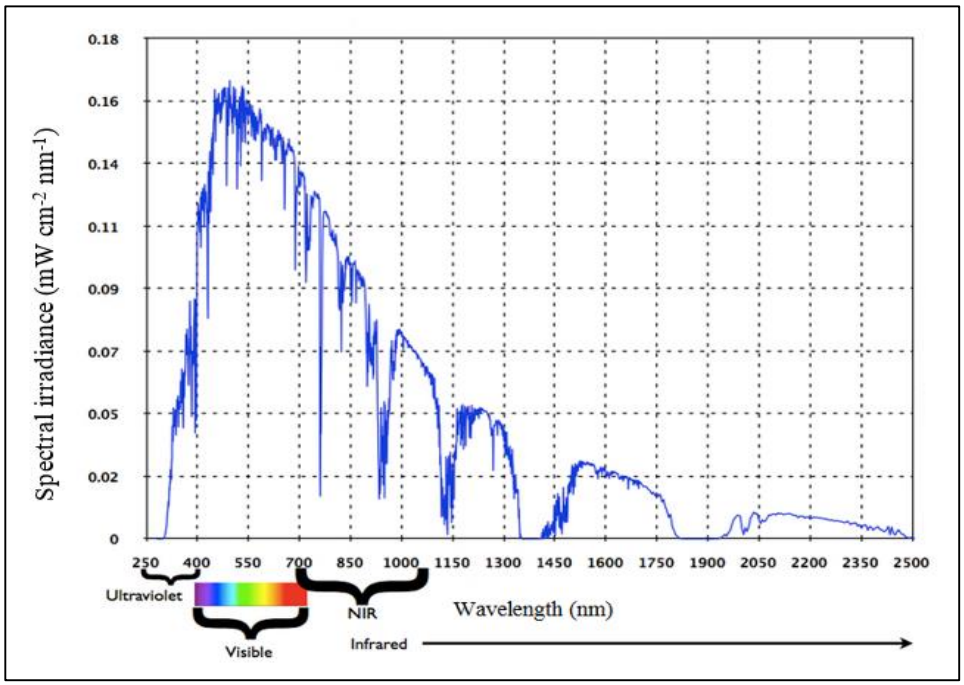

Figure 1.2 Solar irradiance spectrum (taken with permission from [5]).

To date, three generations of solar cells can be distinguished. The first generation were crystalline silicon (Si) solar cells, but these were very costly. The second generation of solar cells used were thin films and dye-sensitised, which reduced the cost, but these suffered from comparatively low efficiency [6]. The third generation, including quantum dot (QD) based solar cells [7], represent an attempt to reduce the cost of solar cells while simultaneously increasing efficiency. Figure 1.3 compares the cost and efficiency of all three generations of solar cells. Of the three generations described above, only third generation solar cells exceed the critical limit, known as the Shockley-Queisser limit, which describes the theoretical power conversion efficiency of a single p-n junction solar cell. This limit is based on the calculation of maximum generated photo-current to input power, according to four assumptions [8]. First, that the concentration used was 1 sun, and second, that the sun and the solar cell were both assumed to be blackbodies at temperatures of 6000 and 300 K, respectively. Third, that a semiconducting material can absorb photons with energy above its band gap, and hence, can generate charges while photons with energies below its band gap are not absorbed. The excess energy of an absorbed photon above the band gap raises the temperature of the charges in the semiconductor over the lattice temperature, where it is divided between electrons and holes according to their effective masses; more excess energy goes to the lower effective mass charge [9]. It should be noted that excess energy here is lost in the form of heat. Fourth, that the only loss in recombination is radiative loss. These assumptions allowed a value of ~31% for the Shockley-Queisser limit [8]. Hanna and Nozik [10] modified the detailed balance model used by Shockley and Queisser, by also taking into consideration carrier multiplication or the multiple exciton generation (MEG) effect which then led to an increase in the efficiency limit, to reach ~44%, at a band gap of 0.7 eV. The band gap of a semiconducting material is optimum for harvesting the solar spectrum if it has

an energy between 1 and 1.6 eV, and this point falls to lower values ~ (0.5 – 1.1 eV) in the presence of MEG [6].

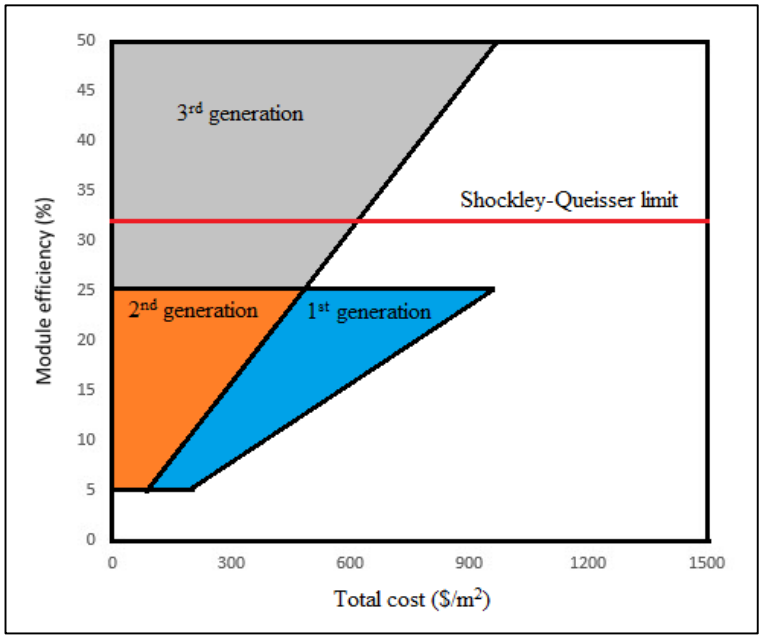

Figure 1.3 Comparison of the cost and efficiency of the three different generations of solar cells (modified from [6], Copyright (2009), with permission from Elsevier).

1.2 Background

1.2.1 Quantum dots

An object smaller than 100 nm in at least one dimension is usually classified as a nanoparticle (NP) [4]. It can be classified as either one, two or zero dimensional, and described as quantum wire, quantum well or thin film, or QD, respectively. When the size of the NP decreases further, quantum confinement might be observed, and we must then consider the QDs regimes. A QD is usually defined as an ultra-small particle of semiconductor crystal, with dimensions smaller than, or comparable with, the size of the exciton in the respective bulk material [11]. QDs lie between atomic-molecular and bulk materials, and are sometimes described as artificial atoms, and their energy levels as atomic-like. Figure 1.4 illustrates the change of density of states with energy for different dimensions of semiconductors from bulk to QD [12]. It should be noted that electron-hole

(eh) pairs in QDs are often termed excitons [13], even though they are not necessarily bound by their Coulomb interaction. Rather, confinement by the nanoscale of the QD leads to a particular electron being associated with a particular hole; for this reason, we sometimes use the term 'geminate charge'.

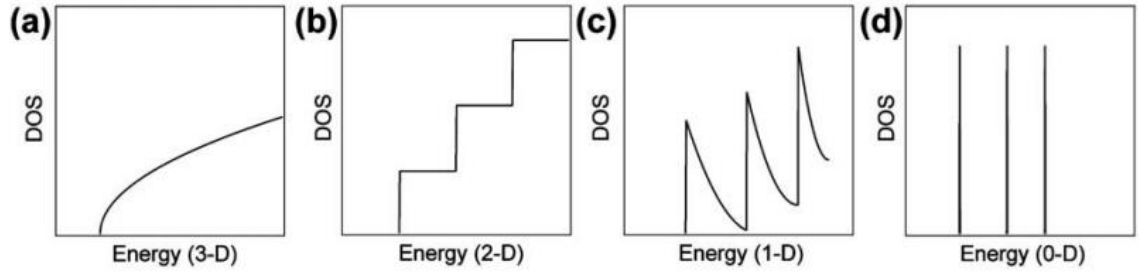

Figure 1.4 Illustration of the change of density of states (DOS) with energy in: (a) a bulk material, (b) a quantum well, (c) a nanowire, and (d) a quantum dot (Reproduced from [12] with permission of The Royal Society of Chemistry).

The characteristic distance between charges, known as the exciton Bohr radius (r_B), in a bulk semiconductor is defined as [4]:

$$r_B = \frac{\hbar^2 \varepsilon}{e^2}\left(\frac{1}{m_e} + \frac{1}{m_h}\right)$$

Equation 1.1

where ħ, ε, and m_e and m_h are the reduced Planck's constant, optical dielectric constant and the effective masses of the electron and hole respectively. However, in the quantum confinement regime, exciton motion is confined to a very small dimension, which results in discrete energy levels in comparison with the continuous bands in the respective bulk, as shown in Figure 1.5. It also results in the modification of the band gap, so it is size-dependant as follows [14]:

$$E_g^{QD} = E_g^{bulk} + \frac{h^2}{8R^2}\left(\frac{1}{m_e} + \frac{1}{m_h}\right) - \frac{1.8e^2}{4\pi\varepsilon_0\varepsilon R}$$

Equation 1.2

where E_g^{QD} is the band gap of the QD, E_g^{bulk} is the band gap of the bulk counterpart and R is the radius of the QD. The second term, on the right hand side of Equation 1.2 is the extra energy because of quantum confinement, which explains how the band gap energy changes with $1/R^2$; meanwhile, the third term shows Columbic interaction. The energy levels are classified using the principal quantum number (n=1, 2, 3 ...) and the angular momentum (L=0, 1, 2...), which has the corresponding names (s, p, d...) [11].

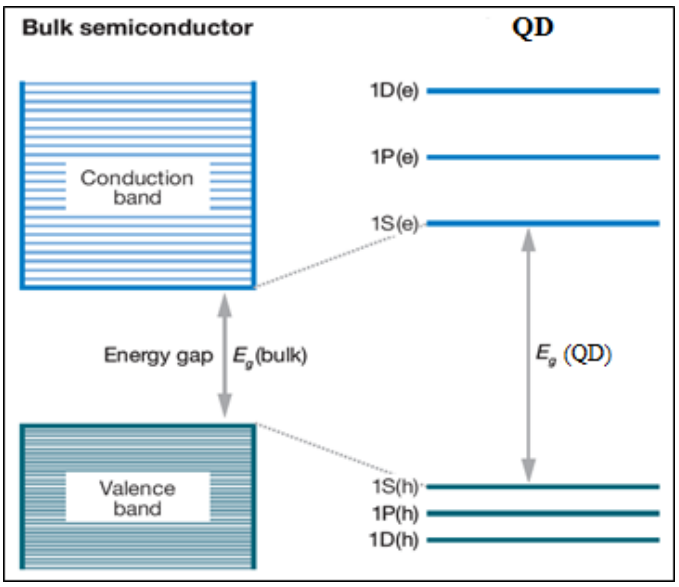

Figure 1.5 The valence and conduction bands in bulk and QD semiconductors. Discrete energy levels appear in the QD case and the bandgap expands [modified from [11]].

QDs have several applications; e.g. in light emitting diodes (LEDs) based on QDs [15], QDs lasers [16] and solar cells [4] (the application most relevant to this thesis). In a single junction bulk solar cell, efficiency is limited to the Shockley-Queissar conversion limit, because the energy in excess of the band gap is wasted as heat, via electron-phonon scattering, which is followed by phonon emission until the charges relax to their band edges. For example, up to 47% of the incident energy upon a single-junction of a bulk silicon cell is lost as heat [17]. Multi-junction solar cells can successfully overcome the Shockley-Queissar limit, because different p-n junctions of different materials are built on top of each other in layers, so that more wavelengths of the solar spectrum can be absorbed by the cell

(higher band gap materials absorb photons with higher energies, while lower band gap materials absorb photons of lower energies). Theoretically, efficiency can be increased up to 66%, but practically, efficiencies of 32% and 42.8% have been reported [18]. However, this technique is relatively expensive, and hence, attention has been directed toward impact ionisation for the enhancement of the photocurrent [19]. However, its rate has to be greater than all the other relaxation processes for hot charges.

QDs are useful in this matter for several reasons. Firstly, tuning the band gap of the QDs by changing their size allows one to build a multi-junction solar cell comprised of the same QD [20], but capable of absorbing a wide range of the solar spectrum covering UV, visible, and NIR, in some cases for exciton generation. Secondly, quantum confinement can reduce the relaxation rate of hot carriers [20]. Thirdly, it is possible, through the use of QDs, to create MEG [21], which increases the limits of theoretical efficiency as previously discussed. Fourthly, they show better stability and resistance to oxygen and UV radiation, compared to polymers, and fifthly their solution processability reduces fabrication costs [4]. Efficiencies as high as 6% for PbS [22] and 8.55% for ZnO/PbS [23] QD solar cells have been reported, and research is ongoing, due to the promise in this field.

QD's near–infrared (NIR) band gaps are unique because their absorption edge is specific and can be size-controlled to match the optimum spectral region for exploitation of the solar spectrum, approximately 900-1100nm [10]. This is optimum, because the maximum power conversion efficiency of a solar cell is given by [24]:

$$\eta = \frac{V_{oc} J_{sc} FF}{P_{in}}$$

Equation 1.3

where V_{oc} and J_{sc} are the open-circuit voltage and short-circuit current density, respectively, FF is the fill factor and P_{in} is the input solar intensity (typically 100 mW per cm^2). The

current was found to decrease when increasing the semiconductor band gap used, while the voltage could be increased by increasing the band gap [25], which then leads to an optimum value of efficiency for materials with an absorption edge in NIR at about 930 nm.

1.2.1.1 Relaxation dynamics and recombination in QDs

It is crucial to understand general charge dynamics in QDs before discussing the results of the research, and thus, here we briefly discuss these processes. Following the excitation of a QD, electrons and holes can be created with excess kinetic energy which is then lost by one of the following different paths [4]. First, it can be dissipated as heat via electron-phonon interactions, allowing the electrons to relax to the bottom of the conduction band and holes to relax to the top of the valence band. Secondly, an additional ehp can be created when the excess kinetic energy is at least equal to the band gap of the QD; this is a process known as carrier multiplication or MEG [4]. MEG happens via a process that is the inverse of the Auger recombination, in which the first exciton created relaxes to the band edges by transferring some of its energy to an electron in the valence band, promoting it to the conduction band; the fraction of the initial excess energy not used in the MEG process is lost by other processes, such as phonon emission. MEG is discussed in greater detail in section 1.2.1.2. Thirdly, Auger relaxation can also result when the excess energy is given to another charge, which could be the geminate; this charge can be later cooled by emitting phonons [4]. Relaxation can also occur by the transfer of energy to the vibrational modes of adsorbed ligands [26]. Surface states can also lead to non-radiative relaxation, as will be explained in section 1.2.1.3.

Charge recombination typically has a longer time scale than relaxation, with non-radiative recombination occurring over 10s of ps or longer, and radiative recombination characterised by lifetimes measured in nanoseconds. Non-radiative recombination processes include recombination via a surface state and Auger recombination. In Auger recombination,

an electron recombines with a hole, transferring the energy to a third charge (electron or a hole) in the process, which then loses its energy as heat [4]. Figure 1.6 illustrates some of the processes discussed above. Surface state relaxation and recombination are illustrated in Figure 1.8.

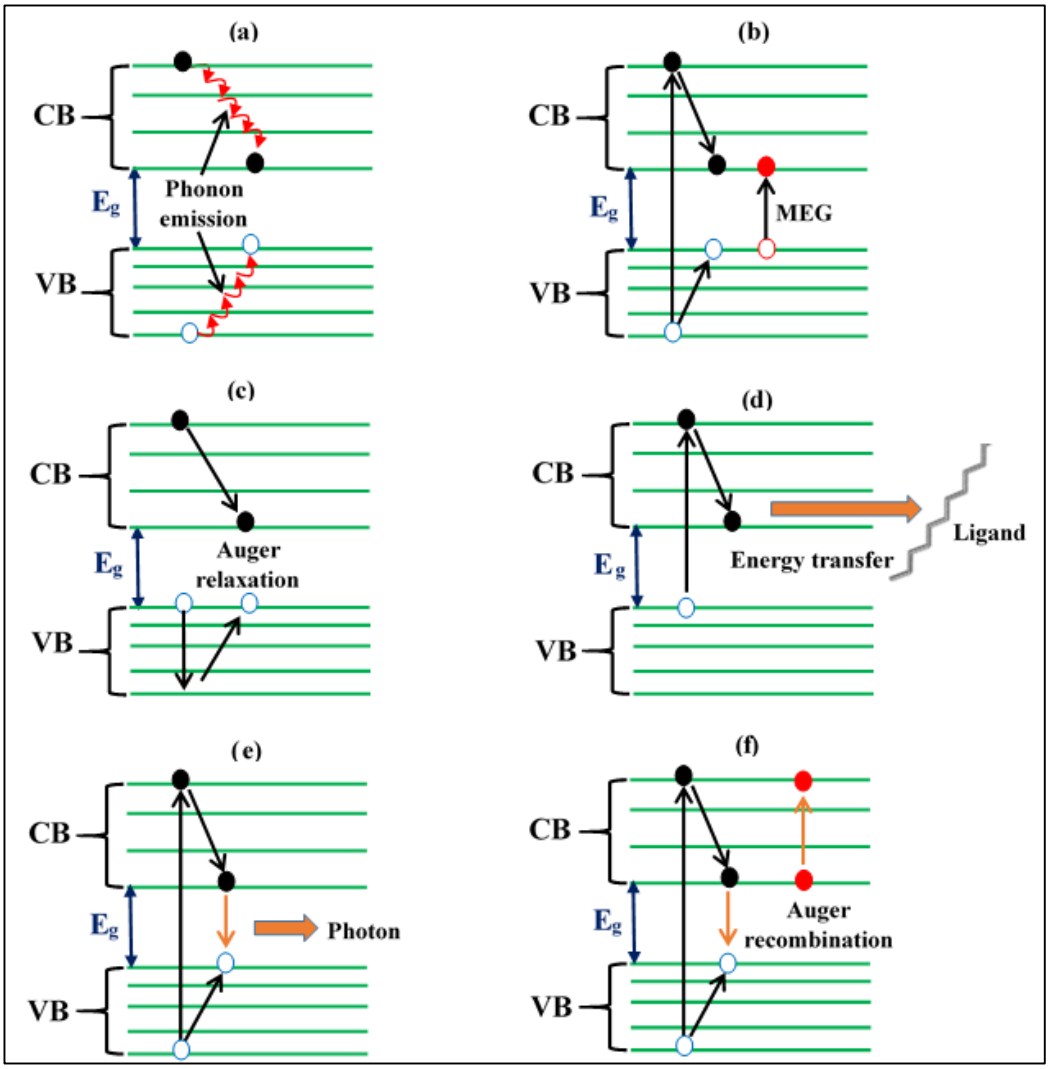

Figure 1.6 Schematic of some charge dynamic process in QDs showing (a) phonon emission, (b) MEG, (c) Auger relaxation, (d) energy transfer to the vibrational modes of ligands, (e) radiative emission of photons, and (f) Auger recombination. E_g is the band gap and VB and CB are the valence and conduction bands, respectively.

In bulk semiconductors, heat dissipation by phonon emission is very fast [19] and can occur in a few ps if the exciton density is less than 5×10^{17} cm^{-3}; when density is increased above 5×10^{18} cm^{-3}, the cooling time can be increased by a factor of two. However, the cooling time of hot carriers in QDs is relatively slow [18], especially at the low light

intensities that correspond to solar intensity on earth. That is due to the discrete energy levels, as the energy separation between them can be as high as several times the typical phonon energy. Characteristically, the energy levels in QDs are separated by about 100 meV and 30 meV in the conduction and valence bands, respectively; while phonon energy is usually about 30 meV [21]. Therefore, excited electrons in higher states can often only relax to the next lower level, by emitting several phonons, in order to satisfy energy conservation; a process called the "phonon bottleneck" [18].

Quantum confinement explains the prediction that hot charges would require multi-phonon processes when the separation between energy levels is greater than the phonon energy. The multi-phonon time was estimated using [20]:

$$\tau_c \sim w^{-1} \exp(\Delta E / kT)$$

Equation 1.4

where τ_c is the cooling time of hot charges, w is the phonon frequency, and ΔE is the energy separation between the energy levels. Note that ΔE > 0.2 eV for strong confinement, and then τ_c could be > 100 ps [20]. Experimentally, the cooling time of hot electrons in InP QDs was increased from 200-300 fs to 2-3 ps; i.e. about 10 times that when the Auger cooling channel was blocked, for example by extracting the holes immediately after generation [27]. Therefore, it is possible in principle to slow down hot electron cooling time in QDs, and when charge cooling time is increased then relaxation channels other than phonons, such as MEG, have a high probability of becoming dominant in QDs [18]. However, in this experiment the phonon bottleneck in QDs is a disputed issue, as some results support it [28] and others do not [29]. The confusion arises because, although the observed cooling time is relatively long, that is 10s of ps, compared with bulk semiconductors, it is not as long as theorised. However, Nozik [19] pointed out that the charge relaxation or cooling time (10s of ps) needs to be compared with the electron transfer time, for example from the conduction

band of GaAs to cobaltocenium redox acceptor ($Co(Cp)_2^+$) [30], (sub-ps to several ps), and hence, if the relaxation times are greater than 10 ps then it can be stated that the cooling of carriers in QDs has slowed sufficiently. Slow hot electron and hole cooling were both reported in the literature [20] ranging from 10 ps to 1 ns for electrons in InGaAs QDs and about 400 ps for holes. Furthermore, carrier relaxation for II-VI CdSe colloidal QDs has been reported, using intraband pump-probe spectroscopy to study the electron cooling dynamics from the 1P to the 1S states [28]. The cooling time was in the order of 200 ps and attributable to the phonon bottleneck. In determining the hot charge's relaxation time and bottleneck, it is important for the researcher to consider additional factors, including the concentration, the type of QDs and the surface chemistry, all of which affect dynamics in this field and could explain the controversy [20].

1.2.1.2 Multiple exciton generation (MEG) - phenomenology and underlying physics

As mentioned above, MEG is a process by which the excess energy of charges can be used completely or partially to generate an additional ehp, or even several, provided that the excess energy is at least equal to the band gap, i.e. each new ehp requires an energy equal to the band gap [17]. This is known as impact ionisation in bulk semiconductors, and was observed in the photocurrent of p-n junctions in Si and Ge in 1959 [31]. The quantum yield, i.e. the number of ehp generated was realised to exceed 1 when a photon, with energy of at least 3 eV was used. Impact ionisation was also observed in other bulk materials, such as InSb [32] and GaAs [33]. However, it has a low efficiency in general, because of its slow rate compared with electron-phonon scattering [34]. It is also limited to a narrow material choice, because the absorbed photon energy has to be much greater than the band gap of the bulk semiconductor; for instance, it has to be five times the band gap in bulk PbS [35]. Furthermore, it only becomes significant in Si when the energy of the incident photon rises

above 3.5 eV [36], which is beyond the energy levels of most photons that exist in the solar spectrum. Hence, impact ionisation in bulk semiconductors has not significantly improved photovoltaic cell efficiency [18]. However, interest in impact ionisation has been rekindled since the introduction of QDs, due to the reduced rate of phonon emission.

MEG can only occur at pump energies above a certain value, termed the MEG threshold ($h\upsilon_{th}$); it is dependent on the band gap of the material used, and is given by [37]

$$h\upsilon_{th} = E_g(2 + {m_e^*}/{m_h^*})$$

Equation 1.5

where h is Plank's constant, υ_{th} is the threshold optical frequency, E_g is the band gap energy, and m_e^* and m_h^* are the effective masses of the electron and the hole respectively. Equation 1.5 results from the conservation of energy and momentum [17] and how photon energy in excess of the band gap is divided between charges. MEG is usually detected by ultrafast transient absorption spectroscopy (UTA) (see Chapter 2 for more information).

Beard *et al*. [38] defined the efficiency for MEG (η_{exc}) as the band gap divided by the energy required for generating a new exciton above the MEG threshold (E_{exc}) i.e., we can write $\eta_{exc} = E_g/E_{exc}$ but also conservation of energy must be satisfied. That means the number of excitons generated multiplied by their energy cannot exceed the absorbed energy by photons $N(exc)E_{exc} \leq h\upsilon N_{photons}$. Note that some of the absorbed photon energy is converted to charge excess energy and is lost as heat unless if it is at least equal to E_{exc} then a new exciton can be generated. In an ideal case $E_{exc} = E_g$, the energy loss is zero and therefore $\eta_{exc} = 1$. Hence, if the absorbed photon has an energy of $2E_g$ then two excitons can be generated while if it is 3 then the generated excitons are three. However, in between $2E_g$ and $3E_g$ only 2 excitons can be created and the rest of the energy is considered as an excess energy (could be wasted as heat). Therefore, the energy loss is $E_{loss} = h\upsilon - mE_g$

where m is defined as the number of created excitons and so at the case of $E_{loss} = 0$ then $QY = m = h\upsilon/E_g$ [38].

In contrast, a nonideal case means $E_{exc} > E_g$ and therefore $\eta_{exc} < 1$ giving the energy loss this expression [38]

$$E_{loss} = h\upsilon - [E_g + (m-1)E_{exc}]$$

Equation 1.6

Solving Equation 1.6 at $E_{loss} = 0$ when considering $E_{exc} = E_g/\eta_{exc}$ allows the determination of the quantum yield as [38]

$$QY = m = \left[\left(\frac{h\upsilon}{E_g} - 1\right)\eta_{exc}\right] + 1$$

Equation 1.7

But we know that MEG occurs at energies above photon threshold $h\upsilon_{th}$ and its QY increases linearly above it. If $E_{loss} = h\upsilon_{th} - E_g = E_g/\eta_{exc}$, then solving Equation 1.6 gives the QY the following expression [38]

$$QY = \left(\frac{h\upsilon}{E_g} - 1\right)\eta_{exc}$$

Equation 1.8

Equation 1.8 tells us that the efficiency is extracted from plotting QY against ($h\upsilon/E_g$) and solving it gives the relationship between $h\upsilon_{th}$ and η_{exc} as [38].

$$h\upsilon_{th} = E_g + E_g/\eta_{exc}$$

Equation 1.9

Here we see that the efficiency can be increased by reducing the threshold [17].

Debate is ongoing regarding what is more efficient; impact ionisation in bulk semiconductors, or MEG in QDs made of the same material. When QY was measured against $h\upsilon$, bulk PbSe [39] showed more efficient carrier multiplication than QDs. However,

that study ignored the effect of the band gap, as it varies when tuning the size in QDs and is always greater than that of its bulk counterpart, hence QY should be plotted against (hv/E_g) rather than hv. This strategy allowed Beard *et al*. [38] to compare QDs with bulk cases, considering PbSe as an example. They found that the efficiency of the bulk case was 0.19, which improved to 0.41 for the QDs. Moreover, they found the threshold had decreased from $4.2E_g$, for the bulk to be $2.7E_g$ for the QDs. Delerue *et al.* [40] also claimed the enhancement of efficiency in QDs, when compared to the bulk of PbSe.

Regarding theoretical models that have described MEG, they include impact ionisation, biexciton creation via a virtual exciton or biexciton and direct multi-exciton creation [17]. Figure 1.7 illustrates these models when only two excitons are formed. Impact ionisation, which is considered to be the most popular route to produce MEG, is based on passing the excess energy of an exciton initially generated by a single photon to an electron in the valence band which then jumps to the conduction band forming another exciton.

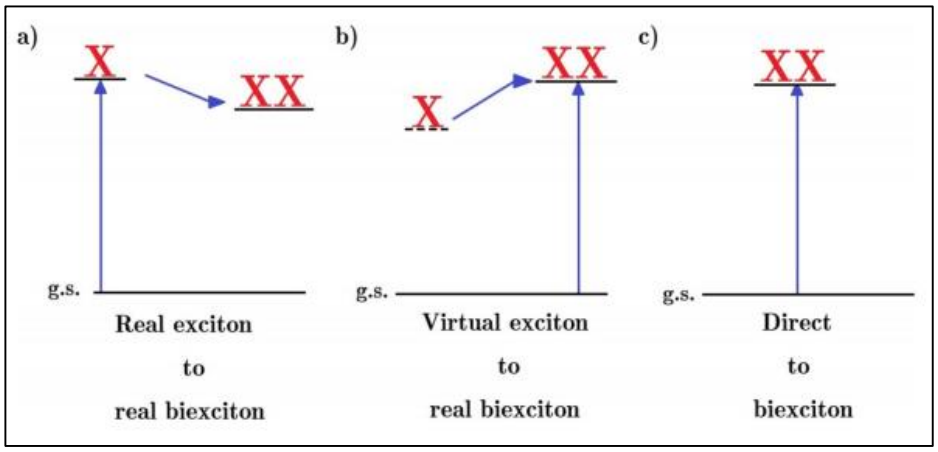

Figure 1.7 The formation of biexciton from absorption of a single photon via: a) impact ionisation, b) biexciton formation via a virtual exciton or biexciton states; and c) a superposition of multi-excitons quantum states (taken from [17]).

MEG creation through virtual electron states was proposed for the first time in CdSe and PbSe nanocrystals (NCs) [41] which can contribute to the overall QY. Two years later a study [42] suggested that MEG by a single photon can be obtained via the generation of a

virtual biexciton in intraband transitions which then is converted to a real biexciton. They claimed that the efficiency by this process can be equivalent to or even better than the efficiency of impact ionisation. However, a recent study [43] in bulk and nanocrystalline PbSe and PbS reduced the photogeneration process to impact ionisation because of the complete lack of interference between it and the virtual channels. MEG was also suggested to be produced theoretically by a single photon through a coherent superposition of single and multi-exciton channels generated by quantum confinement in 2006 [44]. Such a process can contribute to the overall MEG QY however as mentioned earlier, this is contradicted with the study suggesting that interference between the pathways is neglected. Another study [45] based on crystalline and bulk PbSe also concluded that it has a weak contribution to the QY and impact ionisation is the dominant process.

Tight-binding calculations were used by Allan and Delerue to assess carrier multiplication in a number of materials. They succeeded to obtain the same measured efficiency of carrier multiplication in bulk PbSe and PbS [39]. Their simulations also explained successfully the efficient MEG observed for low photon energy in PbSe NCs [46]. The calculations were also applied successfully for InAs nanocrystal quantum dots (NQDs) [47] Si NCs [48] and α-Sn QDs [49] and finally were used to assess MEG measurements in HgTe QDs concluding that the theory agrees excellently with experimental results [50] (see Chapter 3).

1.2.1.3 Sub-nanosecond trap-related charge dynamics

All multi-excitons created by the pump (either directly by multi-photon absorption or via MEG) decay to a single exciton on a time-scale of 10s of ps [17] by a process of Auger recombination, that cannot occur for single-excitons because of the need for a third charge to receive the liberated energy. However, such a decay time is not only obtained for multi-exciton recombination but also by two other processes: trion formation, sometimes known

as photocharging, and direct surface-trapping [17]. In trion formation, a charge (electron or hole) is trapped on the surface of the QD after photoexcitation by the pump for a period exceeding that between successive pump pulses. During this time, the geminate charge (hole or electron) is still in the QD, and thus, when a subsequent pulse of the pump generates a new exciton it may then recombine by an Auger process, liberating its energy to the unpaired charge in the QD created by the previous pulse. This Auger recombination process produces a bleach decay with a ps lifetime at low fluence, which thus might then be mistaken for MEG, which can also happen at low pump fluences [17]. However, researchers [51-53] have found that vigorously stirring or flowing the sample can sweep out the initially excited QDs from the excitation volume before the arrival of the subsequent pump pulse. This can prevent double excitation of the same QD [54] and consequently the production of trions, which avoids overestimation of the MEG quantum yield (QY). Figure 1.8 (a) shows a schematic of trion formation.

Another process that can be mistaken for MEG is direct surface-trapping. Here the surface of the QD becomes a route for exciton recombination, resulting in the electron population of the conduction band minimum (CBM) decaying on a ps time-scale for low pump fluences, again mimicking MEG [17]. However, direct surface-trapping can be distinguished from MEG by two features. It usually coincides with a broad photo-induced absorption near the 1S transition, and also the decay transients, are usually non-monoexponential in form [55]. Unlike trion recombination, this process cannot be eliminated by stirring or flowing the sample, but careful passivation of the sample surface was found to be an effective method to eliminate this type of trapping. The surface-trapping process explains why a study seemed to show MEG with a QY of 170% using a pump wavelength with energy below the MEG threshold [55]. Figure 1.8 (b) illustrates surface-trapping of cold and hot electrons.

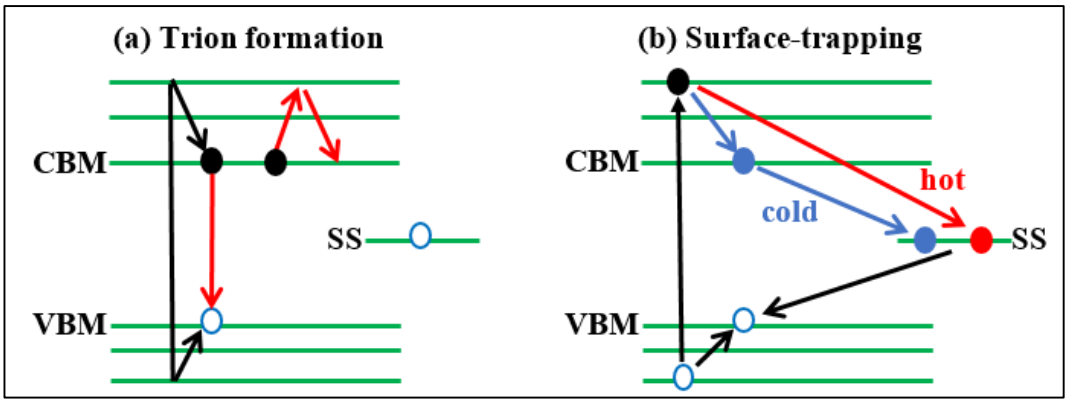

Figure 1.8 Schematic of (a) Trion formation (here a negative trion is shown but positive trions can also form when an electron is instead trapped on the surface), and (b) Surface-trapping in its two types - cold and hot; also shown is surface state recombination. Note that the filled circles represent electrons, while the empty ones represent holes, VBM (valence band maximum), CBM (conduction band minimun), and SS (surface state).

1.2.2 TiO_2-Au system

In addition to directly generated electricity, clean and renewable fuels can be produced using sunlight. For instance, hydrogen can be made by 'water-splitting', i.e. photolysis of H_2O by solar photons using a photocatalyst. Titanium dioxide (TiO_2) is a common photocatalyst among semiconductors [56], and solar water splitting using an electrode of TiO_2 has been considered an effective technique to generate clean hydrogen energy since 1972 [57]. The principle is based on initially absorbing photons with energy equal to, or higher than, the TiO_2 band gap, to generate ehp. The electrons and holes created then induce the splitting of water into hydrogen (H_2) and oxygen (O_2) gas. To initiate the water splitting reaction, the CB and the VB levels of the photocatalyst have to be favourable for producing hydrogen and oxygen respectively [56], and this is the case in TiO_2 as shown in Figure 1.9. Only a very low percentage of photo-generated charges (less than 5%) reach the TiO_2 surface before recombination, and these separated electrons and holes are respectively responsible for the reduction and oxidation process to the reactants that the TiO_2 adsorbs. Figure 1.9 shows the principle of hydrogen production (water splitting) by TiO_2 photocatalysis.

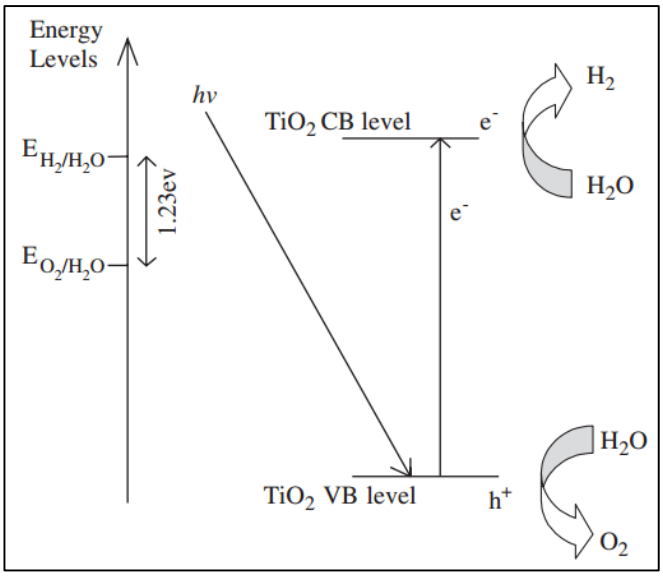

Figure 1.9 The principle of hydrogen production (water splitting) by TiO_2 photocatalysis (Reprinted from [56], Copyright (2006), with permission from Elsevier). E_{H_2/H_2O} and E_{O_2/H_2O} are hydrogen production level and oxidation level, respectively.

TiO_2 has largely suitable optical and electronic properties, good stability and low cost [58] resulting in it being widely studied as a photocatalyst for the water splitting reaction and in the development of dye sensitised solar cells [59, 60]. However, it has two significant drawbacks: a large band gap (3.23eV (385nm) for bulk anatase TiO_2 [61]), which demands UV light for photo-excitation, and high recombination rates of the photo-created ehp, which limits its photocatalytic and photovoltaic performances [58]. However, both of these can be improved by decorating its surface with noble metal nanoparticles (NPs). These NPs have Fermi levels lower than that of TiO_2, i.e., they can trap photo-generated electrons in the TiO_2, leading to the separation of electrons from holes, thereby improving the quantum yield [62]. Furthermore, some metals, such as silver and gold, support localised surface plasmon resonance (LSPR) in the visible region of the spectrum, enabling the enhancement of charge formation due to plasmonic effects [63]. When light interacts with metals it stimulates delocalised electrons near the surface into oscillation, with the Coulomb attraction between the electrons and the parent nuclei acting as the restoring force. This phenomenon is known as a surface plasmon and has a resonance that occurs when the light frequency matches the

natural frequency of the surface electrons [64]. When the wavelength of light is greater than the metal NP diameter then this collective electron oscillation is confined, and is known as a localised surface plasmon. The electric field near the surface of the NP can be greatly enhanced by this effect, particular at resonance which for noble metal nanoparticles occurs in the visible part of the spectrum [65].

1.3 Literature review

1.3.1 Brief history of QDs

The large number of publications in the last 25 years reflect the high interest in QDs. The synthesis of QDs started in the 1980s [54] with CdS in aqueous solution stabilised with polymers or surfactant [66]. This was improved by the discovery of a synthesis route for high quality mono-dispersed colloidal quantum dots (CQDs) published in 1993 for CdS, CdSe and CdTe in an organic solvent using coordinating ligands [67]. Within that time, a hot-injection method was used to synthesis narrow size distributed QDs [68]. Later on, passivation of QD surfaces with inorganic semiconductors was established in 1995 for CdSe capped with ZnS [69] as an efficient way to improve both stability and luminescence. The surface passivation was found to eliminate charges from trapping into surface states and reduce photo-oxidation [54]. Core/shell synthesis is achieved by three steps: core synthesis, purification and shell growth. A simpler synthesis technique was developed to avoid the purification step in the middle and used for the synthesis of CdSe/ZnSe and other QDs. Next, a precise technique to control the shell thickness was used in 2003 to synthesis CdSe/CdS [70]. Since then many studies and synthesis based on a variety of core only or core/shell semiconductor QDs were published in the last 20 years considering chemicals with low cost and toxicity.

Intensive work has been performed on a number of NIR QDs, of particular interest as the absorbers of light in solar cells, including PbX (X=S, Se, and Te) [19, 71, 72], InAs [73] and HgTe [74]. In the literature on the HgTe QDs, several potential applications are discussed such as being emitters at telecommunications wavelengths [75] and as the absorbing species in photodetectors and photovoltaic devices [76]. However, prior to this study, no experimental work on MEG in HgTe QDs, or any semimetal QD has been conducted. Moreover, MEG measurements demand a full understanding of multi-exciton dynamics and interactions if they are to be properly interpreted [77], and these too had yet to be carried out before this study.

In the literature, Yang *et al.* [78] reported using CdHgTe nanocrystals in combination with CdTe QDs to fabricate QD solar cells. They achieved energy conversion efficiency rates of 1.0% and 2.2% for $(CdHgTe)_3$ and $(CdHgTe)_3$-$(CdTe)_2$, respectively. Prior to commencing the study of CdHgTe alloy QDs described in this thesis, no one had studied ultrafast exciton dynamics for this material including MEG; however, just before we completed the study one appeared. Kershaw *et al.* [79] investigated MEG in 3.75 nm diameter $Cd_xHg_{(1-x)}Te$ alloy QDs with different compositions and different band gaps between 1.35 and 1.60 eV using a transient grating pump-probe experiment. MEG quantum yield measurements showed dependency upon composition, revealing the best quantum yield of 199 ± 19% for a composition x = 0.52/0.62 when using a pump energy equivalent to 3 times the band gap. They also calculated the MEG threshold as 2.15 times the band gap. Thus, in Chapter 4 we compare our results with theirs.

1.3.2 History of MEG

The history of MEG in QDs dates to 2001, when Nozik [20] suggested MEG as a means to increase photovoltaic cell efficiency. Three years later, Schaller and Klimov [80]

observed MEG experimentally for the first time in QDs. They used a UTA experiment to examine exciton dynamics in ~ 4-6 nm size PbSe QDs, and found a QY of 218% when pumping at $3.8E_g$. PbSe QDs are attractive for MEG studies, because of their small bulk band gap (0.28 eV [37]), allowing size-tuning of the QD absorption edge for optimum exploitation of the solar spectrum. For this reason, they are the most popular type of QD in terms of the number of studies [17]. In 2005, Ellingson *et al.* [71] confirmed the observation of MEG in PbSe QDs, reporting a QY of 300% for photoexcitation with an energy of $4E_g$. They also observed MEG for the first time for PbS QDs with an efficiency similar to that of PbSe QDs. Shortly thereafter, Schaller *et al.* [81] compared MEG measurements for CdSe QDs with PbSe QDs, reporting a better MEG threshold for CdSe of ~ $2.5E_g$ and QY of ~ 165% at $3.1E_g$ in contrast with ~ $2.9E_g$ for PbSe and QY of ~ 700% at $8E_g$. Although, Cd-based QDs have too large a band gap compared to the optimum for exploitation of the solar spectrum [17], the way in which they are synthesised is well-controlled making them a useful model system for the study of MEG and associated processes. A low MEG threshold of $2.5E_g$ and $2.65E_g$ has also been reported for CdTe QDs [82] and CdTe/CdSe core/shell system [83], respectively. The observation of MEG in PbTe QDs has also been claimed [72], with a QY of up to 300% at $4E_g$ reported. InAs QDs are attractive for MEG studies for two reasons: a low band gap in bulk cases, allowing the tuning of the size of the QDs to be optimum for exploitation of the solar spectrum, and a low expected MEG threshold. Since m_e^* is very small in InAs QDs compared to m_h^*, Equation 1.5 gives hv_{th} a value of ~$2E_g$ [17]. In 2006, MEG was reported for InAs QDs [84] with QY of 160% at $2.7E_g$ and then a year later the MEG threshold was found to be as low as $2E_g$ [73]. It is not surprising to find MEG studies of Si QDs, because Si itself is a well-known semiconductor used in conventional solar cells. For the first time, in 2007, 9.5 nm Si QDs with a 1.2 eV band gap

were studied for MEG [85]. They showed a threshold of 2.4 ± 0.1E_g and a QY of 2.6 ± 0.2, using a wavelength of 3.4E_g.

However, all the above studies were conducted before the establishment of other processes that can be mistaken for MEG measurements (as discussed in section 1.2.1.3). 2007 was a critical year in MEG studies, as this was when the artefacts in MEG started to become well-known. Following reports that confirmed the occurrence of MEG in some materials, later reports [86] showed some discrepancy. For example, CdSe and CdTe QDs showed no evidence of MEG, even with photon energy greater than 3E_g. Theoretical calculations [87] linked this inconsistency to the possibility of surface trapping. Similarly, Pijpers *et al.* [88] failed to reproduce MEG in InAs QDs that they already reported in ref. [84], and a study in InAs/CdSe/ZnSe core/shell1/shell2 [89] failed to observe any sign of MEG when exciting photon energies up to 3.7E_g. Discrepancy in the results reported for InAs QDs led Califano [90] to suggest observations were not necessarily of MEG; this phenomenon was later referred to as the existence of surface-trapping in InAs/ZnSe QDs [47], as no sign of MEG was found for photon energies up to 3.2E_g.

Although MEG occurrence cannot be confidently concluded on the basis of studies in the period from 2004 to 2007 (as artefacts could influence them), they were nonetheless crucial studies advancing the field. MEG measurements have since taken a further step toward certainty, as they now take into consideration both trion recombination and surface-trapping. Reports began with a stirred sample of PbSe QDs [77], which showed a threshold of MEG below 3E_g and a QY of 245% using photon energy of ~ 7E_g. In 2010, Midgett *et al.* [53] studied two sizes of PbSe QDs 4.6 and 6.6 nm. The QY of the small QDs was 1.2±0.1 at 3.7E_g and 1.55±0.05 at 4.5E_g, while it was 1.61±0.05 for the 6.6 nm QDs at 4.7E_g. Another material studied for MEG was InP QDs, not because of their band gap (1.7-2.0 eV) but due to the expected low MEG threshold [17], similar to InAs. In 2009, InP/ZnS/ZnO

core/shell1/shell2 system [91] was examined for its MEG characterisation, resulting in the lowest reported threshold after trion recombination and surface-trapping were identified with a value of (2.1±0.2)E_g and creation of 1.18±0.03 excitons per absorbed photon of energy equal to 2.6E_g. MEG was also examined in a stirred sample of PbS QDs [52] and found to have a threshold of (2.5±0.2)E_g. To date, none of the materials studied for MEG have shown optimum efficiency, which is the goal of seeking the best candidate in this field.

1.3.3 Brief overview about TiO_2-Au

TiO_2 as a photocatalyst for hydrogen production dates back to 1972 [92], when it was used as a photoanode photoexcited with UV light faced by platinum (Pt) metal as a cathode. This was found to make water electrolysis happen at lower voltages compared to electrolysis without the TiO_2. Five years later, a small amount of Pt was loaded on to the surface of TiO_2 which lead to separation of the created photogenerated eh pairs, with electrons moving to the metal to induce reduction and holes staying in the TiO_2 and inducing oxidation at its surface. Since then, research has focused on eh separation and for more than 20 years researchers used different metals to examine the change in the photocatalytic properties of titanium dioxide [59]. Several reviews have discussed the development of this topic [92-94].

In 1995, UV radiation was used to excite TiO_2 loaded with various Au NPs for producing hydrogen from a water–ethanol solution [95]. Photogenerated electrons are trapped by the Au NPs, enhancing charge separation and thus hydrogen gas productions. Researchers have found that the size of the gold NP affects the catalytic activity of TiO_2, with 2-5 nm size producing better results [59]. The reduction efficiency of the TiO_2-Au system with C_{60} acting as an electron acceptor was measured as a function of the Au NP size. The yield of C_{60}^- was found to increase with decreasing size of the Au NPs, indicating a

greater shift in the Fermi level after photoexcitation, 8, 5 and 3 nm sizes were used with -20 mV shift achieved for 8 nm size while 3 nm resulted in -60 mV shift [59].

A recent study used ultrafast transient absorption spectroscopy to test the electron injection dynamics of gold NPs to the conduction band of TiO_2 films probing at 3440 nm [96]. They conducted their study using a series of pump wavelengths from 400 to 680 nm and found two different paths of electron injection: the first of which occurs at wavelengths < 500 nm and can be attributed to interband exciton generation in the gold NPs. The second dominates at wavelengths > 580 nm and relates to the enhancement of the electric field by the plasmon resonance. Interestingly, they claimed that interband transition from the d-band to the sp-band in gold overlaps with the plasmon band in the range between ~400 to ~550 nm (the peak of the plasmon band) while the overlap disappears in wavelengths above the plasmon band. The literature reports excitation of gold NPs by a 400 nm pump beam and probing of plasmon resonance, resulting in the broadening of the surface plasmon band, which occurred as a bleach at the plasmon band maximum, superimposed with two wings of absorption features at shorter and longer wavelengths [97, 98].

1.4 Thesis motivation

The overall efficiency of solar cells and hydrogen production devices can depend on the sub-nanosecond dynamics of photo-created charges within the material being used, and this is the subject of this thesis. This research can be divided into two main parts: a study of QDs with applications in solar cells and TiO_2Au systems relevant to hydrogen production devices. Each part has a particular motivation, and hence will be discussed individually, starting with HgTe QDs and the semimetals family and the importance of studying them. Then, in relation to the second part of the study, the TiO_2Au system will be discussed.

1.4.1.1 Why HgTe QDs?

Firstly, bulk HgTe is a semimetal with a small negative bandgap of -0.15 eV [76]. The negative band gap of semimetals, such as HgTe or alpha-tin (α-Sn), corresponds to a very small overlap between the valence and conduction bands [99]. The Bohr exciton radius of HgTe is 40 nm [100], about 10 times larger than that of silicon [101] which means that HgTe QDs of a few nm in diameter are well within the strong confinement regime. Consequently, quantum confinement causes a strong size-dependent increase in the effective band gap, moving it towards an increasingly positive one, as the size of the QD decreases [102]. Thus, the band edge of these QDs is dominated almost entirely by confinement energy (see Equation 1.2), which allows tuning of the band edge across the NIR and hence to be optimized for efficient exploitation of the solar spectrum [74].

Furthermore, a recent theoretical study predicted MEG would be particularly efficient in semimetal QDs [49], making them particularly well-suited for quantum dot based solar cells (QDSCs), as the additional ehp formed by MEG can contribute to the photocurrent and thereby improve the efficiency of the solar cell. This study was mainly concerned with determining which semiconductor material would produce the highest MEG efficiency when in the form of a QD. The research calculated the rate of impact ionisation (the process underlying MEG), and determined the quantum yield of MEG by comparing the lifetime of impact ionisation to that of phonon emission. It revealed that the lifetime of impact ionisation reduced dramatically faster with increasing excitation energy in QDs than in the bulk material (see Figure 1.10). This behaviour was attributed to the much more rapid increase in the density of states as the excitation energy is increased for QDs than for bulk, allowing the increased Coulomb interaction in QDs to become effective. Using this approach, the study compared the carrier multiplication threshold theoretically and experimentally in PbSe and PbS QDs with bulk Si, and linked the better efficiency of QDs to the small band gaps (0.28

and 0.42 eV for PbSe and PbS, respectively) and to the high degeneracy of the band edges [49].

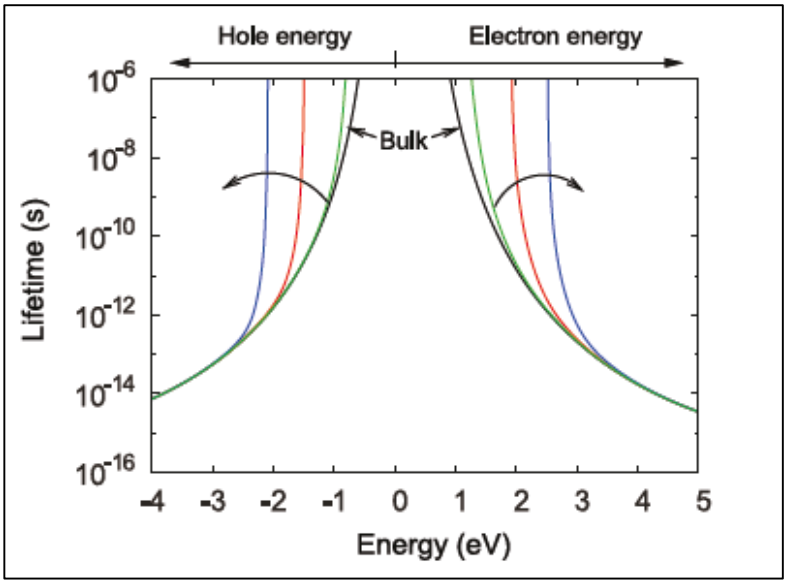

Figure 1.10 Impact ionisation lifetime compared to the energy of the photoexcited carriers for PbS. Arrows indicate the decrease in size of the QDs and consequent increase in the band gap "Reprinted with permission from [49]. Copyright (2011) American Chemical Society."

The authors concluded that to improve the efficiency of MEG, the chosen QDs should be among those materials with band gaps smaller than bulk PbSe and PbS, i.e. close to a zero band gap, such as semimetals [49]. If semimetals are used then the blue curve in Figure 1.10 representing small QDs, which have a long lifetime, can be shifted toward zero, and in particular to the optimum for exploitation of the solar spectrum. The study chose α-Sn as a candidate for semimetals, and calculated its MEG quantum yield versus photon energy for different sizes of QDs, as shown in Figure 1.11. The sharp peaks observed in the quantum yield can be attributed to the high rates of impact ionisation. These peaks were not observed in similar calculated spectra for PbSe, PbS, Si and InAs QDs, giving the α-Sn an advantage over them [49]. Figure 1.11 shows that decreasing the α-Sn QDs band gap resulted in a decrease in the MEG threshold scaling as ($h\upsilon_{th} \approx 2.15E_g$), which is very close to the ideal threshold of $2E_g$ and also highlights the importance and benefits of semimetals or zero band

gap materials in achieving a small MEG threshold. In the study, the lifetime of impact ionisation was found to be smaller than the assumed phonon lifetime, i.e. 1 ps for energies ranging from 2 to 4 eV, and even lower than 2 eV for QDs sized 3.6 nm or greater. This means the rate of impact ionisation is higher, allowing carrier multiplication to be preferred over phonon emission [49]. Furthermore, the low MEG threshold in α-Sn QDs results in high energy efficiency (the ratio between the number of excitons created to normalise photon energy to the band gap), which remains above 38% in comparison to a maximum value of only 25% for PbSe and PbS QDs [49].

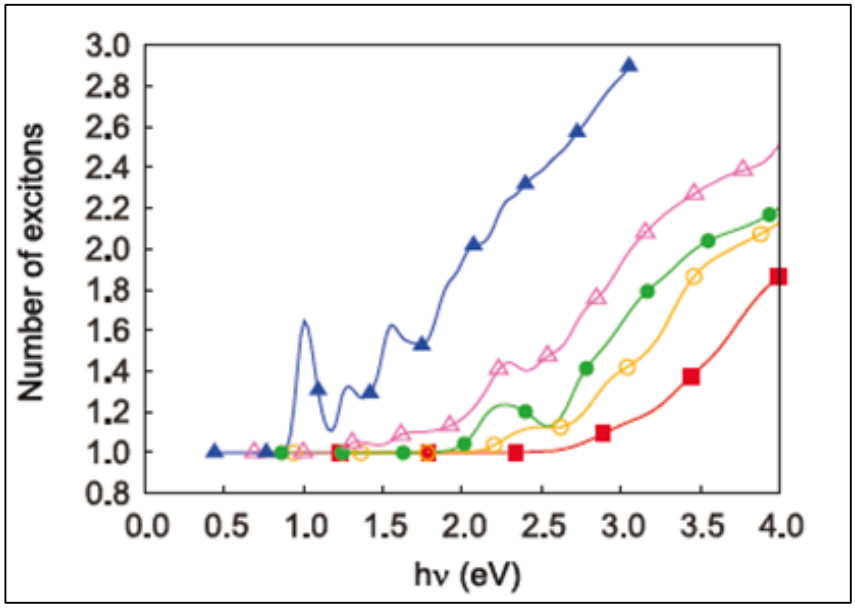

Figure 1.11 Quantum yield (number of excitons created per absorbed photon) for different QDs sizes, corresponding to E_g=0.44 eV (filled triangles), E_g=0.69 eV (open triangles), E_g=0.86 eV (filled circles), E_g=0.94 eV (open circles), and E_g=1.24 eV (filled squares). "Reprinted with permission from [49]. Copyright (2011) American Chemical Society."

Another aspect of this study concerns the effect of the ligands used to passivate the HgTe QD surfaces. Small-sized QDs of a few nm in diameter can form a significant number of surface trap states, due to the large surface-to-volume ratio [103]. The nature of these trap states derives from the unsaturated bonds on their surfaces [104]. These traps open a route for non-radiative relaxation and recombination, which might prevent MEG from being the dominant relaxation route. Ligand passivation is an established technique used to suppress

such trap states, but the degree of passivation is ligand dependent. For example, long-chain alkyls result in an incomplete bonding of surface atoms, because of steric hindrance, leaving some trap states remaining. In comparison, chloride ions as a compact ligand has shown almost complete passivation to the QDs surface [104]. Adsorbed surface molecules are also known to affect intraband cooling of hot carriers and recombination rates in QDs through energy transfer to their vibrational states [26]. Hence, we study the effect of different ligands on ultrafast dynamics in HgTe QDs in Chapter 3.

Energy levels in the CB of QDs move further apart than the energy of a single phonon close to the CBM [55]. Consequently, the phonon cooling rate decreases, leaving other mechanisms, such as Auger cooling and energy transfer to the vibrational modes of surface ligands, as the main cooling processes. A study in 2008 [105] showed that the cooling rate from $1P_e$ to $1S_e$ (i.e. CBM-1 to the conduction band minimum (CBM)) can be decreased by three orders of magnitude, with cooling times exceeding 1 ns for thick-shelled type-II QDs. In type-II QDs, the electron and holes are located in different parts of the hetero-QD, i.e. one in the core and the other in the shell; while, in type-I QDs the electron and hole are localised in the same part, either in the core or in the shell [106]. This heterostructure reduces the wavefunction overlap of the photo-generated ehp, which decreases Auger cooling, and the thickness of the shell isolates the ehp from the surface ligands, reducing vibrational energy transfer. The dramatic drop reported in cooling rate could allow MEG processes to dominate, and therefore, a change in solar cell efficiency could be realised. However, slower cooling will not benefit MEG, unless the electron still has sufficient energy to produce an additional ehp by impact ionisation [34]. In other words, the energy above the CBM should be greater than the ehp formation energy. Unfortunately, the energy difference for most QDs between an electron in the $1P_e$ level and one in the $1S_e$ level is less than the required energy level for exciton creation, and is therefore insufficient to enable MEG [34]. However, in semimetal

QDs, the energy difference between $1P_e$ and $1S_e$ levels is sufficient to allow MEG from the $1P_e$ state. Let us consider a simple model of the energy level structure in QDs, where, for a spherically symmetric QD, the energy of an ehp, E_{ehp}, is approximately given by [107]:

$$E_{ehp}(n_h L_h n_e L_e) = E_{\mathrm{g}} + \frac{\hbar^2}{2a^2}\left\{\frac{\varphi^2(n_h, L_h)}{m_{eff}^{v}} + \frac{\varphi^2(n_e, L_e)}{m_{eff}^{c}}\right\} - E_{\mathrm{c}}$$

Equation 1.10

where E_{g} is the bandgap of the bulk semiconductor; m_{eff}^{v} and m_{eff}^{c} are the effective masses of the hole and electron, respectively; a is the radius of a spherical potential well, $\phi\,(n_i, L_i)$ i=e,h is the n^{th} zero of a spherical Bessel function of order L (the states of the electron and hole being determined by ordinal and angular momentum quantum numbers n_e and L_e, and n_h and L_h, respectively); and E_c is a result of the Coulomb attraction, and is equal to ($1.8e^2/\,\mathcal{E}a$) where $\mathcal{E}$ is the dielectric constant of the material, but because $\mathcal{E}a \gg 1.8e^2$, E_c can be neglected. The term $\frac{\hbar^2}{2a^2}\frac{\varphi^2(n_h,L_h)}{m_{eff}^{v}}$ implies the confinement energy for the hole, and describes the existence of different energy values for discrete energy levels. Similarly, $\frac{\hbar^2}{2a^2}\frac{\varphi^2(n_e,L_e)}{m_{eff}^{c}}$ defines changes in the confinement energy for the electron according to its level. However, because E_{g} ~ -0.15 eV, m_{eff}^{c}=0.017m_0 , and m_{eff}^{v}=0.5m_0, where m_0 is the electron mass [108], in HgTe QDs, the confinement energy is mostly governed by the electron. The values of $\phi\,(1,0)$ and $\phi\,(1,1)$, corresponding to the $1S_i$ and $1P_i$ states, are 3.15 and 4.5 and their squared values are ~ 9.9 and ~ 20.3, respectively, and therefore for HgTe, QDs $E_{ehp}(1P_h1P_e)$ ~ $2E_{ehp}(1S_h1S_e)$ [34]. This means it is possible for an electron to cool from level $1P_e$ in the conduction band, to $1S_e$ of a semimetal QD, to discharge adequate energy to allow MEG.

1.4.1.2 Why $Cd_xHg_{(1-x)}Te$ alloy QDs?

The reasons detailed above in reference to HgTe for expecting good MEG quantum yield are also applicable here; however, there are also some additional benefits that might be obtained from cadmium mercury telluride ($Cd_xHg_{(1-x)}Te$) QDs. The band gap in bulk $Cd_xHg_{(1-x)}Te$ is dependent on alloy composition [109], which allows it to be tuned between the band gap of the bulk semimetal HgTe and the band gap of CdTe (1.44 eV at room temperature [110]). Both the band gap, and the split-off energy difference in valence levels change linearly according to the alloy composition in bulk $Cd_xHg_{(1-x)}Te$, but in different ways [79] (see Figure 1.12). This dependency enables the band gap and split-off energies to resonate with a certain composition value [79], which can lower the energy required for charge multiplication [111]. For example, this condition was found to favour charge multiplication when the band gap was 0.9 eV [109]. Hence, the band gap of $Cd_xHg_{(1-x)}Te$ alloy QDs can be tuned using two means: controlling the size of the QD and/or the composition degree. This could allow control of the point at which the band gap and the split-off energies match each other, and therefore move it towards the optimum value for exploitation of the solar spectrum. Another advantage of these materials is the anticipated low MEG threshold, as the electron's effective mass is significantly lower than that of the hole.

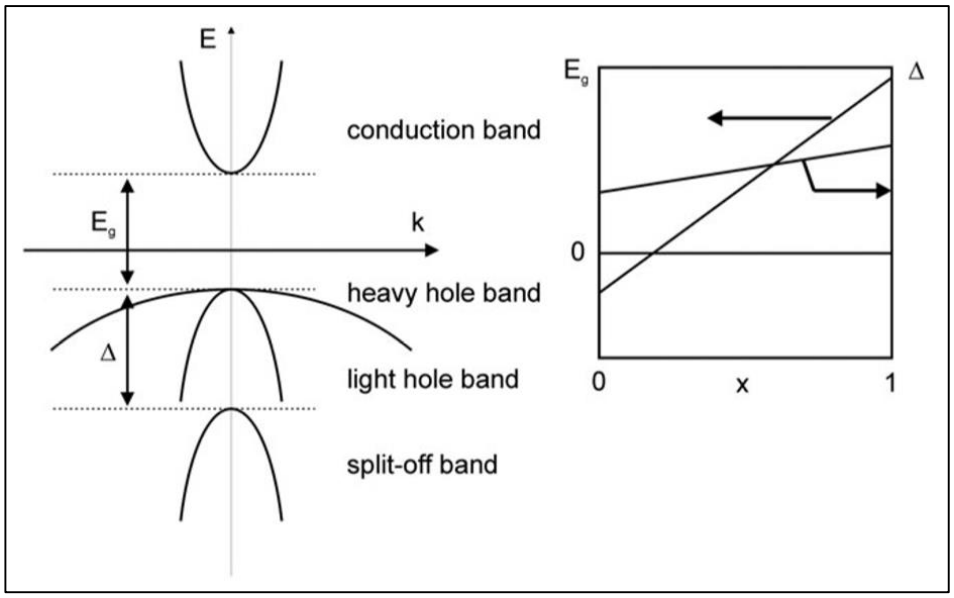

Figure 1.12 Conduction and valence levels near the band edge (left) and the variation of both the band gap, E_g, and the split-off energy level difference, Δ, versus composition, x, for bulk $Cd_xHg_{(1-x)}Te$. Both have a linear relationship with composition but this is much weaker for Δ. "Reproduced from [79] with permission of the PCCP Owner Societies"

1.4.1.3 Why a new study on theTiO_2-Au system?

Chapter 5 of the thesis centres on the study of TiO_2-Au NPs. The reason for studying a different, although also relevant to solar energy, system, was to maximise the use of time during the PhD study, since it took longer than anticipated for some of the HgTe and CdHgTe QD samples to become available. The optical characteristics of TiO_2 when combined with Au NPs have been widely reported [62, 96, 112, 113]; however, most of the ultrafast studies published on TiO_2-Au NPs have investigated the electron injection process from gold to the conduction band of TiO_2 when probing NIR or IR wavelengths [114-116]. The reverse process, i.e. capturing electrons from the TiO_2 conduction band to the Au NP resulting in charge separation [113], is key to improving the photo-catalytic efficiency of TiO_2; however, it has not yet been studied on the sub-nanosecond time-scale. Plasmon decay in Au NPs is a well-known process involving three stages [117]: electron-electron scattering, electron-phonon scattering and heat dissipation to the surrounding environment. The cooling rates associated with each of these stages relative to the rate of re-injection of hot electrons back into the TiO_2 determine the charge separation yield, and are system dependent. Surface

chemistry is a key factor in the cooling process [117], as some molecules can exchange electrons with the Au surface, opening a new route for electron cooling. Further, discrepancy exists in the literature concerning whether the diameter of the Au NPs affects cooling or not [117], with some studies reporting dependence on the size of the Au NPs of electron-phonon scattering, while others observing no such dependence. Known surface chemistry dependence in addition to discrepancy in size-dependence suggest that the cooling rates for any materials synthesised using new methods need to be assessed. Damato *et al*. [112] recently developed a new facile and environmentally-friendly method for the synthesis of mono-dispersed Au NPs that are distributed uniformly over the surface of TiO_2. Such well-controlled properties allow dependence on NP diameter to be studied, and ultimately, optimisation of its photocatalytic and photovoltaic applications.

1.5 Aim and objectives

The primary aim of this research is to further understanding of ultrafast charge dynamics in a number of nanostructured materials of relevance to the production of renewable energy, using ultrafast transient absorption spectroscopy. In order to achieve this aim, the objectives are specified as follows:

- To study the MEG process in HgTe QDs and CdHgTe alloy QDs and reliably determine its efficiency.
- To examine the effect on sub-nanosecond charge dynamics in HgTs QDs of three different passivating ligands: 1-thioglycerol, mercaptopropionic acid (MPA) and dodecanethiol (DDT).
- To investigate whether the sub-nanosecond charge dynamics of TiO_2 colloidal spheres decorated with Au nanoparticles is affected by the size of the nanoparticles.

1.6 Thesis outline

The experimental techniques used throughout the study are described in Chapter 2. Instruments used for steady state absorption and photoluminescence spectroscopy, as basic techniques for initial characterisation of the samples, are stated and the sample optical density measurement is explained. After that, ultrafast transient absorption spectroscopy, the main technique used throughout the thesis, is covered in detail. That includes the laser systems involved in the generation of the probe and pump beams and the way in which they were used on the experimental table. The chapter describes the way in which both the UTA signal and pump-induced transmittance change spectra were obtained followed by an interpretation of the signal. It explains the measurement of MEG and finally shows the response of the UTA experiment to the solvents and ligands used in the samples.

Chapter 3 details the study of ultrafast charge dynamics of HgTe QDs passivated with different ligands including: 1-thioglycerol, MPA and DDT. It highlights the chemical structure of the ligands used and the results obtained. The results begin with an initial characterisation of the PL and absorption spectra compared with calculated ones. It then presents the pump-induced transmittance change spectra and excitonic dynamics using ultrafast transient absorption spectroscopy. The chapter discusses the possible underlying mechanisms: MEG and all sub-nanosecond trap-related processes. It discusses the chemical structures of the ligands and the influence of the carboxylic acid group, in MPA-capped samples, on the passivation processes. The chapter also identifies MEG for the first time in semimetal QDs and shows how MEG can be mistaken if other recombination processes are not considered.

Chapter 4 outlines the ultrafast exciton dynamics in $Cd_xHg_{(1-x)}Te$ alloy QDs. The investigation starts with the basic electronic properties including steady state absorption,

photoluminescence and pump-induced transmittance change spectra. Next, the decay of the transmittance transients is obtained at different wavelengths above and below the MEG threshold in order to investigate the excitonic dynamics of the sample. The chapter investigates the shape of the transients obtained for stirred and static samples and discusses all the possible mechanisms that can be involved in sub-nanosecond transients. It finally reports MEG QY measurement and compares it to a recent published value.

The study of picosecond-scale electron dynamics in different sizes of Au NPs loaded on colloidal TiO_2 spheres is reported in Chapter 5. It begins with a brief description of the synthesis method used and the sizes of the materials. The chapter presents the electronic characterisation of the samples including the steady state absorption, PL and pump-induced transmittance change spectra. After that, charge dynamics of the samples are investigated at the plasmon band using ultrafast transient absorption spectroscopy to study the effect of the NP size on the overall dynamics. Chapter 8 finally concludes all the main results in the thesis and then provides suggestions for future work.

1.7 References

1. Nozik, A.J. and J. Miller, *Introduction to Solar Photon Conversion.* Chemical Reviews, 2010. **110**(11): p. 6443-6445.
2. Sawin, J., *Renewables 2013 Global Status Report*, in *REN21*, L. Mastny, Editor. 2013: Paris, France. p. 178.
3. Weisz, P.B., *Basic choices and constraints on long-term energy supplies.* Physics Today, 2004. **57**(7): p. 47-52.
4. Bera, D., et al., *Quantum Dots and Their Multimodal Applications: A Review.* Materials, 2010. **3**(4): p. 2260-2345.
5. Stephens, B. *How much "useful" radiation does the sun deliver?* . [cited 2014 25/05/2014]; Available from: http://www.k-laserusa.com/how-much-useful-radiation-does-the-sun-deliver/.
6. Hillhouse, H.W. and M.C. Beard, *Solar cells from colloidal nanocrystals: Fundamentals, materials, devices, and economics.* Current Opinion in Colloid & Interface Science, 2009. **14**(4): p. 245-259.
7. Green, M.A., *Third generation photovoltaics: solar cells for 2020 and beyond.* Physica E-Low-Dimensional Systems & Nanostructures, 2002. **14**(1-2): p. 65-70.
8. Shockley, W. and H.J. Queisser, *Detailed balance limit of effeciency of p-n junction solar cells.* Journal of Applied Physics, 1961. **32**(3): p. 510-&.
9. Nozik, A.J., *Quantum dot solar cells.* Physica E-Low-Dimensional Systems & Nanostructures, 2002. **14**(1-2): p. 115-120.
10. Hanna, M.C. and A.J. Nozik, *Solar conversion efficiency of photovoltaic and photoelectrolysis cells with carrier multiplication absorbers.* Journal of Applied Physics, 2006. **100**(7): p. 074510.
11. Klimov, V.I., *Spectral and Dynamical Properties of Multiexcitons in Semiconductor Nanocrystals.* Annual Review of Physical Chemistry, 2007. **58**(1): p. 635-673.
12. Szczech, J.R., J.M. Higgins, and S. Jin, *Enhancement of the thermoelectric properties in nanoscale and nanostructured materials.* Journal of Materials Chemistry, 2011. **21**(12): p. 4037-4055.
13. Trinh, M.T., et al., *A Hot Electron-Hole Pair Breaks the Symmetry of a Semiconductor Quantum Dot.* Nano Letters, 2013. **13**(12): p. 6091-6097.
14. Murphy, C.J. and J.L. Coffer, *Quantum dots: A primer.* Applied Spectroscopy, 2002. **56**(1): p. 16A-27A.
15. Coe-Sullivan, S., *Quantum dot developments.* Nature Photonics, 2009. **3**(6): p. 315-316.
16. Cao, Y.-L., et al., *Three-region characteristic temperature in p-doped quantum dot lasers.* Applied Physics Letters, 2014. **104**(4).
17. Smith, C. and D. Binks, *Multiple Exciton Generation in Colloidal Nanocrystals* Nanomaterials, 2013. **4**(1): p. 19-45.
18. Nozik, A.J., *Multiple exciton generation in semiconductor quantum dots.* Chemical Physics Letters, 2008. **457**(1-3): p. 3-11.
19. Nozik, A.J., et al., *Semiconductor Quantum Dots and Quantum Dot Arrays and Applications of Multiple Exciton Generation to Third-Generation Photovoltaic Solar Cells.* Chemical Reviews, 2010. **110**(11): p. 6873-6890.
20. Nozik, A.J., *Spectroscopy and hot electron relaxation dynamics in semiconductor quantum wells and quantum dots.* Annual Review of Physical Chemistry, 2001. **52**(1): p. 193-231.

21. Binks, D.J., *Multiple exciton generation in nanocrystal quantum dots - controversy, current status and future prospects.* Physical Chemistry Chemical Physics, 2011. **13**(28): p. 12693-12704.
22. Tang, J., et al., *Colloidal-quantum-dot photovoltaics using atomic-ligand passivation.* Nat Mater, 2011. **10**(10): p. 765-771.
23. Chuang, C.-H.M., et al., *Improved performance and stability in quantum dot solar cells through band alignment engineering.* Nature Materials, 2014. **13**(8): p. 796-801.
24. Pattantyus-Abraham, A.G., et al., *Depleted-Heterojunction Colloidal Quantum Dot Solar Cells.* ACS Nano, 2010. **4**(6): p. 3374-3380.
25. Meillaud, F., et al., *Efficiency limits for single junction and tandem solar cells.* Solar Energy Materials and Solar Cells, 2006. **90**(18-19): p. 2952-2959.
26. Peterson, M.D., et al., *The Role of Ligands in Determining the Exciton Relaxation Dynamics in Semiconductor Quantum Dots.* Annual Review of Physical Chemistry, Vol 65, 2014. **65**: p. 317-339.
27. Blackburn, J.L., et al., *Electron Relaxation in Colloidal InP Quantum Dots with Photogenerated Excitons or Chemically Injected Electrons.* The Journal of Physical Chemistry B, 2002. **107**(1): p. 102-109.
28. Guyot-Sionnest, P., et al., *Intraband relaxation in CdSe quantum dots.* Physical Review B, 1999. **60**(4): p. R2181-R2184.
29. Gontijo, I., et al., *Time-resolved photoluminescence and carrier dynamics in vertically-coupled self-assembled quantum dots.* Japanese Journal of Applied Physics Part 1-Regular Papers Short Notes & Review Papers, 1999. **38**(2A): p. 674-680.
30. Meier, A., et al., *Fast electron transfer across semiconductor-molecule interfaces: GaAs/Co(Cp)(2)(+/0).* Journal of Physical Chemistry B, 1999. **103**(12): p. 2122-2141.
31. Vavilov, V.S., *On photo-ionization by fast electrons in germanium and silicon.* Journal of Physics and Chemistry of Solids, 1959. **8**: p. 223-226.
32. Beattie, A.R., *Quantum efficiency in InSb.* Journal of Physics and Chemistry of Solids, 1962. **23**(AUG): p. 1049-&.
33. Jung, H.K., K. Taniguchi, and C. Hamaguchi, *Impact ionization model for full band Monte Carlo simulation in GaAs.* Journal of Applied Physics, 1996. **79**(5): p. 2473-2480.
34. McElroy, N., et al., *Increasing Efficiency with Multiple Exciton Generation.* Quantum Dot Solar Cells, 2014. **15**: p. 233-253.
35. Smith, A. and D. Dutton, *Behavior of lead sulfide photocells in the ultraviolet.* Journal of the Optical Society of America, 1958. **48**(12): p. 1007-1009.
36. Geist, J., J.L. Gardner, and F.J. Wilkinson, *Surface-field-induced feature in the quantum yield of silicon near 3.5 eV.* Physical Review B, 1990. **42**(2): p. 1262-1267.
37. Beard, M.C. and R.J. Ellingson, *Multiple exciton generation in semiconductor nanocrystals: Toward efficient solar energy conversion.* Laser & Photonics Reviews, 2008. **2**(5): p. 377-399.
38. Beard, M.C., et al., *Comparing Multiple Exciton Generation in Quantum Dots To Impact Ionization in Bulk Semiconductors: Implications for Enhancement of Solar Energy Conversion.* Nano Letters, 2010. **10**(8): p. 3019-3027.
39. Pijpers, J.J.H., et al., *Assessment of carrier-multiplication efficiency in bulk PbSe and PbS.* Nature Physics, 2009. **5**(11): p. 811-814.

40. Delerue, C., et al., *Carrier multiplication in bulk and nanocrystalline semiconductors: Mechanism, efficiency, and interest for solar cells.* Physical Review B, 2010. **81**(12): p. 125306.
41. Schaller, R.D., V.M. Agranovich, and V.I. Klimov, *High-efficiency carrier multiplication through direct photogeneration of multi-excitons via virtual single-exciton states.* Nature Physics, 2005. **1**(3): p. 189-194.
42. Rupasov, V.I. and V.I. Klimov, *Carrier multiplication in semiconductor nanocrystals via intraband optical transitions involving virtual biexciton states.* Physical Review B, 2007. **76**(12).
43. Velizhanin, K.A. and A. Piryatinski, *Numerical analysis of carrier multiplication mechanisms in nanocrystalline and bulk forms of PbSe and PbS.* Physical Review B, 2012. **86**(16).
44. Shabaev, A., A.L. Efros, and A.J. Nozik, *Multiexciton Generation by a Single Photon in Nanocrystals.* Nano Letters, 2006. **6**(12): p. 2856-2863.
45. Velizhanin, K.A. and A. Piryatinski, *Numerical Study of Carrier Multiplication Pathways in Photoexcited Nanocrystal and Bulk Forms of PbSe.* Physical Review Letters, 2011. **106**(20).
46. Allan, G. and C. Delerue, *Role of impact ionization in multiple exciton generation in PbSe nanocrystals.* Physical Review B, 2006. **73**(20): p. 205423.
47. Cadirci, M., et al., *Ultrafast exciton dynamics in InAs/ZnSe nanocrystal quantum dots.* Physical Chemistry Chemical Physics, 2012. **14**(43): p. 15166-15172.
48. Allan, G. and C. Delerue, *Influence of electronic structure and multiexciton spectral density on multiple-exciton generation in semiconductor nanocrystals: Tight-binding calculations.* Physical Review B, 2008. **77**(12).
49. Allan, G. and C. Delerue, *Optimization of Carrier Multiplication for More Effcient Solar Cells: The Case of Sn Quantum Dots.* Acs Nano, 2011. **5**(9): p. 7318-7323.
50. Al-Otaify, A., et al., *Multiple exciton generation and ultrafast exciton dynamics in HgTe colloidal quantum dots.* Physical Chemistry Chemical Physics, 2013. **15**(39): p. 16864-16873.
51. McGuire, J.A., et al., *New Aspects of Carrier Multiplication in Semiconductor Nanocrystals.* Accounts of Chemical Research, 2008. **41**(12): p. 1810-1819.
52. Hardman, S.J.O., et al., *Electronic and surface properties of PbS nanoparticles exhibiting efficient multiple exciton generation.* Physical Chemistry Chemical Physics, 2011. **13**(45): p. 20275-20283.
53. Midgett, A.G., et al., *Flowing versus Static Conditions for Measuring Multiple Exciton Generation in PbSe Quantum Dots.* The Journal of Physical Chemistry C, 2010. **114**(41): p. 17486-17500.
54. Kim, J.Y., et al., *25th Anniversary Article: Colloidal Quantum Dot Materials and Devices: A Quarter-Century of Advances.* Advanced Materials, 2013. **25**(36): p. 4986-5010.
55. Tyagi, P. and P. Kambhampati, *False multiple exciton recombination and multiple exciton generation signals in semiconductor quantum dots arise from surface charge trapping.* The Journal of Chemical Physics, 2011. **134**(9): p. 094706-10.
56. Ni, M., et al., *A review and recent developments in photocatalytic water-splitting using for hydrogen production.* Renewable and Sustainable Energy Reviews, 2007. **11**(3): p. 401-425.
57. Jose, D., et al., *Au-TiO2 Nanocomposites and Efficient Photocatalytic Hydrogen Production under UV-Visible and Visible Light Illuminations: A Comparison of Different Crystalline Forms of TiO2.* International Journal of Photoenergy, 2013.

58. Chen, X. and S.S. Mao, *Titanium Dioxide Nanomaterials: Synthesis, Properties, Modifications, and Applications.* Chemical Reviews, 2007. **107**(7): p. 2891-2959.
59. Kamat, P.V., *Meeting the Clean Energy Demand: Nanostructure Architectures for Solar Energy Conversion.* The Journal of Physical Chemistry C, 2007. **111**(7): p. 2834-2860.
60. Peter, L.M., *The Grätzel Cell: Where Next?* The Journal of Physical Chemistry Letters, 2011. **2**(15): p. 1861-1867.
61. Kamat, P.V., *TiO2 Nanostructures: Recent Physical Chemistry Advances.* The Journal of Physical Chemistry C, 2012. **116**(22): p. 11849-11851.
62. Chandrasekharan, N. and P.V. Kamat, *Improving the Photoelectrochemical Performance of Nanostructured TiO2 Films by Adsorption of Gold Nanoparticles†.* The Journal of Physical Chemistry B, 2000. **104**(46): p. 10851-10857.
63. Stiles, P.L., et al., *Surface-Enhanced Raman Spectroscopy*, in *Annual Review of Analytical Chemistry*. 2008. p. 601-626.
64. Schasfoort, R.B.M. and A.J. Tudos, *Handbook of surface plasmon resonance*. 2008, Cambridge: Royal Society of Chemistry.
65. Petryayeva, E. and U.J. Krull, *Localized surface plasmon resonance: Nanostructures, bioassays and biosensing—A review.* Analytica Chimica Acta, 2011. **706**(1): p. 8-24.
66. Weller, H., et al., *Photochemistry of semiconductor colloids .14. photochemistry of colloidal semiconductors - onset of light-absorption as a function of size of extremely small CdS particles.* Chemical Physics Letters, 1986. **124**(6): p. 557-560.
67. Murray, C.B., D.J. Norris, and M.G. Bawendi, *Synthesis and characterization of nearly monodisperse CdE (E = sulfur, selenium, tellurium) semiconductor nanocrystallites.* Journal of the American Chemical Society, 1993. **115**(19): p. 8706-8715.
68. LaMer, V.K. and R.H. Dinegar, *Theory, Production and Mechanism of Formation of Monodispersed Hydrosols.* Journal of the American Chemical Society, 1950. **72**(11): p. 4847-4854.
69. Hines, M.A. and P. Guyot-Sionnest, *Synthesis and Characterization of Strongly Luminescing ZnS-Capped CdSe Nanocrystals.* The Journal of Physical Chemistry, 1996. **100**(2): p. 468-471.
70. Li, J.J., et al., *Large-Scale Synthesis of Nearly Monodisperse CdSe/CdS Core/Shell Nanocrystals Using Air-Stable Reagents via Successive Ion Layer Adsorption and Reaction.* Journal of the American Chemical Society, 2003. **125**(41): p. 12567-12575.
71. Ellingson, R.J., et al., *Highly Efficient Multiple Exciton Generation in Colloidal PbSe and PbS Quantum Dots.* Nano Letters, 2005. **5**(5): p. 865-871.
72. Murphy, J.E., et al., *PbTe Colloidal Nanocrystals: Synthesis, Characterization, and Multiple Exciton Generation.* Journal of the American Chemical Society, 2006. **128**(10): p. 3241-3247.
73. Schaller, R.D., J.M. Pietryga, and V.I. Klimov, *Carrier Multiplication in InAs Nanocrystal Quantum Dots with an Onset Defined by the Energy Conservation Limit.* Nano Letters, 2007. **7**(11): p. 3469-3476.
74. Im, S.H., et al., *Efficient HgTe colloidal quantum dot-sensitized near-infrared photovoltaic cells.* Nanoscale, 2012. **4**(5): p. 1581-1584.
75. Olk, P., et al., *Subwavelength emitters in the near-infrared based on mercury telluride nanocrystals.* Applied Physics Letters, 2004. **84**(23): p. 4732-4734.

76. Priyam, A., D.E. Blumling, and K.L. Knappenberger, *Synthesis, Characterization, and Self-Organization of Dendrimer-Encapsulated HgTe Quantum Dots.* Langmuir, 2010. **26**(13): p. 10636-10644.
77. McGuire, J.A., et al., *Apparent Versus True Carrier Multiplication Yields in Semiconductor Nanocrystals.* Nano Letters, 2010. **10**(6): p. 2049-2057.
78. Yang, Z. and H.-T. Chang, *CdHgTe and CdTe quantum dot solar cells displaying an energy conversion efficiency exceeding 2%.* Solar Energy Materials and Solar Cells, 2010. **94**(12): p. 2046-2051.
79. Kershaw, S.V., et al., *Multiple exciton generation in cluster-free alloy CdxHg1-xTe colloidal quantum dots synthesized in water.* Physical Chemistry Chemical Physics, 2014.
80. Schaller, R.D. and V.I. Klimov, *High efficiency carrier multiplication in PbSe nanocrystals: Implications for solar energy conversion.* Physical Review Letters, 2004. **92**(18): p. 186601.
81. Schaller, R.D., M.A. Petruska, and V.I. Klimov, *Effect of electronic structure on carrier multiplication efficiency: Comparative study of PbSe and CdSe nanocrystals.* Applied Physics Letters, 2005. **87**(25).
82. Kobayashi, Y., T. Udagawa, and N. Tamai, *Carrier Multiplication in CdTe Quantum Dots by Single-photon Timing Spectroscopy.* Chemistry Letters, 2009. **38**(8): p. 830-831.
83. Gachet, D., et al., *An Upper Bound to Carrier Multiplication Efficiency in Type II Colloidal Quantum Dots.* Nano Letters, 2010. **10**(1): p. 164-170.
84. Pijpers, J.J.H., et al., *Carrier multiplication and its reduction by photodoping in colloidal InAs quantum dots.* Journal of Physical Chemistry C, 2007. **111**(11): p. 4146-4152.
85. Beard, M.C., et al., *Multiple Exciton Generation in Colloidal Silicon Nanocrystals.* Nano Letters, 2007. **7**(8): p. 2506-2512.
86. Nair, G. and M.G. Bawendi, *Carrier multiplication yields of CdSe and CdTe nanocrystals by transient photoluminescence spectroscopy.* Physical Review B, 2007. **76**(8): p. 081304.
87. Califano, M., *Photoinduced Surface Trapping and the Observed Carrier Multiplication Yields in Static CdSe Nanocrystal Samples.* Acs Nano, 2011. **5**(5): p. 3614-3621.
88. Pijpers, J.J.H., et al., *Carrier multiplication and its reduction by photodoping in colloidal InAs quantum dots (vol 111, pg 4146, 2007).* Journal of Physical Chemistry C, 2008. **112**(12): p. 4783-4784.
89. Ben-Lulu, M., et al., *On the Absence of Detectable Carrier Multiplication in a Transient Absorption Study of InAs/CdSe/ZnSe Core/Shell1/Shell2 Quantum Dots.* Nano Letters, 2008. **8**(4): p. 1207-1211.
90. Califano, M., *Direct and Inverse Auger Processes in InAs Nanocrystals: Can the Decay Signature of a Trion Be Mistaken for Carrier Multiplication?* Acs Nano, 2009. **3**(9): p. 2706-2714.
91. Stubbs, S.K., et al., *Efficient carrier multiplication in InP nanoparticles.* Physical Review B, 2010. **81**(8): p. 081303.
92. Schneider, J., et al., *Understanding TiO2 Photocatalysis: Mechanisms and Materials.* Chemical Reviews, 2014. **114**(19): p. 9919-9986.
93. Tada, H., T. Kiyonaga, and S.-i. Naya, *Rational design and applications of highly efficient reaction systems photocatalyzed by noble metal nanoparticle-loaded titanium(iv) dioxide.* Chemical Society Reviews, 2009. **38**(7): p. 1849-1858.

94. Gupta, S. and M. Tripathi, *A review of TiO_2 nanoparticles.* Chinese Science Bulletin, 2011. **56**(16): p. 19.
95. Bamwenda, G.R., et al., *Photoassisted hydrogen production from a water-ethanol solution: a comparison of activities of Au・TiO2 and Pt・TiO2.* Journal of Photochemistry and Photobiology A: Chemistry, 1995. **89**(2): p. 177-189.
96. Du, L., et al., *Ultrafast plasmon induced electron injection mechanism in gold–TiO2 nanoparticle system.* Journal of Photochemistry and Photobiology C: Photochemistry Reviews, 2013. **15**(0): p. 21-30.
97. Link, S. and M.A. El-Sayed, *Shape and size dependence of radiative, non-radiative and photothermal properties of gold nanocrystals.* International Reviews in Physical Chemistry, 2000. **19**(3): p. 409-453.
98. Khon, E., et al., *Suppression of the Plasmon Resonance in Au/CdS Colloidal Nanocomposites.* Nano Letters, 2011. **11**(4): p. 1792-1799.
99. Farhangfar, S., *Quantum size effects in a one-dimensional semimetal.* Physical Review B, 2006. **74**(20): p. 205318.
100. Rinnerbauer, V., et al., *Effect of quantum confinement on higher transitions in HgTe nanocrystals.* Applied Physics Letters, 2006. **89**(19).
101. Pavesi, L., et al. *Towards the first silicon laser*. Dordrecht: Kluwer Academic Publishers.
102. Harrison, M.T., et al., *Colloidal nanocrystals for telecommunications. Complete coverage of the low-loss fiber windows by mercury telluride quantum dots.* Pure and Applied Chemistry, 2000. **72**(1-2): p. 295-307.
103. Espinobarro-Velazquez, D., et al., *Effect of Chloride Passivation on Recombination Dynamics in CdTe Colloidal Quantum Dots.* ChemPhysChem, 2015: p. 7.
104. Page, R., et al., *Near-Unity Quantum Yields from Chloride Treated CdTe Colloidal Quantum Dots.* Small, 2014: p. 7.
105. Pandey, A. and P. Guyot-Sionnest, *Slow Electron Cooling in Colloidal Quantum Dots.* Science, 2008. **322**(5903): p. 929-932.
106. Ivanov, S.A., et al., *Light amplification using inverted core/shell nanocrystals: Towards lasing in the single-exciton regime.* Journal of Physical Chemistry B, 2004. **108**(30): p. 10625-10630.
107. Klimov, V.I., ed. *Semiconductor and Metal Nanocrystals*. 2004, Marcel Dekker: New York. 484.
108. Berger, L.I., *Properties of semiconductors*, in *Handbook of Physics and Chemistery*, D.R. Lide, Editor. 2009, CRC: Boca Raton. p. 90.
109. Norton, P., *HgCdTe infrared detectors (Reprinted from Electrochem Soc. Proc., pg 48-70, 1999).* Opto-Electronics Review, 2002. **10**(3): p. 159-174.
110. Gupta, S., et al., *$Cd_xHg_{(1-x)}Te$ Alloy Colloidal Quantum Dots: Tuning Optical Properties From the Visible to Near-Infrared by Ion Exchange.* Particle & Particle Systems Characterization, 2013. **30**: p. 346-354.
111. Tsang, W., ed. *Lightwave Communications Technology*. Semiconductors and Semimetals. Vol. 22. 1985, Academic Press: London. 450.
112. Damato, T.C., et al., *A Facile Approach to TiO2 Colloidal Spheres Decorated with Au Nanoparticles Displaying Well-Defined Sizes and Uniform Dispersion.* Langmuir, 2013. **29**(5): p. 1642-1649.
113. Subramanian, V., E.E. Wolf, and P.V. Kamat, *Catalysis with TiO2/Gold Nanocomposites. Effect of Metal Particle Size on the Fermi Level Equilibration.* Journal of the American Chemical Society, 2004. **126**(15): p. 4943-4950.

114. Du, L., et al., *Plasmon induced electron transfer at gold–TiO2 interface under femtosecond near-IR two-photon excitation.* Thin Solid Films, 2009. **518**(2): p. 861-864.
115. Du, L., et al., *Plasmon-Induced Charge Separation and Recombination Dynamics in Gold−TiO2 Nanoparticle Systems: Dependence on TiO2 Particle Size.* The Journal of Physical Chemistry C, 2009. **113**(16): p. 6454-6462.
116. Furube, A., et al., *Ultrafast Plasmon-Induced Electron Transfer from Gold Nanodots into TiO2 Nanoparticles.* Journal of the American Chemical Society, 2007. **129**(48): p. 14852-14853.
117. Aruda, K.O., et al., *The role of interfacial charge transfer-type interactions in the decay of plasmon excitations in metal nanoparticles.* Physical Chemistry Chemical Physics, 2013. **15**(20): p. 7441-7449.

Chapter 2 Experimental Techniques

2.1 Introduction

This chapter describes the experimental techniques used throughout the study. The basic optical characterisation of the samples by steady state absorption and photoluminescence spectroscopy is described. The chapter also introduces UTA spectroscopy, the main technique used throughout the thesis, explaining briefly the laser systems involved in the generation of the probe and pump beams and the way in which they were used in the UTA experiment. The way in which both the UTA signal and pump-induced transmittance change spectra were obtained is also described. How the resulting data is processed and interpreted and how this relates to MEG measurements is detailed. Finally, the way in which the UTA experiment responds to the solvents and ligands used in the samples is described.

2.2 Optical characterisation.

Samples used in this study arrived in small bottles as solutions, which in some cases were very concentrated and needed dilution for the study. Some of the solution was transferred to 10 mm path length quartz cuvettes made by Starna, with a usable range from 170 to 2700 nm [1], and was diluted using deionised water, as necessary. The absorption and PL spectra of the samples were measured using an UV/Vis/NIR spectrometer (model: Lambda 1050) and a Horiba Jobin Yvon Fluorolog (model: iHR FL3-22) spectrofluorometer, respectively. The position of the absorption edge and the PL peak were used to determine the likely position of the bleach feature in the transient absorption spectrum and the band gap. Absorption measurements also enabled the sample to be diluted such that its absorbance, A, at the absorption edge was in the range 0.2–0.5, which from

experience gives the best UTA signal. The absorbance, sometimes known as the optical density, of the sample was calculated using the *natural logarithm* (as opposed to the logarithm to base 10, as in some works) as [2]

$$A = -\ln \frac{I_{out}}{I_0}$$

Equation 2.1

where I_0 is the initial intensity of light before a sample and I_{out} is the intensity of light when it exits the sample. The related quantity of transmittance, T , is also used in this thesis, where [2]

$$T = \frac{I_{out}}{I_0} = \exp(-A)$$

Equation 2.2

2.3 Ultrafast transient absorption (UTA) spectroscopy

UTA is a spectroscopic technique that has been used to investigate ultrafast charge dynamics in variety of NPs [3-6]. It is a time-resolved pump-probe experiment designed to measure the absorbance of a sample being pumped by high energy laser pulses in order to obtain information on electronic energies and charge cooling and recombination processes [4]. The pump excites the sample, creating eh pairs; low intensity probe pulses then measure the average number of excitons per NQD in a particular energy state. The measurement is taken as a function of the time delay between the arrival of the pump and probe beams, which can be controlled by varying the difference between their optical path lengths using a computer-controlled translation stage [3].

Two different types of transitions are mainly used in the probing process in QD research. The probe beam either monitors an intraband transition in the CB or the interband transitions of the sample from a level that is very close to but not at the valence band maximum (VBM) to the conduction band minimum (CBM); it is these interband transitions

that are probed in this study. It should be noted that due to the weakness of the transition from VBM to CBM, it cannot be easily used for UTA measurements. Each absorbed pump photon creates an ehp (or more than one when MEG occurs), after cooling the associated electrons fill CBM states and the holes relax to the VBM. As the probe absorption depends on the number of unoccupied states in the CBM, if the exciton population increases, absorption decreases, leading to an increase in the transmission of the probe through the QDs [7]; this is known as a 'bleach'. If only one exciton is created in a QD, the decay of the bleach will be in the form of mono-exponential decay with a lifetime in the ns scale. However, if excitation of two excitons per QD occurs, it results in a much faster decay component (10s of ps) as efficient Auger recombination is enabled. This fast time decay is therefore used as the signature of MEG [8]. If a lock-in amplifier synchronised to the repetition rate of the pump pulse is used, it allows only the CBM electrons that are created by pump pulses to be detected where the interest is in the magnitude of the lowest energy absorption maximum, namely the 1S peak. Details of the system are given in Sections 2.3.1 and 2.3.2.

2.3.1 Laser system

The laser system used is crucial to the UTA experiments. Basically, a mode-locked oscillator-amplifier laser system is used as the source of both the probe beam and, after nonlinear frequency conversion and mixing procedures, the pump beam. The time resolution of the system is primarily achieved by the pulse duration [3] with the laser system used here producing ultra-short pulses of ~100 fs or less. Furthermore, the system needs to be tunable over a wide range of wavelengths to expand its applications over a wide range of QDs. A schematic of the laser system used here is shown in Figure 2.1. Briefly, a Millennia laser is used to pump a Tsunami Ti:sapphire oscillator in order to produce mode-locked (~100 fs) pulses at 800 nm with a 81.2 MHz repetition rate. The pulses are used as the seed beam for a Spectra Physics SpitfirePro Ti:sapphire Regenerative Amplifier. The amplifier is pumped

by a Spectra Physics Empower Q-switched 532 nm laser with 12 W power to produce output pulses with 100 fs width and energy of 1 mJ at 1 kHz repetition rate [9-13]. The resultant beam is then split into two beams of 5% and 95% intensity respectively. The former is sent to the UTA experimental table (described in Section 2.3.2) to be used as the probe beam while the latter is passed through a tunable optical parametric amplifier known as TOPAS-C and frequency mixers to form the pump beam.

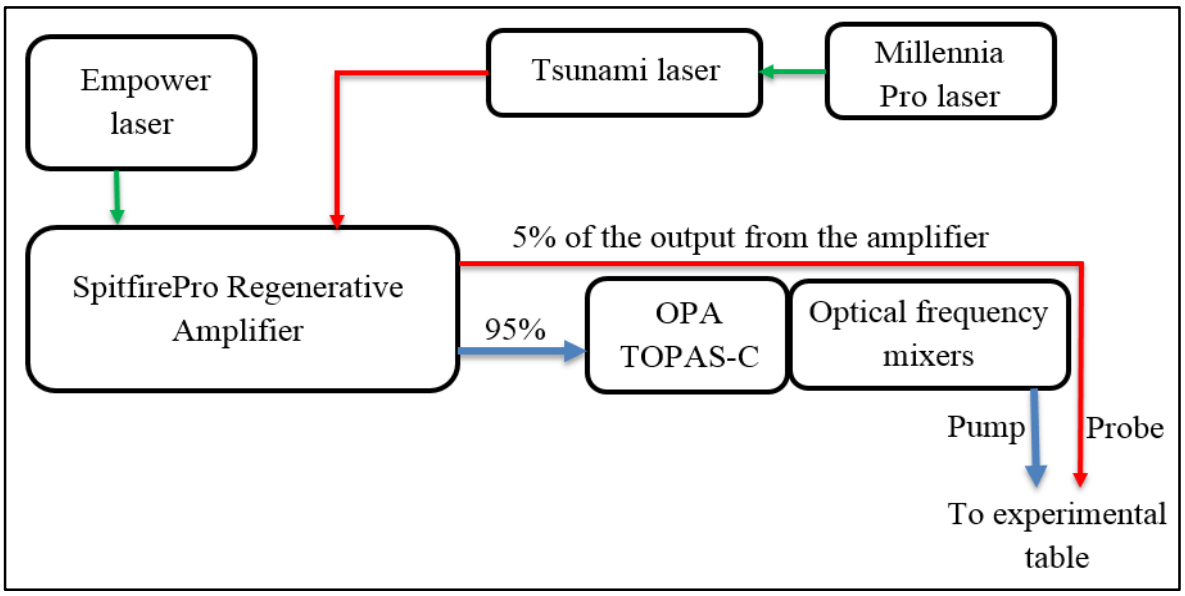

Figure 2.1. A schematic drawing of the UTA laser system.

2.3.1.1 Preparation before taking measurements

1- The cooling system (Millenia chiller) is first switched on for the main laser oscillator. All the electronics are on and the oscillator warms up, setting its pump laser to 12 W.

2- The cooling system for the laser used for pumping the amplifier also needs to be started and the pump system for the amplifier needs to be switched on.

3- Two hours are allowed for the oscillator to warm up and the output power (typically 500 mW) is then measured. At this stage, the laser spectrum is matched to the original one provided by the manufacturer with a 800 nm wavelength.

4- The laser is then fed to the amplifier and left for about half an hour to warm up.

5- The amplifier and optical parametric amplifier (OPA) outputs are then measured with a typical value of 93 mW at 800 nm and 250 mW at 1400 nm, respectively.

6- In terms of the pump wavelength, the configuration of both the optical frequency mixer and the wavelength selector should be set based on the wavelength required, as every set of wavelengths have their own configurations.

2.3.2 The UTA experimental table

The table was originally set by Dr Stuart K. Stubbs, a previous PhD student, but has since been modified by the researcher and his colleague Dr Musa Cadirci. Figure 2.2 shows the optical setup of the table exhibiting the two main beams; the paths of the probe and the pump are described below.

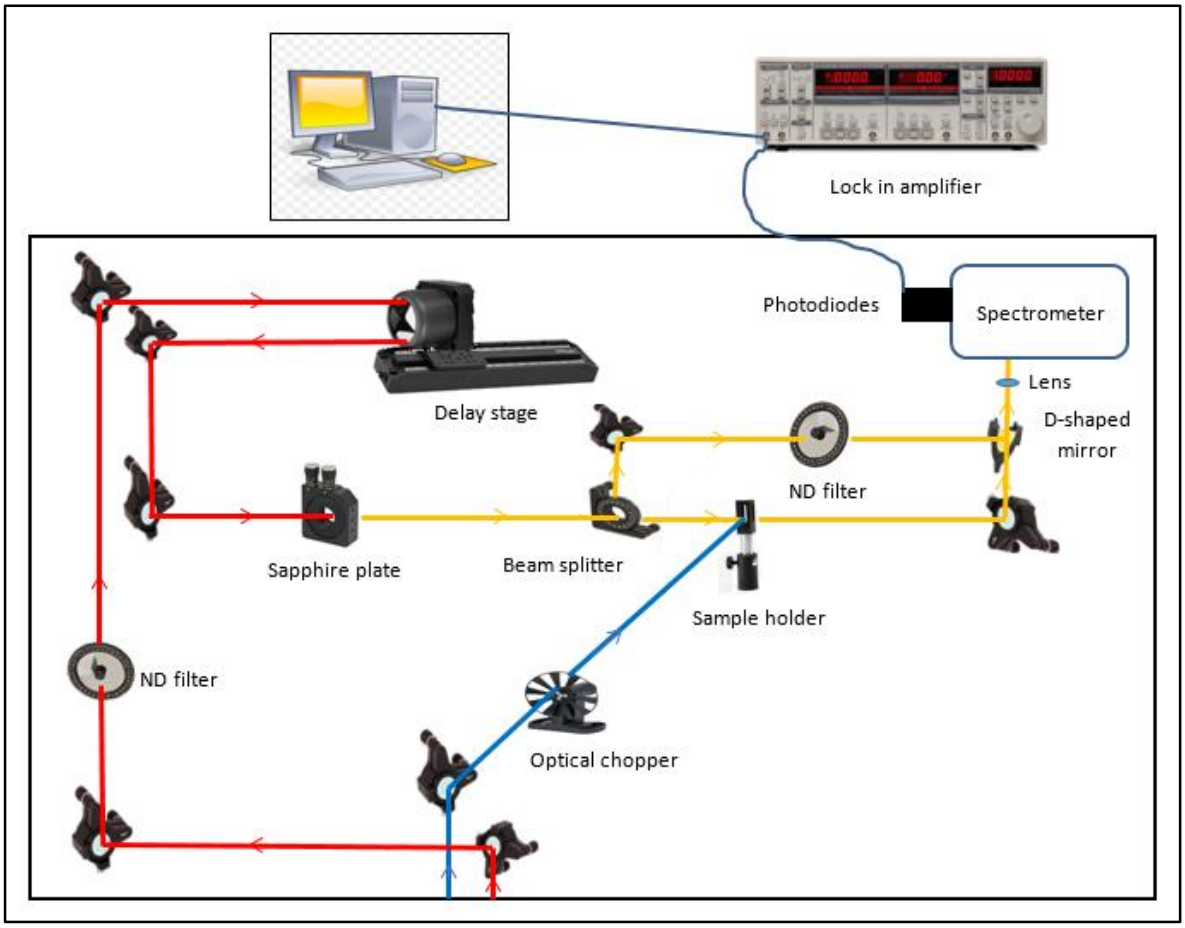

Figure 2.2. The optical setup of the UTA experimental table.

2.3.2.1 The probe beam path

Originally, the probe beam (shown in red in Figure 2.2) represents only 5% of the beam provided by the Spitfire Pro. It passes through a variable attenuation reflective neutral density (ND) filter to control the incident power for the sapphire crystal. It is then guided by mirrors to a Newport ILS series 200 mm delay stage with a retroreflector, which is used here to delay the probe beam with respect to the pump beam. A 1 mm step in the delay stage provides a 2 mm difference in the path length between the pump and probe beams. The formula $x = vt$ is applied where x here is the distance (2 mm) and v is the speed of light (3×10^8 m/s). This gives t a value of ~6.67 ps hence each 1 mm step in the delay stage corresponds to ~6.67 ps delay time. The probe beam then passes through a sapphire crystal to generate a white light continuum (WLC) which can be used as a probe beam for a variety of QDs with different bandgaps. The WLC probe beam (shown in yellow in Figure 2.2) travels through two lenses to be focused at the sample. However, before reaching the sample, the WLC is split into sample and reference beams by a beam splitter. The sample beam is directed by a mirror to the monochromator (SpectraPro 2500i 0.5 meter imaging spectrometer) and then onto high-speed silicon photodiodes passing through a focusing lens while the reference beam passes through a variable reflective ND filter to balance both the sample and reference beams. It is then directed by a D-shaped mirror to pass through the lens onto the monochromator. A D-shaped mirror rather than a normal one is used to allow the sample beam to pass over it to the monochromator. The monochromator is controlled by computer software (Lab-View) for the selection of the monitored wavelength.

2.3.2.2 The pump beam path

The blue line in Figure 2.2 represents the pump beam generated in the TOPAS-C, which is directed by UV-enhanced aluminium mirrors. An iris is placed in the pump path in front of the chopper for alignment in addition to blocking any unwanted beams generated by

the frequency mixing process. After passing through the iris, the pump beam is modulated with a mechanical chopper to provide a 500 Hz repetition rate. The pulses are then passed through the sample for pumping the QDs before being blocked just after the sample holder. In the UTA experimental table, a digital lock-in amplifier (Stanford Research Systems SR830) is phase-locked with the chopper to amplify any pump-induced difference between the sample and reference beams. The angle between the pump and probe beams at the sample position is adjusted to be around 25 degrees to enable these beams to interact as much as possible in order to gain more data. The measurements are taken by a data acquisition system based on a Lab-view program written specifically for detecting any change to the absorption in the presence and absence of the pump beam.

2.3.3 How is a transmittance change transient obtained?

Initially both the probe and pump beams are aligned along their respective paths, as shown in Figure 2.2, with good probe alignment corresponding to the lock-in amplifier producing about 1.1 V with the spectrometer set at zero order. The pump and probe spots were set and overlapped at the middle of the sample cuvette and the arrival of the pump and probe was set to occur in the mid-range of the delay-stage movement. The spectrometer was set at the 1S position of the QDs to monitor the carrier population at the sample band-edge. The intensities of the sample and reference beams were balanced via the tunable ND filter so that the difference in the corresponding photodiode signals produced a lock-in output of 10^{-6} or 10^{-7} V .The chopper channel was then turned on to synchronise the lock-in amplifier at 500 Hz, the pump repetition rate. Kinetic traces were then taken that are measured in volts but are proportional to the change in transmittance at the chopper frequency, ω_{ch}, i.e. $\Delta V(\omega_{ch}) = k\Delta T$, (where k is a constant of proportionality which depends on the probe beam power and the system response). These traces include a background, rise, peak and decay, as shown in Figure 2.3. Ten scans of the transients were typically obtained and

automatically averaged by the program used. The transmittance, T, of the sample is taken, by synchronising the lock-in to the pump repetition rate, rather than the chopper, and monitoring only the sample beam. This produces a signal (in volts) $V = kT$ proportional to the full power of the probe transmitted through the sample rather than just that portion that is being modulated at the chopper frequency. This signal is measured both before and after the transient measurement and then averaged. The decay signal was then processed as follows. The average of the background, which is due to photoluminescence, was subtracted from the whole decay to offset the signal. The decay was then calibrated by dividing through by the average of the transmittance signal i.e. $\Delta T/T = \Delta V(\omega_{ch})/V$. In terms of the horizontal axis, the original values represent the delay between the probe and pump beams in distance (mm); this was thus converted to time in ps. The time value corresponding to the peak of the transient signal was then set to zero. The signal is now ready for analysis.

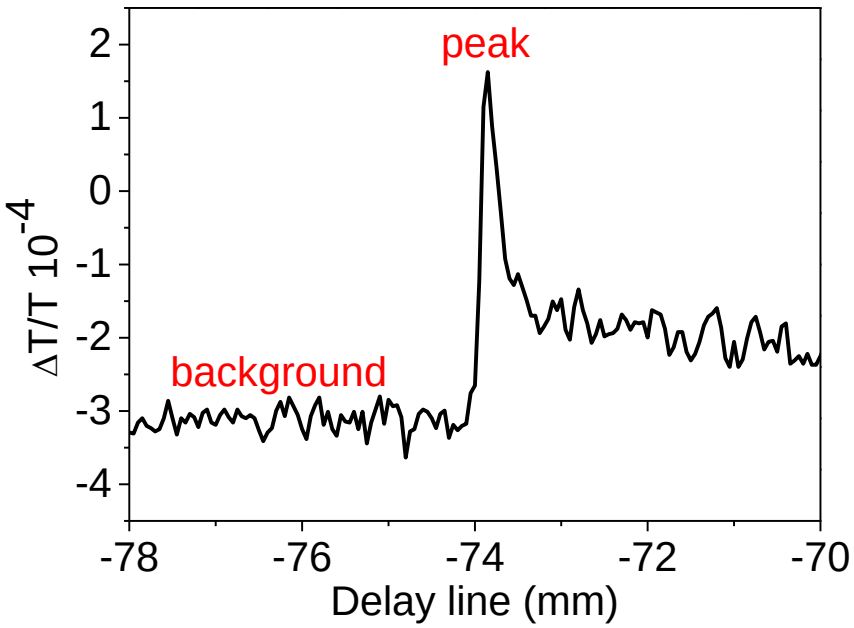

Figure 2.3. Typical output signal from the UTA experiment, obtained for HgTe QDs.

2.3.4 How are the differential spectra obtained?

The peak of the transmittance was found by carrying out a narrow UTA similar to that shown in Figure 2.3, but with fine step sizes (typically 0.04 mm) in the delay stage. The

delay stage was then positioned at the peak of the UTA, where it remains fixed whilst a differential spectrum is acquired. The differential spectrum is then ready to be measured and the spectrometer can be run over a variety of wavelengths. A scan at the required range of wavelengths at the presence of the pump at 500 Hz is then carried out, which provides a ΔT signal indicating any change in transmission caused by the pump wavelength. A scan is then run over the same wavelengths but in the absence of the pump and synchronised to the pump repetition rate, which provides the T signal. In each single point of the scan, the spectrometer takes an average of 20 readings. The ΔT signal was finally divided by the T signal in order to obtain the final shape of the spectrum. Both the ΔT and T signals are obtained via only one channel, the sample arm, with no reference beam used and hence no balance is required.

2.3.5 Interpretation of the TA signal and MEG measurements

The objective of the measurements is to examine how the population of the excited-state in a sample changes with time, controlled by the delay stage [14]. As shown in Figure 2.4(a), a typical signal obtained from a UTA experiment after processing usually shows the transmittance change through the sample induced by the pump pulses, ΔT/T, as a function of the time delay between the pump and probe beams. The transmission of the probe pulses through the sample is T, which changes when the pump interacts with the sample. The transmittance transient signal is defined as [14]

$$\frac{\Delta T}{T} = \frac{T_{with\ pump} - T_{without\ pump}}{T_{without\ pump}}$$

Equation 2.3

Two different scenarios can be distinguished here [14]. The first occurs when the probe pulses are absorbed by the state created by the pump (transmission is less), which results in a negative $\frac{\Delta T}{T}$ signal known as photo-induced absorption (PA). The second scenario occurs when the transmission of probe pulses becomes higher at the existence of the pump. In such

cases, the pump has modified the population of states and the probe pulses are able to interact with fewer states than in the absence of the pump. Here, the resultant $\frac{\Delta T}{T}$ signal is positive and the case is known as bleaching.

The analysis of the signal depends on the purpose for which the measurement is taken. It could be to obtain the lifetime of multi-excitons, which can be achieved in a straightforward manner from a fit such as that shown in Figure 2.4(a). It could also be used to study the ultrafast exciton dynamics in a more complicated way, such as by measuring MEG or the sample surface trapping. However, the analysis generally relies on the difference between the recombination rates of multiexcitons and single excitons in QDs, where it is in the range of 10-100 ps for multiexcitons or 10 ns to 1 μs for a single exciton [3]. The initial peak of the UTA signal at t=0 is proportional to the total number of excitons generated by the pump beam in both the case of MEG and if MEG does not occur. After the initial peak when the excitons created by the pump beam decay to single excitons and before these are lost, the UTA signal becomes proportional to the number of QDs originally excited by the pump beam. The ratio between the amplitude of the initial peak and the long-lived plateau $R=A/B$ therefore indicates the average number of excitons formed per QD excited by the pump per pulse. At low pump fluences, a QD will only absorb one photon per pump pulse; at such low pump fluences R can correspond to the average number of excitons generated per absorbed photon of the pump beam, which is known as the quantum yield QY [3]. Applying this to a number of pump fluences allows R to be measured for all of them. The data can then be fitted, usually versus the transmittance transient at a maximum value (sometimes versus occupation) to extrapolate to zero fluence (see Figure 2.4(b)) with [15]

$$R(J) = QY\sigma J[1 - \exp(-\sigma J)]^{-1}$$

Equation 2.4

where σ is the absorption cross-section of the QD at the pump wavelength and J is the fluence of the pump pulse. If this is completed for a specific wavelength, the QY can be extracted. For MEG measurements, QY or R were measured for at least two wavelengths, one above the MEG threshold and the other below it, with a QY value of 1 expected below the MEG threshold.

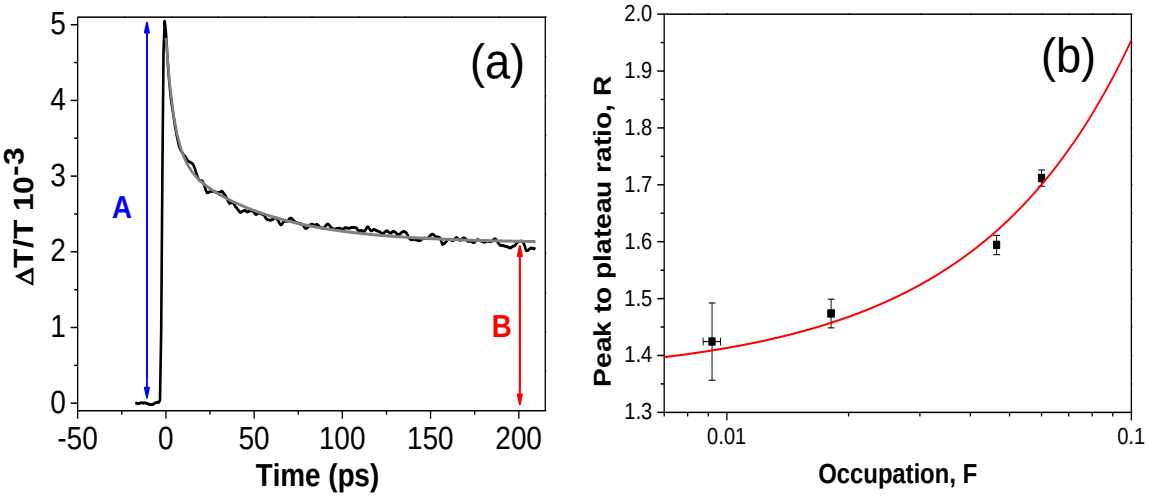

Figure 2.4 (a). Typical signal obtained from a UTA experiment shows ΔT/T, as a function of the time delay between the pump and the probe beams. A is the initial amplitude and B is the plateau. (b) R, the ratio between A and B, versus occupation for HgTe QDs photo-excited at 3.1E_g.

Multi-exciton formation can take place not only by MEG but also if multiple photons are absorbed per QD per pump pulse. In order to ensure that the excitons created are purely due to MEG, the average number of photons absorbed per QD per pulse should be much less than unity [7]. Poisson statistics govern the probability, $P(n)$, of a QD absorbing n photons per pump pulse [16] where

$$P(n) = \langle N \rangle^n \exp(-\langle N \rangle)/n! \qquad \textit{Equation 2.5}$$

The average number of photons absorbed per QD, $\langle N \rangle$, is equal to σ multiplied by J in units of photons per pulse per unit area. In practice, accurate measurement of σ is difficult; instead, the analysis relies on the determination of R in the limit of vanishing pump fluence.

2.3.6 Response of solvents and ligands to the UTA experiment

Differential spectra for the solvents and capping ligands used in this study were acquired alone so that their potential contribution to the spectra for the QD samples could be assessed. As most QDs studied were diluted in water, particular care must be taken around 950 nm, as water has a strong absorption feature in that region. Heavy water (D_2O), which is chemically identical but for which the absorption feature is significantly red-shifted, was considered as an alternative solvent if the H_2O feature was found to be obscuring details in the QD differential spectra. In Figure 2.5, it can clearly be seen that H_2O has an absorption feature starting at 920 nm and centred at ~970 nm, while D_2O absorption starts above 1250 nm. However, as the UTA experiment only measures pump-induced changes the water absorption feature should not contribute. To confirm that the feature from 900 to 1100 nm is not due to the absorption of the solvents (H_2O or D_2O if used), the pump-induced transmittance change spectra of both solvents were measured and are shown in Figure 2.6. Also shown in the same figure is the spectrum for 1-thioglycerol, which was used to passivate some of the HgTe QD samples. The pump used here was at a wavelength of 450 nm and at ~1 mW pump power. For all three, the differential spectra fluctuated around zero in this spectral region, which allowed any bleach or absorption features detected by the UTA experiment to be attributed to the HgTe QDs and not to the solvents or ligand. Furthermore, the choice of H_2O or D_2O as a solvent is confirmed not to affect the results obtained from the UTA experiment.

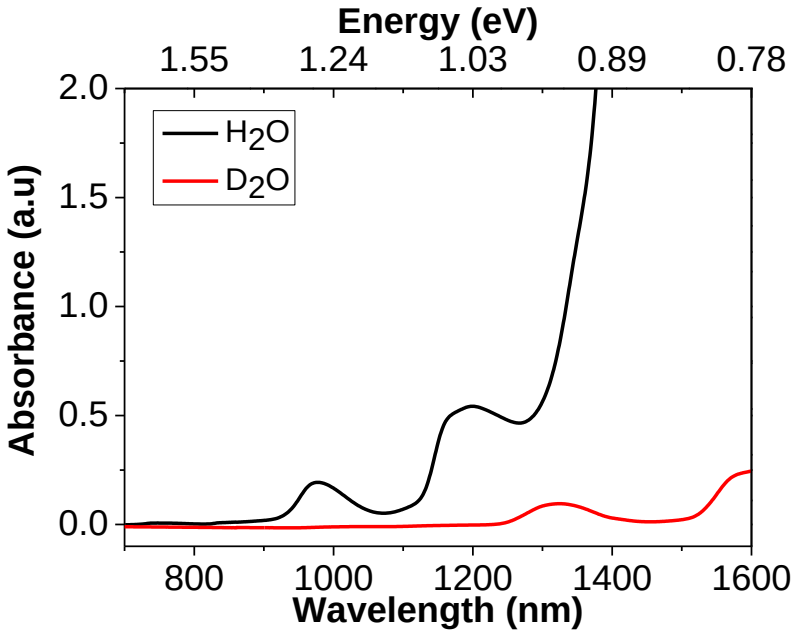

Figure 2.5. Steady state absorption spectra for H_2O (black) and D_2O (red).

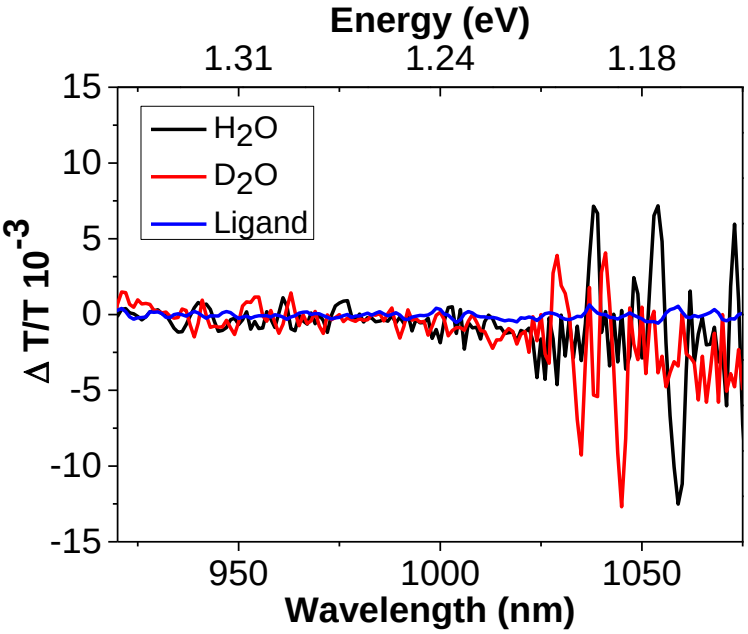

Figure 2.6. Transmittance change spectra induced by 450 nm (differential spectra) of solvents H_2O (black) and D_2O (red), and the ligand [1-thioglycerol] (blue).

Similarly, the pump-induced transmittance change, $\Delta T/T$, spectra for the solvents and the ligands used for MPA-capped HgTe QDs were examined. Figure 2.7 shows these spectra when photo-exciting with ~1 mW of power pump at 400 nm. The spectra show no response over the range shown, indicating that any feature over this range in the HgTe QDs spectra is purely due to the QDs rather than the solvent or ligands.

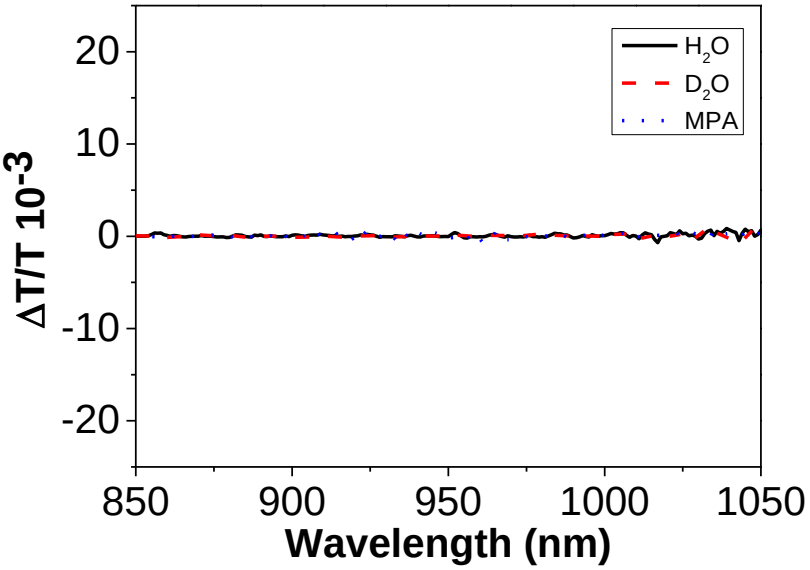

Figure 2.7. Pump-induced transmittance change, ΔT/T, spectra taken with 400 nm pump wavelength of MPA (blue), H_2O (black), and D_2O (red).

As part of this study, DDT-capped HgTe QDs were examined for their ultrafast charge dynamics. The solvent used with these QDs was toluene and its pump-induced transmittance change, $\Delta T/T$, spectrum was examined as shown in Figure 2.8. Clearly, the solvent has no response over the shown spectral region, confirming that any response to the UTA experiment is due to HgTe QDs alone.

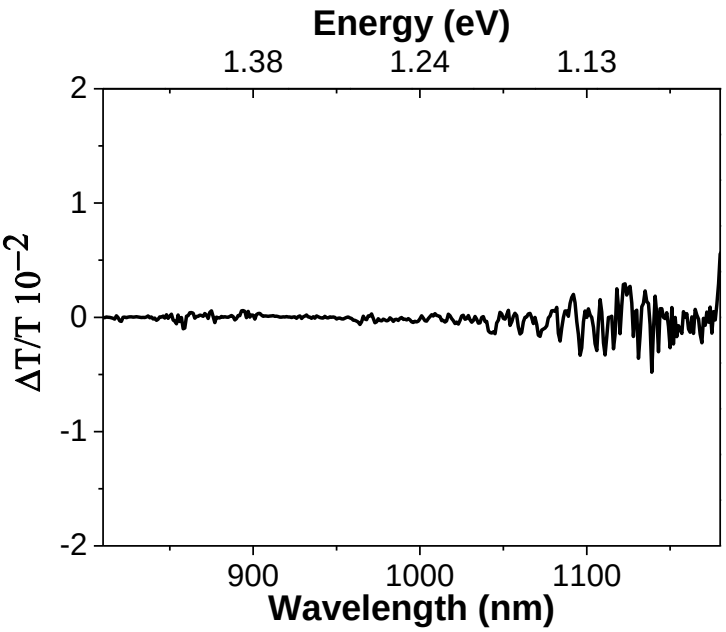

Figure 2.8. Pump-induced transmittance change, ΔT/T, spectrum of toluene taken with 400 nm pump wavelength.

The $Cd_xHg_{(1-x)}Te$ alloy QDs studied in Chapter 4 were passivated with tetrachloroethylene (TCE). Figure 2.9 shows the pump-induced transmittance change, $\Delta T/T$, spectrum obtained for this ligand. The spectrum shows a feature with a peak positioned at 1000 nm. This is associated not with state filling but rather is a residual fundamental in the frequency doubled pump wavelength used (500 nm), which was sometimes seen in the experiment. Otherwise, no response over the spectral region was shown, confirming that any features that appeared for UTA measurements are due to the response of the $Cd_xHg_{(1-x)}Te$ alloy QDs alone.

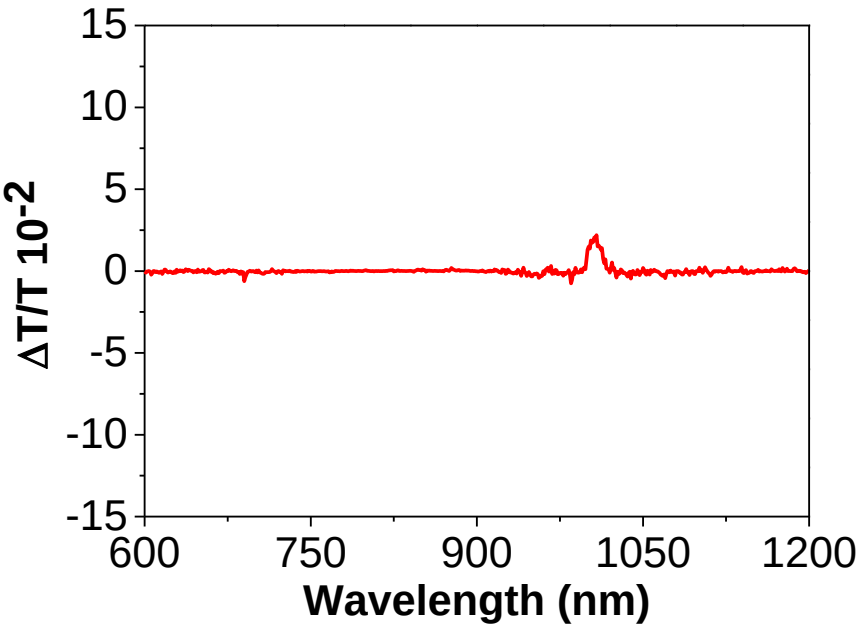

Figure 2.9. Pump-induced transmittance change, ΔT/T, spectrum of ligand, TCE, taken with 500 nm pump wavelength. The feature at 1000 nm is due to the residual fundamental in the frequency doubled pump wavelength used (500 nm).

In Chapter 5, the plasmon ultrafast dynamics for TiO_2-Au samples, which were diluted in water, were examined. Figure 2.10 shows the pump-induced transmittance change, $\Delta T/T$, spectrum of the solvent used (deionised water) for excitation at a wavelength of 370 nm with an average pump power of 1 mW. It can be seen that the solvent shows no response over this spectral region, allowing any response to the UTA experiment to be attributed to the TiO_2-Au samples.

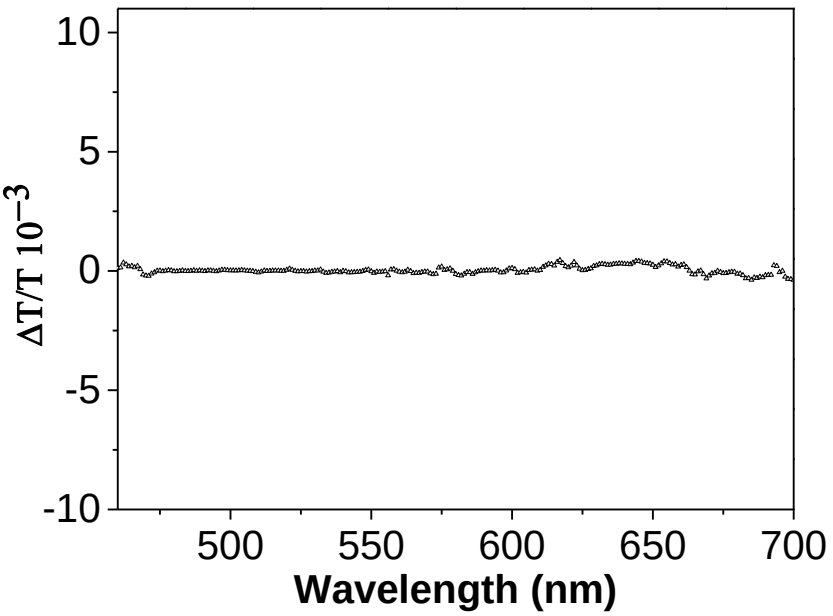

Figure 2.10. Pump-induced transmittance change, $\Delta T/T$, spectrum of water for a 370 nm excitation wavelength and an average pump power of 1 mW.

2.4 Summary

The spectroscopic methods used for sample characterisation throughout the study have been described in this chapter. The UV/Vis/NIR spectrometer (Lambda 1050) and the Horiba Jobin Yvon Fluorolog (iHR(FL3-22)) spectrofluorometer were the commercial instruments used throughout this study for steady state and PL spectra measurements respectively. UTA spectroscopy is a pump-probe experiment used to investigate the ultrafast dynamics of charges and a detailed description of its laser system and the optical bench layout was provided. This chapter described how both the UTA signal and pump-induced transmittance change spectra were obtained in addition to the interpretation of the signals. It concluded by covering the investigation of the UTA experiment response to the solvents and ligands used in the samples.

2.5 References

1. Starna Cells, I., *Catalog and Price List*, Starna, Editor. 2014: Atascadero. p. 12.
2. Tkachenko, N.V., *Optical Spectroscopy: Methods and Instrumentations*. 1st ed. 2006, Oxford: Elsevier. 307.
3. Binks, D.J., *Multiple exciton generation in nanocrystal quantum dots - controversy, current status and future prospects.* Physical Chemistry Chemical Physics, 2011. **13**(28): p. 12693-12704.
4. Klimov, V.I., *Spectral and Dynamical Properties of Multiexcitons in Semiconductor Nanocrystals.* Annual Review of Physical Chemistry, 2007. **58**(1): p. 635-673.
5. Nozik, A.J., *Multiple exciton generation in semiconductor quantum dots.* Chemical Physics Letters, 2008. **457**(1-3): p. 3-11.
6. Nozik, A.J., et al., *Semiconductor Quantum Dots and Quantum Dot Arrays and Applications of Multiple Exciton Generation to Third-Generation Photovoltaic Solar Cells.* Chemical Reviews, 2010. **110**(11): p. 6873-6890.
7. Smith, C. and D. Binks, *Multiple Exciton Generation in Colloidal Nanocrystals* Nanomaterials, 2013. **4**(1): p. 19-45.
8. Kim, J.Y., et al., *25th Anniversary Article: Colloidal Quantum Dot Materials and Devices: A Quarter-Century of Advances.* Advanced Materials, 2013. **25**(36): p. 4986-5010.
9. Hardman, S.J.O., et al., *Electronic and surface properties of PbS nanoparticles exhibiting efficient multiple exciton generation.* Physical Chemistry Chemical Physics, 2011. **13**(45): p. 20275-20283.
10. Stubbs, S.K., et al., *Efficient carrier multiplication in InP nanoparticles.* Physical Review B, 2010. **81**(8): p. 081303.
11. Cadirci, M., et al., *Ultrafast exciton dynamics in InAs/ZnSe nanocrystal quantum dots.* Physical Chemistry Chemical Physics, 2012. **14**(43): p. 15166-15172.
12. Cadirci, M., et al., *Ultrafast exciton dynamics in Type II ZnTe-ZnSe colloidal quantum dots.* Physical Chemistry Chemical Physics, 2012. **14**(39): p. 13638-13645.
13. Al-Otaify, A., et al., *Multiple exciton generation and ultrafast exciton dynamics in HgTe colloidal quantum dots.* Physical Chemistry Chemical Physics, 2013. **15**(39): p. 16864-16873.
14. Snedden, E., *Experimental investigations of excited-state dynamics in conjugated polymers using time-resolved laser spectroscopy*, in *Physics*. 2011, Durham University: Durham. p. 273.
15. Beard, M.C., et al., *Multiple Exciton Generation in Colloidal Silicon Nanocrystals.* Nano Letters, 2007. **7**(8): p. 2506-2512.
16. Klimov, V.I., ed. *Semiconductor and Metal Nanocrystals*. 2004, Marcel Dekker: New York. 484.

Chapter 3 Ultrafast charge dynamics in HgTe QDs

3.1 Introduction

This chapter presents and discusses the results obtained for HgTe QDs using 1-thioglycerol, mercaptopropionic acid (MPA), and dodecanethiol (DDT) as ligands. It starts with information regarding the chemical formulae of the ligands and a brief account of the samples under study. The presentation of the results begins with an initial characterisation of the samples which includes a comparison of a calculated absorption spectrum with the experimental data. It then presents the pump-induced transmittance change spectra and excitonic dynamics obtained using ultrafast transient absorption spectroscopy. The chapter discusses the possible underlying mechanisms: trion formation, photoinduced absorption and MEG. It relates the results to the ligand chemical structure. The chapter also identifies MEG for the first time in HgTe QDs and also shows how a result can be mistaken for MEG if other recombination processes are not considered. The chapter ends with a summary of the results.

3.2 Ligands used in the samples under study

The surface of QDs has a strong chance of developing trap states due to unsaturated bonds. Therefore, QDs are usually passivated with organic ligands, which couple to QDs either gaining or losing charge [1]. However, the choice of ligand is crucial, as some have the ability to better control surface trap states. As a result, the ultrafast charge dynamics of the system might change and some relaxation processes could be favoured over other mechanisms. Therefore, here we compare ultrafast charge dynamics in HgTe QDs capped with three different ligands: 1-thioglycerol, MPA and DDT. The structures of these molecules are shown in Figure 3.1.

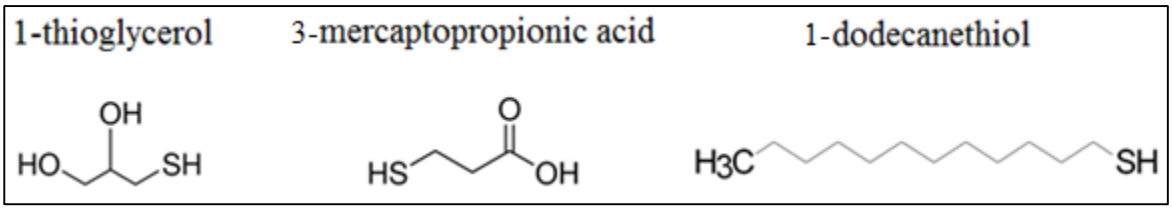

Figure 3.1 Chemical structure of the ligands used to passivate HgTe QDs

The HgTe QDs used here were synthesised by Dr S. V. Kershaw, our collaborator from the Centre for Functional Photonics, Department of Physics and Material Science at City University, Hong Kong. The synthesis process of HgTe QDs is described in detail elsewhere [2], but a brief description is given here. Water was used as a solvent for both 1-thioglycerol and MPA-capped QDs in the synthesis process, which started with preparing a ligand aqueous solution. The next step was to add some mercury perchlorate and then HgTe QDs were allowed to grow with the use of hydrogen telluride. In comparison, the DDT-capped HgTe QDs were not synthesised directly but by ligand exchange, HgTe QDs are instead first synthesised in water with short-chain ligands, such as 1-thioglycerol, which can then be partially exchanged by the long-chain ligand DDT in order to be dissolved in toluene [3]. For optical studies, the samples were prepared in 10 mm cuvettes. The synthesised solutions were diluted with solvents so that the band-edge absorbance was ~0.2-0.5.

3.3 Electronic characterisation of the samples

3.3.1 MPA-capped HgTe QDs

The absorption and PL spectra for a typical sample of MPA-capped HgTe QDs were initially measured to characterise the electronic structure of the sample. Figure 3.2 shows both spectra: the absorption (in black) and the PL (in red). Note that the PL was measured by Dr S. V. Kershaw using an Edinburgh Instruments F900 fluorescence spectrometer equipped with a Hamamatsu InP/InGaAs photomultiplier tube. It is clear that the PL peak lies at ~1176 nm and has a full width half maximum (FWHM) of about 200 nm, whereas the

absorption spectrum has a broad shoulder with a 200-300 nm Stokes shift from the PL peak to the shorter wavelengths. The second derivative of this shoulder was found to have a minimum of approximately 900 nm, which indicates the presence of a peak (see Figure 3.3). A comparison with research published in 2006 [4] and 2012 [5], which studied the relationship between the size of HgTe QDs and their PL peaks or band edges, allowed us to estimate the average size of the MPA-capped HgTe QD diameter to be in the range of 3-4 nm. A theoretical model which calculated the energy gap as a function of the diameter of spherical HgTe QDs in 2012 [6] also supports our estimation of the size of the QDs under study.

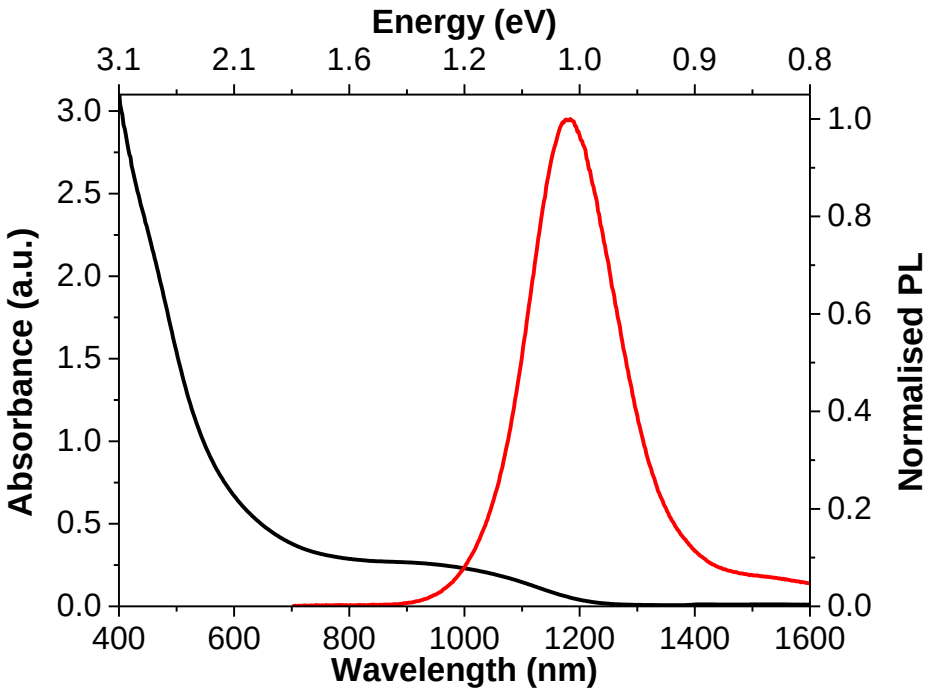

Figure 3.2 Absorbance (black) and PL (red) spectra of MPA-capped HgTe QDs

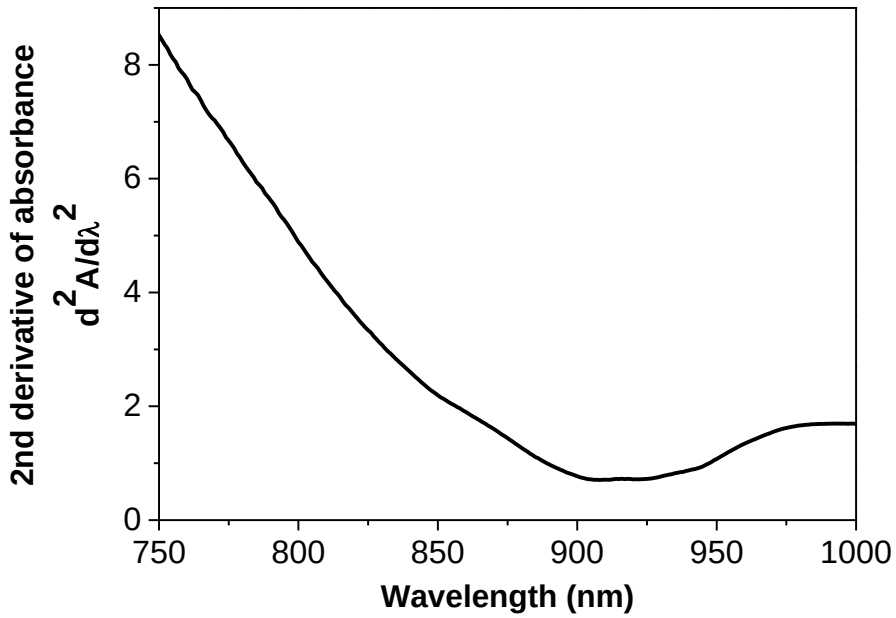

Figure 3.3 Second derivative of the absorbance spectrum shown in Figure 3.2

Allan and Delerue applied the same tight-binding model [6] to calculate the density of states, the absorption and PL spectra for a single spherical HgTe QD with a diameter of 3.5 nm corresponding to a band edge of 1.0 eV. The absorption and PL spectra, taking into account the dispersion of the sizes in an ensemble of QDs, were calculated using the Allan-Delerue single QD data by broadening the individual transitions with Gaussian peaks. The peak width, w, was increased linearly with E, the energy as shown in Equation 3.1:

$$w = a + b(E - E_1)$$

Equation 3.1

where a and b are fitting parameters, and E_1 is the energy of the band-edge transition. Figure 3.4 a) shows the calculated density of states, while b) shows the absorption and PL spectra for a single spherical HgTe QD with a diameter of 3.5 nm and also for an ensemble of QDs with spectra broadened by the size dispersion.

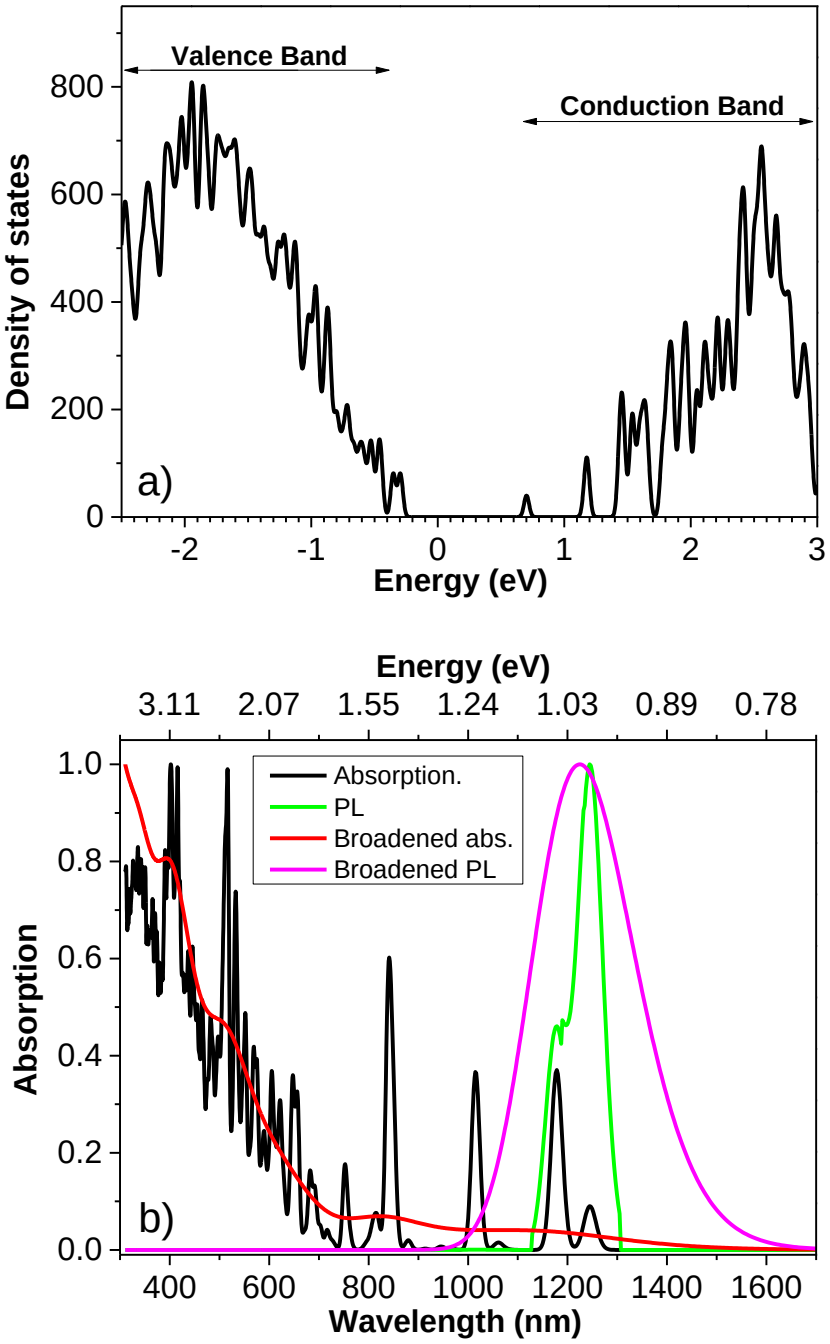

Figure 3.4 Calculated a) density of states, and b) absorption and PL spectra for HgTe QDs; the black and green lines represent the spectra for a single QD of 3.5 nm diameter, whereas the red and pink lines correspond to an ensemble of QDs with an average diameter of 3.5 nm but whose spectra are broadened by size dispersion.

As can be seen from Figure 3.4 a), the VBM and CBM are separated by 1.0 eV, which is the band gap of the QDs, and it is clear that the CBM has a relatively low density and has significantly lower energy than CBM-1, the next-lowest conduction band state. In comparison, the valence band states are much more closely spaced, in particular the states at

and near the VBM. Furthermore, the density of the valence band states grow broader the further they are from the VBM. As a result of this band structure, we should see evidence of their effect on the absorption and PL spectra. Figure 3.4 b) shows this effect and, specifically, the relatively weak transition from VBM to CBM (i.e., the absorption at the band edge) for a single QD as well as the excellent agreement between the spectra calculated for the ensemble of HgTe QDs and the experimental spectra shown in Figure 3.2 for MPA-capped HgTe QDs. The absorption shoulder in Figure 3.4 occurs at an energy that allows transitions from VBM to CBM-1 or to the CBM but from deeper within the valance band. The strong agreement between theory and experiment gives us confidence in the theoretical model used for calculation and also in our experimental results. It also enables us to attribute a value of 1.0 eV to the band edge of the sample under study. Therefore, the PL spectrum shown in Figure 3.2 is attributed to a band edge, i.e., CBM-to-VBM transition, whereas the peak of the absorption shoulder is attributed either to a transition from VBM to CBM-1 or to a CBM transition but from deeper within the valance band (or to a combination of both).

As further investigation, the pump-induced transmittance change, $\Delta T/T$, spectrum for a sample of MPA-capped HgTe QDs taken at the time when it was at its maximum amplitude (typically a few picoseconds after pumping) was measured and is shown in Figure 3.5. The pump wavelength used was 400 nm with ~1 mW power. State-filling produces a positive $\Delta T/T$, which is called a bleach, in the transmittance spectrum of QDs. The bleach depends on both the absorption cross-section at the probe wavelength and the occupation of the states involved. It is always at its maximum after the cooling of the photogenerated charges to the band edge has taken place but before the occurrence of any significant recombination. The spectrum shown in Figure 3.5 has relatively weak bleaching at the band edge at 1176 nm (~1 eV) but a much stronger bleach is evident at wavelengths corresponding to the absorption shoulder peak. This result agrees well with the dependence

of absorption strength on wavelength calculated in Figure 3.4 and also reveals that the absorption shoulder corresponds to a transition involving either VBM or CBM because charge cooling is complete by this time and hence other states in the conduction and valance bands are unoccupied by electrons and holes, respectively.

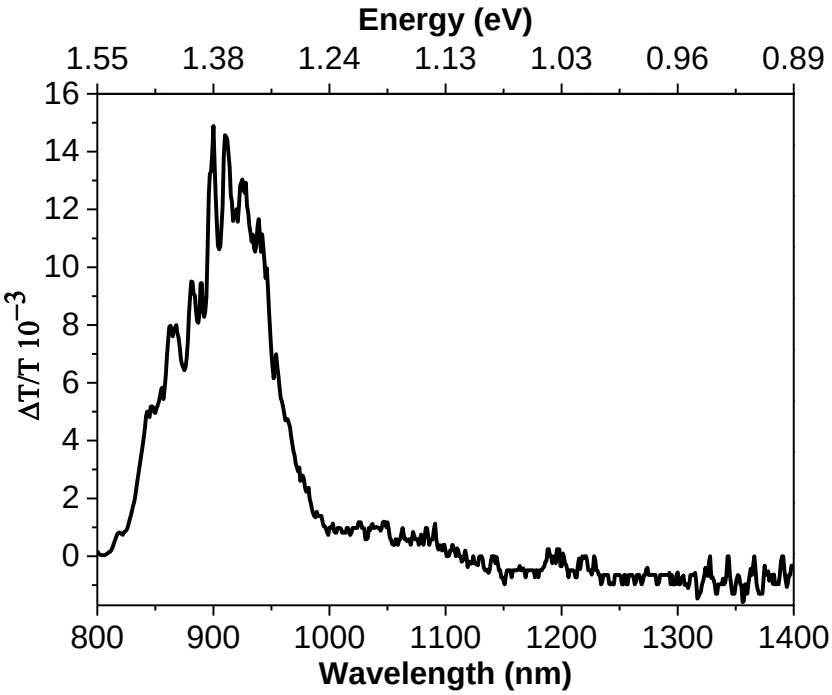

Figure 3.5 Pump-induced transmittance change, ΔT/T, spectrum of MPA-capped HgTe QDs taken with a 400 nm pump wavelength

3.3.2 1-thioglycerol-capped HgTe QDs

Three different samples of thioglycerol-capped HgTe QDs of different sizes were studied at different times during the research period. Figure 3.6 shows the measured absorption spectra for the three samples of HgTe QDs, named 1, 2 and 3. Also shown is the PL spectrum for sample 3; the others arrived at a time when the spectrofluorometer accessories used to measure such a range of PL were not available.

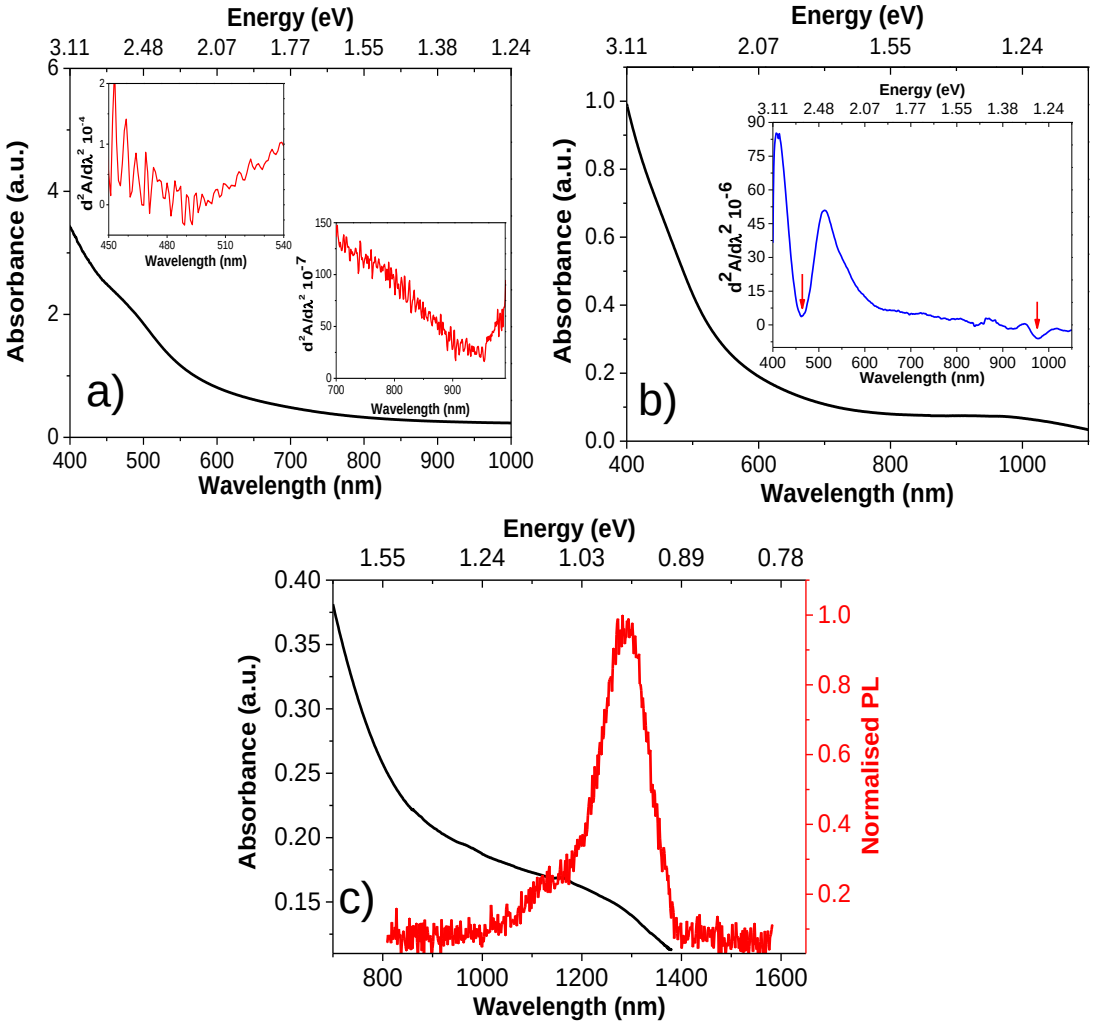

Figure 3.6 Measured absorption spectra for a) sample 1, b) sample 2 and c) sample 3 of thioglycerol-capped HgTe QDs. Insets are the second derivative of absorbance for samples 1 and 2 showing the first two transitions. The PL spectrum is shown for sample 3.

The absorption spectra have a common shape, broad and featureless, which suggests that we have a large size distribution. Hence, the second derivative of absorbance was investigated. Insets in Figure 3.6 a) and b) are the two minimum features obtained from the second derivative of absorbance, revealing the positions of the first two energy levels: ~1.3 eV and ~2.53 eV for sample 1 (i.e., ~950 and ~490 nm, respectively), and ~975 nm and ~460 nm for sample 2, indicated by red arrows in Figure 3.6 b), which correspond to ~1.3 eV and ~2.7 eV, respectively. In comparison, we could not extract the absorption edge position for sample 3 even from the second derivative of absorbance. However, its PL spectrum has a distinct peak centred at ~1290 nm (0.96 eV), indicating the band edge transition, as shown

in Figure 3.6 c). Our observations for samples 1 and 2 are consistent with $E_{ehp}(1P_h1P_e)$ being about $2E_{ehp}(1S_h1S_e)$ in HgTe QDs [7] i.e., the first minimum of the second derivative of the absorbance has energy that is almost half that of the second minimum.

The absorption spectrum was calculated by Allan and Delerue for a single spherical HgTe QD with a band gap of 1.3 eV, as shown in Figure 3.7. The spectrum shows a very weak transition at the band edge, indicating that the shoulder seen in the experimental spectrum is due to the next-highest transition, similar to the results reported for HgTe QDs passivated by MPA ligands [2] (discussed above). We then broadened, with individual Gaussian peaks, the individual transitions in this spectrum to take into account the size dispersion in an ensemble of QDs. The width of the peak was broadened to 50% of the transition energy providing the spectrum shown in red in Figure 3.7. The second derivative of this broadened absorption spectrum (shown in blue in Figure 3.7) was then found to simulate the experimental procedure. The lowest energy minimum in this broadened spectrum, which has an energy almost half that of the second one, was found to correspond, not to the weak band-edge transition, but rather to the stronger next-highest transition. This confirms that the band-edge transition is obscured by the stronger next-highest transition in our experimental data.

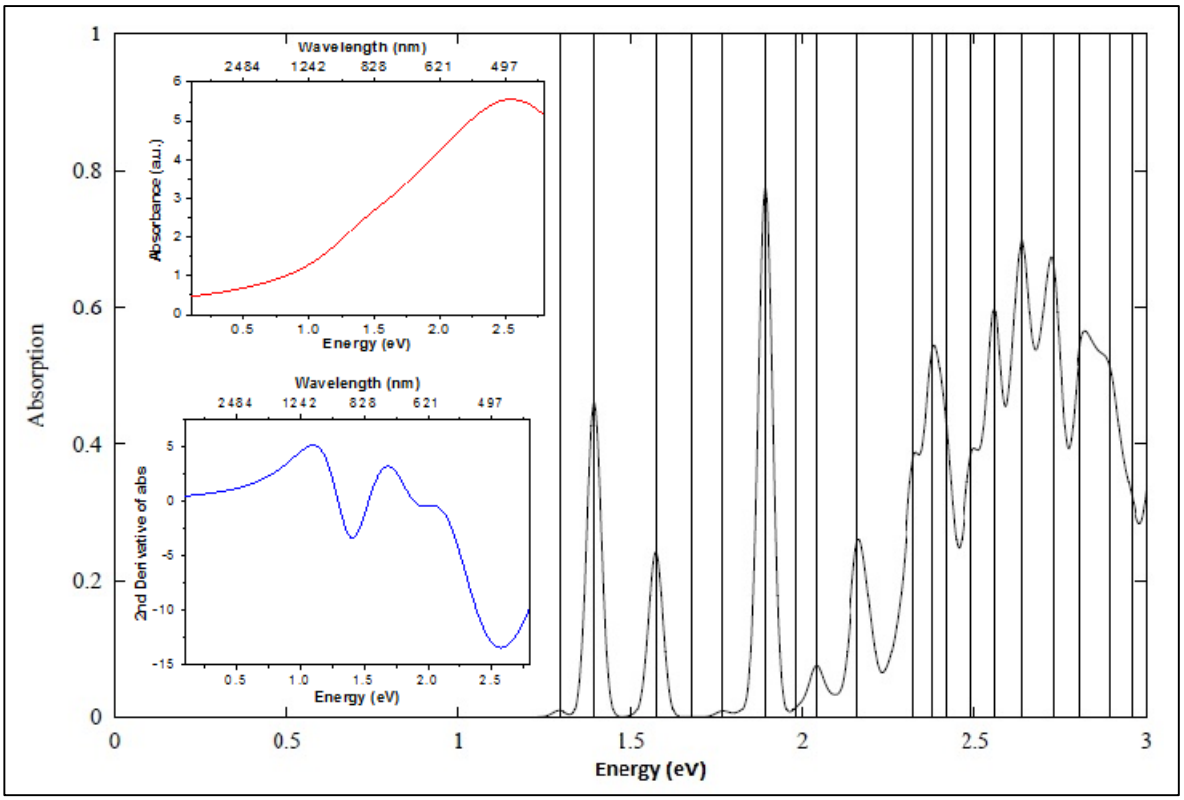

Figure 3.7 Calculated absorption spectrum for a single HgTe QD with a broadened absorption (red) and its second derivative (blue)

The pump-induced transmittance change spectra of thioglycerol-passivated HgTe QDs (also called the differential spectra) were measured at the time when they are at their maximum amplitude i.e., ~6 ps after pumping. Figure 3.8 shows the differential spectra of samples 1 (smoothed), 2 and 3 when pumped with ~1 mW of 450 nm, 390 nm and 400 nm wavelengths, respectively. In general, the shapes of these spectra are similar i.e., broad features of absorption but with bleaches seen at positions that correspond to the first minima of the second derivative of absorbance indicated by red arrows in Figure 3.8. The broad features can be seen from 900 nm to 1100 nm for sample 1, 850 nm to 1100 nm for sample 2, and 800 nm to 1150 nm for sample 3. Note that the $\Delta T/T$ signal obtained is the net effect of the photoinduced absorption and the bleach, which oppose each other; in other words, pump-induced absorption competes with pump-induced transmission and whichever dominates will determine the overall effect. Therefore, the bleach features (seen as a reduction in absorption indicated by red arrows) are attributed to state-filling, where all

photogenerated charges have cooled down to the band edge but no significant recombination has taken place at this early time.

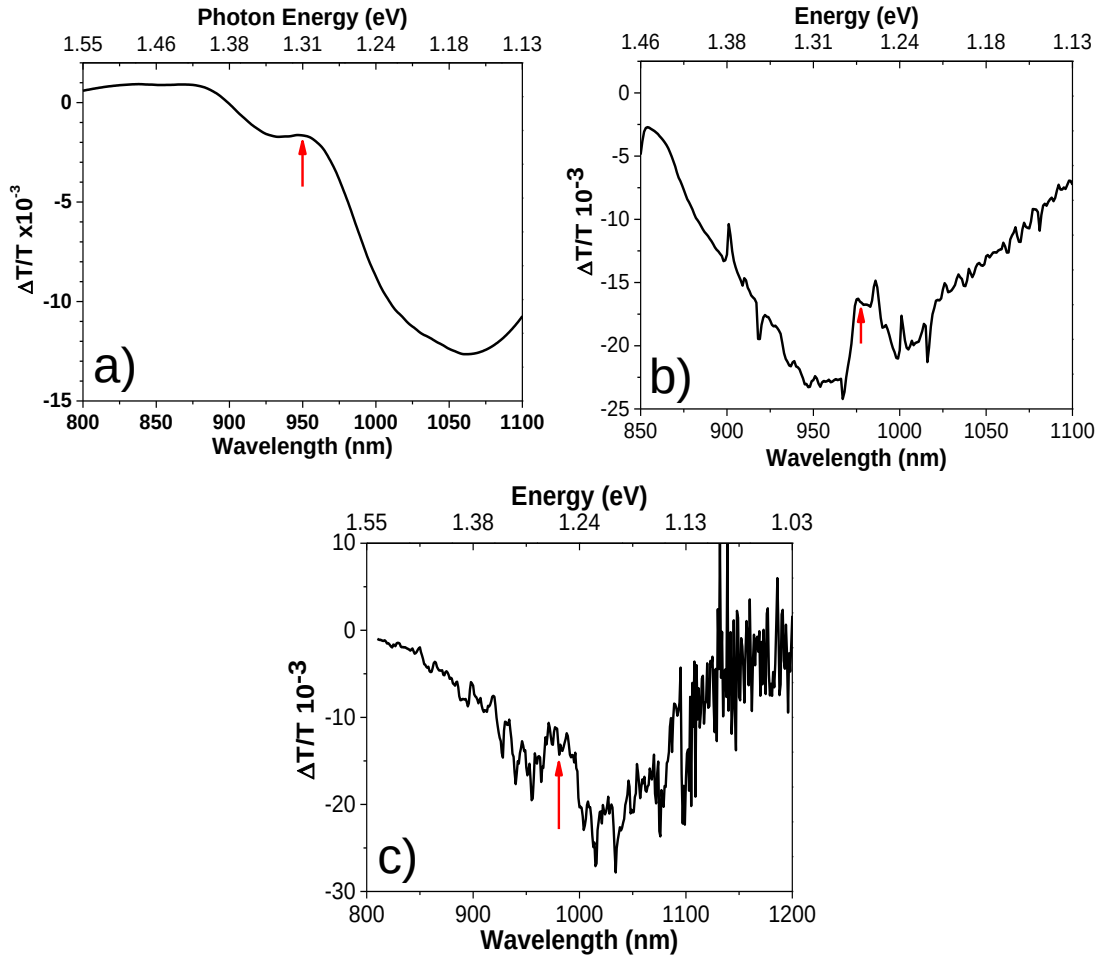

Figure 3.8 Pump-induced transmittance change spectra (differential spectra) of a) sample 1, b) sample 2 and c) sample 3 of thioglycerol-capped HgTe QDs. The red arrows indicate the bleaches at 950 nm, 975 nm and 980 nm for samples 1, 2 and 3, respectively.

A recent study investigated the response of HgTe CQD films [8] to n-and p-type charging. The difference spectra for the films when subject to negative and positive electrochemical potentials were measured, revealing a bleach at the 1S position due to state-filling but found to be coincident with PA. Therefore, we can similarly describe the spectra shown in Figure 3.8 as bleaches at the 1S position of thioglycerol-capped HgTe QDs samples superimposed with a broad photoinduced increase in the absorption spectra. Such behaviour was also observed for Type II ZnTe–ZnSe colloidal quantum dots, destroying the symmetry of the bleach and almost diminishing its positive value [9], but in our study the bleach for

HgTe QDs is obscured by PA to a higher degree. A possible explanation for this PA behaviour is excited state absorption (ESA) enabled by surface trapped charges, similar to that observed in CdSe CQDs [10]. In ESA, an exciton is created by a pump, then the probe excites the charge previously created by the pump to the continuum of the CB (a process that would be forbidden in an ideal case). However, it becomes no longer forbidden due to the modification of the selection rules by the presence of the trapped charge, which disturbs the electronic symmetry of the QD, enabling the ESA.

3.3.3 DDT-capped HgTe QDs

Figure 3.9 shows the absorption (in black) and PL (in red) spectra for a typical sample of DDT-capped HgTe QDs. It can be seen that the PL spectrum has a peak at ~1280 nm (~0.97 eV) and an FWHM of about 200 nm (similar to that of MPA-capped HgTe QDs), whereas the absorption spectrum shows a broad shoulder shifted by 200-300 nm from the PL peak to shorter wavelengths. Following comparison with the literature [4-6], this allows the estimation of the average diameter of a DDT-capped HgTe QD to be between 3 and 4 nm.

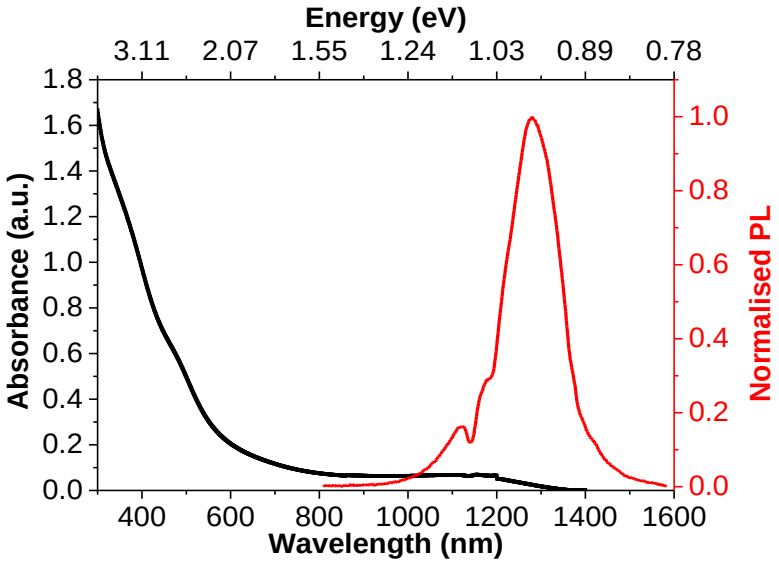

Figure 3.9 Absorbance (black) and PL (red) spectra of DDT-capped HgTe QDs

To investigate this sample further, Figure 3.10 shows the pump-induced transmittance change, $\Delta T/T$, spectrum taken a few picoseconds after pumping. A bleach is clearly seen at wavelengths corresponding to the absorption shoulder peak ~1055 nm (~1.18 eV). A differential spectrum due to state-filling only should be positive and symmetrical and similar in width to the PL peak and 1S spectra feature [11]. However, this spectrum has some features that appear just before the bleach, which is a sign of absorption (reduction in transmission) and this disturbs its symmetry. Destroying the symmetry of the differential spectrum suggests that the PA is overlapping with the bleach in this sample due to surface charge trapping.

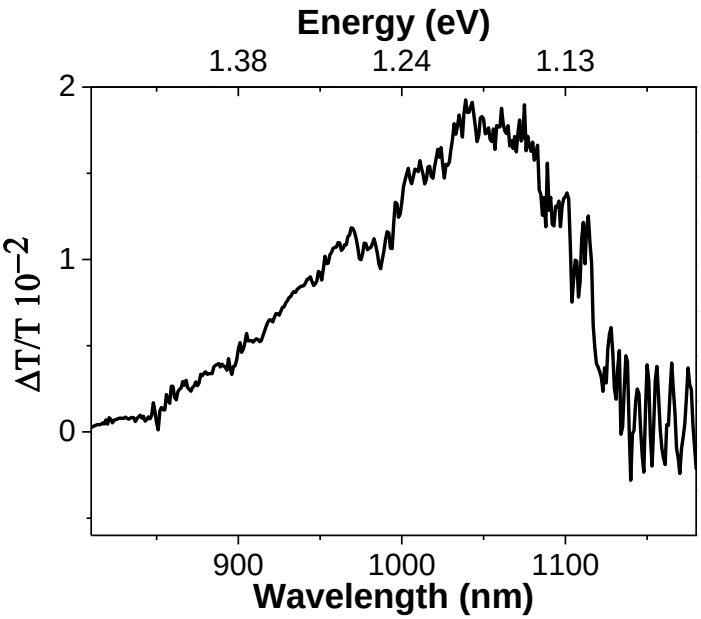

Figure 3.10 Pump-induced transmittance change, ΔT/T, spectrum of DDT-capped HgTe QDs taken with a 400 nm pump wavelength

3.4 Excitonic dynamics of HgTe QDs

3.4.1 MPA-capped QDs

The initial optical characterisation of the HgTe QD samples provided us with the 1S positions and thus the probe wavelengths to be used for the study of the dynamics of CBM electrons. To understand these dynamics in MPA-capped HgTe QDs, the transmittance

transients were measured when probing at 900 nm and pumping at 800 nm using average pump powers of 0.7, 1.5, and 2.5 mW, as shown in Figure 3.11.

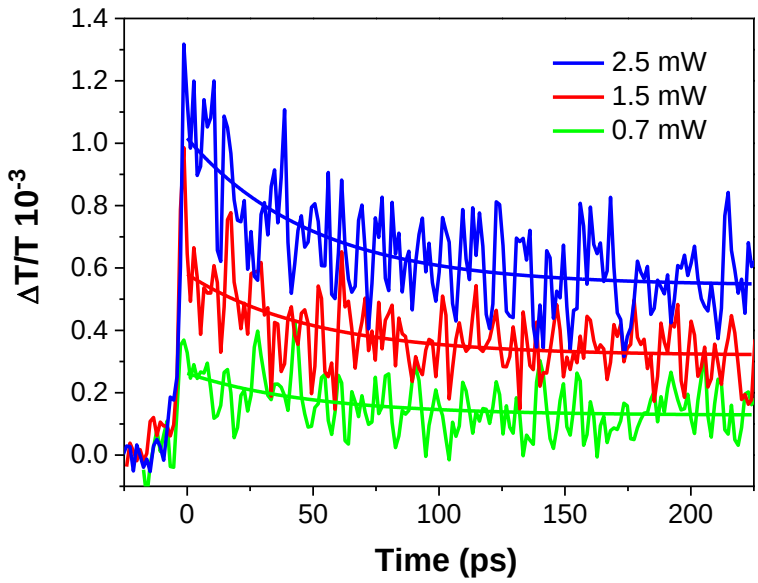

Figure 3.11 Transmittance transients at a probe wavelength of 900 nm for the MPA-capped HgTe QDs induced by pump beams of the powers shown in the legend and of wavelength 800 nm. The fits to the data shown are global and for a mono-exponential decay to a plateau with a time constant of 49 ps.

The initial decrease of the bleach peak to a plateau is described by a mono-exponential decay with a time constant of 49±5 ps. The fits to the data shown are global using the function

$$\frac{\Delta T(t)}{T} = y_0 + A_1 e^{-t/\tau_1}$$

Equation 3.2

where y_0 is the plateau which represents the single long-lived exciton signal, A_1 is the amplitude of the transient component, and τ_1 is the decay lifetime. The 800 nm wavelength used in Figure 3.11 is below the MEG threshold, based on Equation 1.5, and hence bleach transients produced by a shorter pump wavelength, corresponding to above the MEG threshold, were also investigated. Similar transients were obtained at a wavelength of 400 nm for a series of pump powers when using 900 nm as a probe beam (see Figure 3.12). Their global fit using Equation 3.2 yielded a time constant of 49±2 ps, as before. Figure 3.12 also shows a comparison between decays obtained for static and stirred samples at both 0.4 mW and 2 mW. When higher pump powers were used, the form of the transient decay changed

as it developed an additional initial decline of significant amplitude in the first 5 ps, indicating the presence of another process under these conditions. The decay of the transient is now no longer described as mono-exponential but rather as bi-exponential in the form

$$\frac{\Delta T(t)}{T} = y_0 + A_1 e^{-t/\tau_1} + A_2 e^{-t/\tau_2}$$

Equation 3.3

where A_1 and A_2 are the amplitudes of the transient components and τ_1 and τ_2 are the lifetimes of the decay. When fitting the transient with this function, one of the time constants was fixed at the bi-exciton lifetime for this sample, i.e., 49 ps, which gave the additional time constant a value of 4.7±0.2 ps under the conditions used. The green fit in Figure 3.12 is bi-exponential, with the specified time constants for the transient obtained for 2 mW of pump power and a stirred sample.

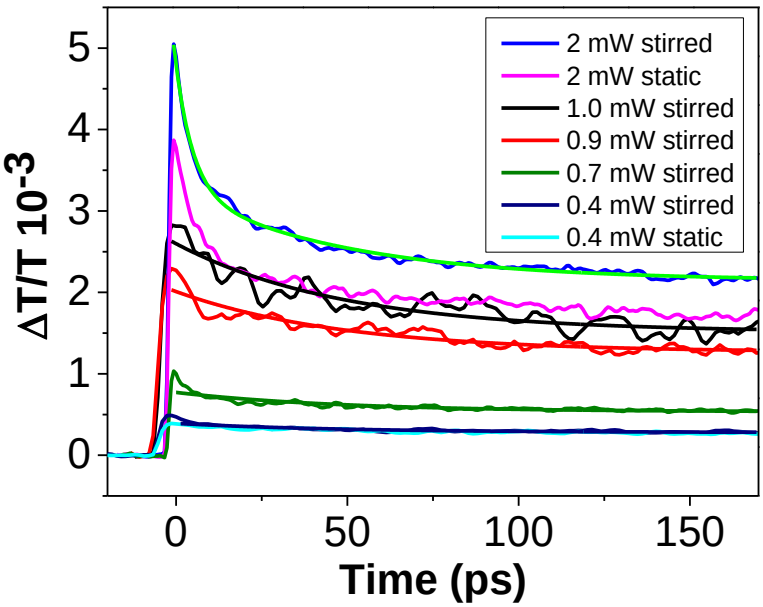

Figure 3.12 Fractional transmittance change, ΔT/T, transients induced in HgTe QDs by a pump beam of wavelength 400 nm with the range of average powers shown in the legend. A global mono-exponential fit to the decays up to 1 mW power is also shown, yielding a time constant of 49 ps. It also compares decays obtained for static and stirred samples at both 0.4 mW and 2 mW. The transient for 2 mW pump power and a stirred sample also includes a bi-exponential fit shown in green yielding time constants of 4.7±0.2 ps and 49±2 ps.

3.4.2 Thioglycerol-capped QDs

Figure 3.13 shows the pump-induced fractional transmittance transients for different pump powers for a sample of thioglycerol-capped HgTe QDs taken when pumped at wavelengths of a) 450 nm and b) 390 nm. A global fit to these transients is also shown yielding a bi-exponential decay with time constants of 25±1 and 3±1 ps.

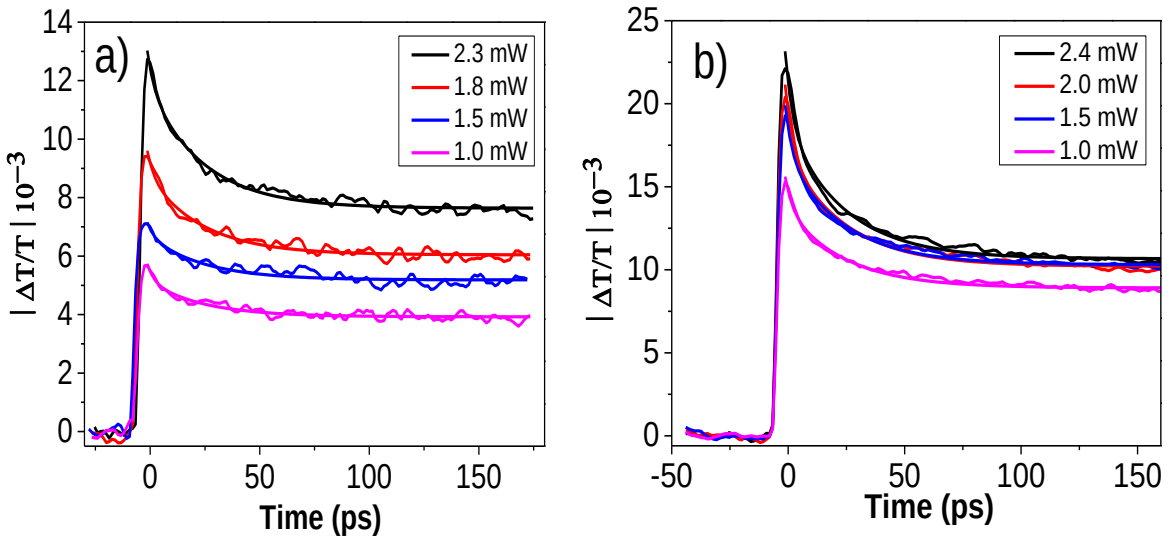

Figure 3.13 Fractional transmittance transients for a sample of thioglycerol-capped HgTe QDs at the different pump fluences shown in the legends when probing at 975 nm and pumping at a) 450 nm and b) 390 nm. The global bi-exponential fits shown give time constants of 25±1 and 3±1 ps.

However, away from the bleach, the behaviour of the transmittance transients is different. Figure 3.14 shows the transients when probing away from the bleach i.e., 1000 nm and photoexciting with a) 390 nm and b) 490 nm. These transients are described by mono-exponential decay with a time constant of 25±1 ps. This means that when PA is dominant (at a probe wavelength of 1000 nm) the decay of the transients is described by only one lifetime, but when the bleach competes with the absorption at the 1S position the decay is described by two lifetimes, the first of which corresponds to PA.

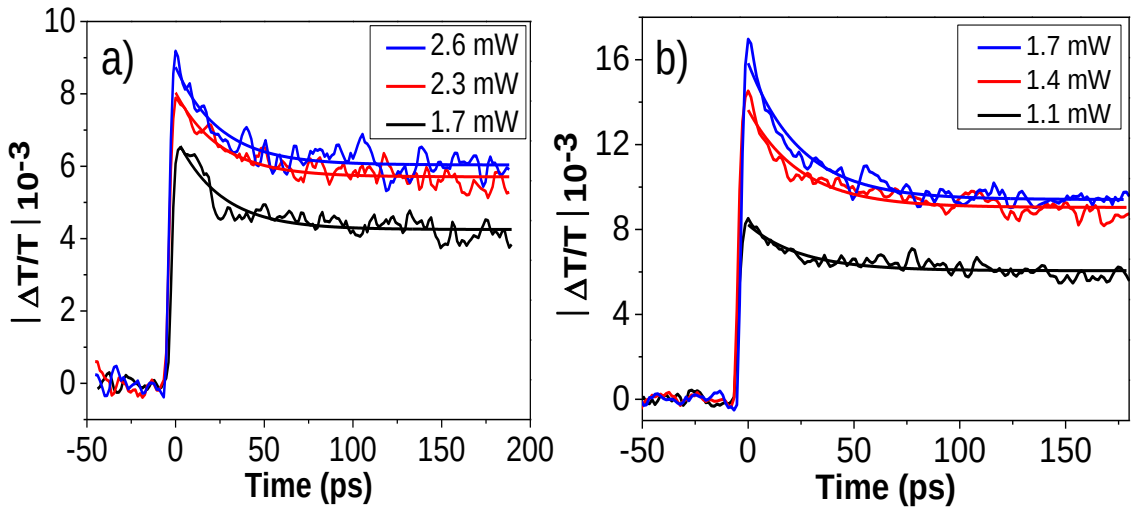

Figure 3.14 Fractional transmittance transients for a sample of thioglycerol-capped HgTe QDs at the different pump powers shown in the legends when probing at 1000 nm and pumping at a) 390 nm and b) 490 nm. The global mono-exponential fits shown give a time constant of 25±1 ps.

For further investigation, a comparison is made between the pump-induced transmittance transients of the sample in two conditions: static and stirred. Figure 3.15 shows the fractional transmittance transient induced by 1 mW of 390 nm for a static sample, a vigorously stirred sample (i.e., 1000 rpm), and a sample stirred more gently (i.e., 500 rpm). There is no significant difference between the transients, indicating that trion formation is eliminated in these QDs.

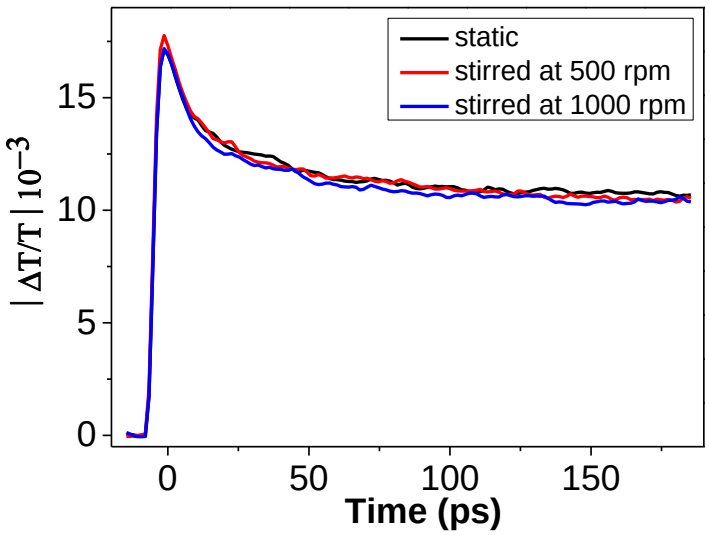

Figure 3.15 Comparison of transients for static (black) and stirred (at 500 rpm [red] and 1000 rpm [blue]) samples of thioglycerol-capped HgTe QDs when probed and pumped with 975 nm and 390 nm, respectively. The power of the pump was ~1 mW.

3.4.3 DDT-capped QDs

The transmittance transients of the bleach for this sample were measured when probing at 1037 nm. The sample was pumped at 800 nm, which is below the MEG threshold, using average pump powers of 0.65, 1.05, and 1.40 mW, resulting in the transients shown in Figure 3.16. The decrease of the bleach peak to the plateau is well-described by a mono-exponential and a global fit to these transients yields a time constant of 25±1 ps. Similar transients were also obtained for 400 nm, above the MEG threshold, at a range of pump powers of between 0.4 mW and 1 mW when probing at 1055 nm. A global fit to these transients also yielded a time constant of 25±1 ps. Note that the data for pump powers above 1 mW starts to deviate from the mono-exponential decay fit at the peak, indicating the onset of another process; in other words, the stirring was not enough to eliminate trion formation at high pump powers. (Similar behaviour was seen for MPA-capped HgTe QDs at high pump powers in Figure 3.12.)

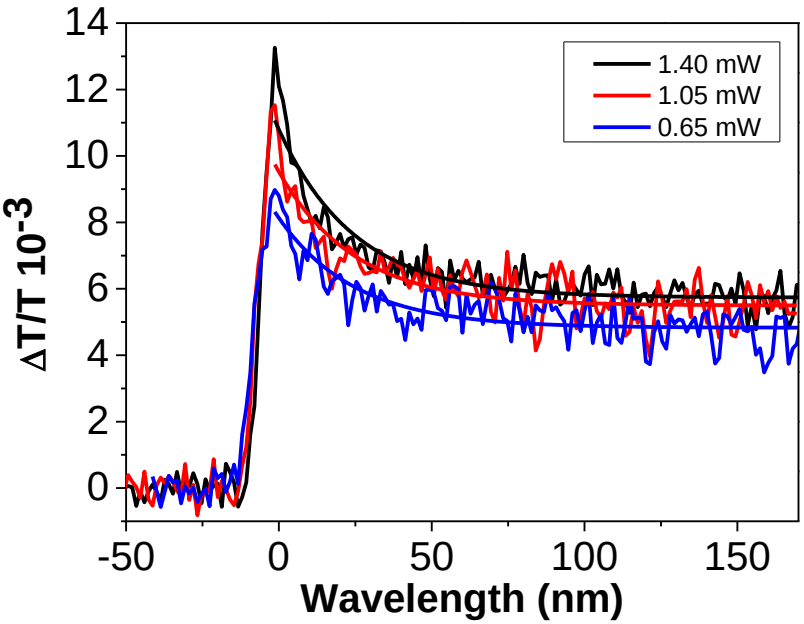

Figure 3.16 Transmittance transients obtained for DDT-capped HgTe QDs when pumping and probing at 800 nm and 1037 nm, respectively. The pump powers are shown in the legend and the global fit to the data shown is mono-exponential with a 25 ps time constant.

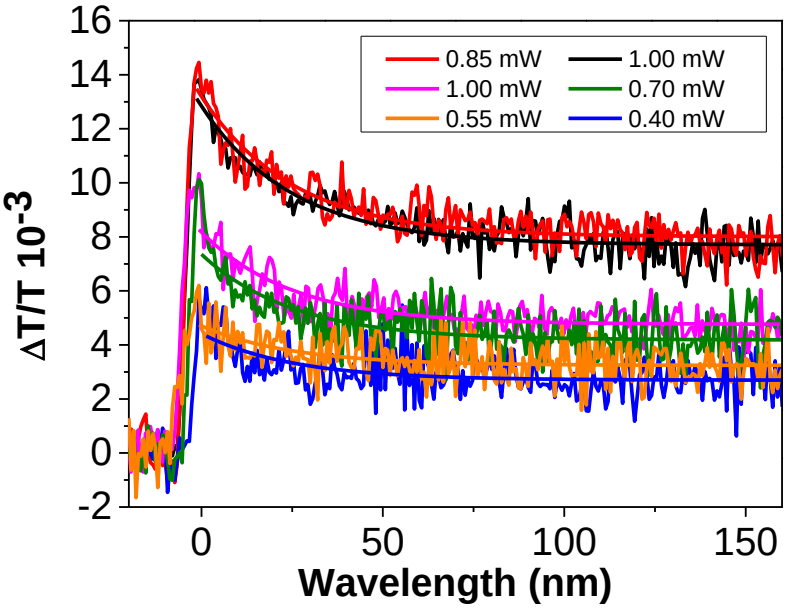

Figure 3.17 Fractional transmittance change, ΔT/T, transients for DDT-capped HgTe QDs induced by 400 nm with the range of average powers shown in the legend. A global mono-exponential fit to the decays is also shown, yielding a time constant of 25 ps.

A comparison between transients obtained for static and stirred samples of DDT-capped HgTe QDs is shown in Figure 3.18. The pump wavelength used was 400 nm at 1 mW power. No significant difference between the transients is seen, indicating that trion formation is eliminated in these QDs.

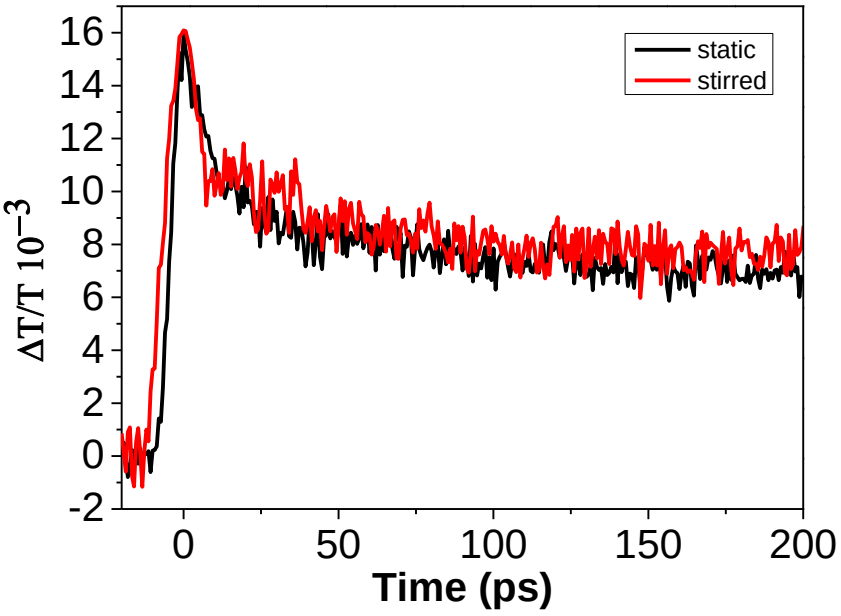

Figure 3.18 Comparison of pump-induced transmittance transients for 1 mW pump power at a wavelength of 400 nm obtained for static and stirred samples of DDT-capped HgTe QDs.

3.5 Discussion of the possible mechanisms

In order for transmittance transients for these HgTe QDs to be understood, different possible mechanisms for such sub-ns decay, including bi-exciton formation either by MEG or by the absorption of multi-photons, trion formation and direct surface trapping, must be considered. These mechanisms are discussed in detail below for each sample discussed above.

3.5.1 MPA-capped QDs

The average number of photons absorbed per QD per pump pulse, $< N >$, is given by [12]

$$< N >= \sigma J$$

Equation 3.4

Lhuillier *et al*. [5] have studied the optical properties of HgTe colloidal quantum dots and determined the absorption cross-section at the absorption edge to be ~1.5×10^{-15} cm^2. However, the optical density of our samples was measured to be 10 times greater at 400 nm than at the absorption edge, hence we estimate σ ~1.5×10^{-14} cm^2 for a pump wavelength of 400 nm. The fluence of the 400 nm pump pulse is calculated (assuming that the pump spot is uniformly circle) as follows.

At an average pump power of 1 mW, for example, which corresponds to the largest amplitude transient mono-exponential fit (shown in black) in Figure 3.12, the energy per pulse is 10^{-3} (W) / 500 (Hz) = 2 µJ and the energy of the photon at 400 nm, $E_{ph}(400)$, is $3.105\times1.6\times10^{-19} = 5\times10^{-19}$ Joule. The number of photons per pulse is energy per pulse / $E_{ph}(400)$ = 2 µJ / 5×10^{-19} J = 4×10^{12} and the diameter of the pump is ~3.5 mm, which means that the area of the pump spot size is $\pi\times(0.175)^2$ = 0.096 cm^2. Hence, the fluence, J, which is equal to the number of photons per pulse / the area of the pump = 4×10^{12} / 0.096 was

estimated to be 4.2×10^{13} photons/cm^2/s. Now we have both the absorption cross-section at the pump and the fluence, which allows us to apply Equation 3.4 and this yields $< N >$ ≈0.6. We can use this value of $< N >$ to calculate the expected value of R, the ratio of the peak amplitude to the plateau if the decay of the transients of 1 mW power and less in Figure 3.12 is due to bi-exciton recombination, as in [13]

$$R = QY\langle N\rangle[1 - \exp(-\langle N\rangle)]^{-1} \approx QY\left[1 + \frac{\langle N\rangle}{2}\right]$$

Equation 3.5

where QY corresponds to the average number of excitons generated per absorbed photon and has a value of 1 without MEG, and greater than 1 with MEG. Note that the approximate expression on the right-hand side is valid for $\langle N\rangle \ll 1$. For $\langle N\rangle$ ~0.6, Equation 3.5 gives R/QY a value of ~1.3 as R is estimated to be ~1.6, that is consistent with the value of the QY observed experimentally of ~1.3 (see discussion in section 3.7.1 below). These initial results of the transients and calculations allow us to attribute the decay of the pump-induced transients shown in Figure 3.12 to the recombination of bi-excitons, with a lifetime of 49±2 ps. The plateau value of the transients is attributed to the remaining single excitons, the lifetime for which is typically longer than 1 ns in QDs [14]. The low $\Delta T/T$ values for these $\langle N\rangle$ in Figure 3.12 suggests that the VBM to CBM-1 transition is the dominant one at the absorption shoulder rather than to CBM, because, as shown in Figure 3.4, VBM has a significantly greater density of states than CBM, which results in a lower occupation and, therefore, bleach for the same value of $\langle N\rangle$.

We stated earlier an initial identification of multi-exciton recombination as the process responsible for the transmittance transients shown in Figure 3.12. However, a number of studies in different types of QDs, including CdSe [10, 15], InAs/ZnSe [16], ZnTe/ZnSe [9], and PbSe [17, 18] have shown that there are two other processes which can

lead to sub-nanosecond decays similar to that shown in Figure 3.12 with a similar time scale: trion decay and direct surface trapping. In the former, a charge is trapped on the QD surface for a period of time longer than that between pump pulses, while the geminate charge remains within the volume of the QD. Therefore, when a photon of a subsequent pump pulse is absorbed, a trion is created from the exciton just formed and the geminate charge. Trions can recombine and produce transient decays similar to that of a bi-exciton with a similar lifetime. However, it was found that vigorous stirring or flowing of the sample has the power to reduce or eliminate trion formation [17-19]. In our sample, we saw from Figure 3.12 that the difference between the stirred and static transients is evident at high pump powers, resulting in the bi-exponential decay form at these excitation rates. However, at low pump powers the transients for stirred and static samples have no significant difference between them, possessing the mono-exponential form of decay even for the static sample, allowing us to exclude trion decay as the cause of the transients of 1 mW power and less shown in Figure 3.12.

The other possible process is direct surface trapping, in which electrons or holes are trapped on a surface state from the conduction or valence bands, respectively. This can reduce the state-filling and thus cause decay similar to that of bi-exciton recombination with a similar lifetime and is characterised by the presence of PA i.e., a negative $\Delta T/T$ or a reduction in the transmittance spectrum, near to the band edge [9, 10, 16]. However, our observation has shown no sign of any PA in the sample (see Figure 3.5), also allowing us to exclude direct surface trapping as the cause of the transients shown in Figure 3.12. Thus, the above discussion, coupled with the consistency of the observed value of R with $\langle N \rangle$ calculation, allows us to conclude that for the MPA-capped HgTe QDs and at low pump powers, bleach decay is dominated by bi-exciton recombination, whereas trion recombination also becomes significant at high pump powers.

3.5.2 Thioglycerol-capped QDs

MEG can occur at pump energies above a photon energy threshold. This is almost ~480 nm for thioglycerol-capped HgTe QDs (see Equation 1.5). However, our investigations have shown that transmittance transients corresponding to pump wavelengths of 390 nm and 490 nm for a sample of thioglycerol-capped QDs exhibited no significant differences, as shown in Figure 3.19. In an ideal case, increasing the pump energy should result in an increase in the corresponding R value, which is not the case here. Hence, it is concluded that MEG is not significant here under the experimental conditions used.

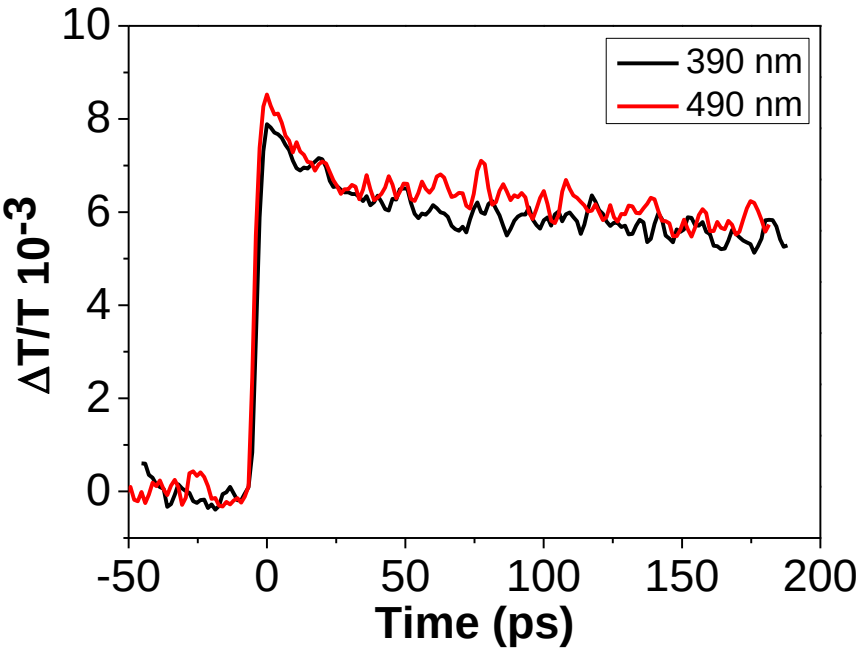

Figure 3.19 Comparison of two transmittance transients for HgTe QDs with a 975 nm band gap at two different pump wavelengths: 390 nm and 490 nm

Trion formation could be the reason for the transmittance obtained for these samples. However, the transmittance transient for stirred samples is comparable to that of static samples, as seen in Figure 3.15, which suggests that the transients observed are not associated with long-lived surface trapping of photogenerated charges. A study in 2011 [10] showed that direct surface trapping is associated with a large PA and non-mono-exponential bleach decay for CdSe QDs, which is consistent with our observation here i.e., bi-

exponential bleach decay and a large and broad PA. Furthermore, the lifetime obtained for CdSe QDs in that study was 30 ps, which is comparable with the lifetimes obtained by us for thioglycerol-capped HgTe QDs. Thus, we attribute the transmittance transients observed for HgTe QDs capped by 1-thioglycerol ligands to direct surface trapping, by which charges after photoexcitation cool to the band edge filling some of the states and hence reducing the absorption, and the decay represents the emptying of these states due to trapping to surface states.

3.5.3 DDT-capped QDs

DDT-passivated HgTe QDs can be considered as a case between MPA-capped ones which are free of any PA detected near the 1S position and those capped with thioglycerol which exhibit PA significantly greater in magnitude than the bleach. However, the question now is what governs the decay of the transients in Figure 3.17? We have seen no significant difference between the transients of the stirred and static samples in Figure 3.18 which allows us to exclude trion formation as the cause of the transients. The decay lifetime is similar to that of thioglycerol-capped QDs and comparable with the previously reported CdSe QDs [10]. In addition, the drop seen in the differential spectrum just before the bleach (Figure 3.10) is a sign of PA. We have also never seen only a plateau in transients that are below the MEG threshold (Figure 3.16). Furthermore, the lifetime obtained for these QDs is 25 ps, which is shorter than that obtained for the MPA-capped QDs of 49 ps, while they are slightly bigger in size as they have a longer PL wavelength and hence should have a longer lifetime. All these reasons suggest direct-surface trapping to be behind the transients in Figure 3.17.

We are confident of our conclusion regarding these QDs but, in order to be more precise, we now discuss the third possible mechanism: MEG. These QDs are a good example

of how MEG can be overestimated (see section 3.7.2). The value of $< N >$ was measured as done for MPA-capped QDs but here the optical density was measured as 14 times greater at 400 nm than at the absorption edge, hence we estimated σ ~2.1×10^{-14} cm^2 for a pump wavelength of 400 nm. Equation 3.4 yields a value of $< N >$ ~0.88 for 1 mW pump power and hence R can be calculated from Equation 3.5 if the decay of the transients is due to bi-exciton recombination. Calculations give R/QY a value of ~1.5 and R has a value of ~1.6 at 1 mW (see Figure 3.17), suggesting a QY of ~1.1. However, the experimental result of the quantum yield (discussed in section 3.7.2) is inconsistent with the one calculated. This contradiction is strong evidence for omitting MEG as the cause of the transients' decay in Figure 3.17.

3.6 Chemical structure and surface states

We now turn our attention to discussing the reason behind the better passivation achieved by using MPA as the surface ligand rather than thioglycerol or DDT, as evidenced by the absence of both PA and trap-related decay processes for the MPA-capped QDs. QD passivation depends on the relative ability of a ligand to exchange electron density with the trap site [1]. In this section, we will relate the degree of passivation achieved by the different ligands to their ability to donate charge to the QDs, as quantified by the zeta potential for the QD-ligand complex, following a suggestion by S. V. Kershaw [20].

The HgTe QDs under study are formed with a 1.3 to 1.4 Hg/Te ratio, as determined by inductively coupled plasma-atomic emission spectroscopy, resulting in a metal-rich surface that can lead to a net positive charge [20]. This net positive charge is offset by negative charges acquired from the ligands used for passivation. In this case, the Hg^{2+} in the QDs binds with the thiolate group, $-S^-$ (formed by deprotonation of the thiol group, -SH, at the high pH used) which all the ligands used possess (see Figure 3.1). However, the positive

charge from the metal rich QD and the negative charge from the thiolate groups do not necessarily completely balance giving the QD-ligand complex a net charge. Indeed, an overall charge on the QD-ligand complex helps to keep the QDs apart i.e., preventing aggregation. The relative ability of the ligands to increase the negative charge of the complex will be used as a measure of how well they are donating electron density to the trap sites associated with the unsaturated Hg. This charge can be described in terms of zeta potential, which we will use to explain why MPA-capped QDs performed better than the others in terms of QD surface passivation.

Zeta potential is a measure of the charge on the surface of QDs [21] and determines the stability of the colloidal dispersion [22]. The charges carried by a QD-ligand complex are distributed around the QDs with some attached to the QD surface. Increasing the concentration of the charges on the surface influences the distribution of the remaining ions in the surrounding medium, resulting in an electrical double layer. The first layer is composed of ions strongly bound to the QD, while the second layer, which is adjacent to the first, is of less firmly bound ions. The second layer has an imaginary boundary in which, if the QD moves, the ions also move with it, while beyond it the ions do not move. The potential at this boundary is known as the zeta potential [22]. The zeta potential, ζ, can be measured using a light-scattering technique in which QD electrophoretic mobility, μ_e, defined as the travel velocity of a QD divided by the applied electric field, is related to the zeta potential by [21]

$$\mu_e = \frac{2\varepsilon\zeta f(ka)}{3\eta}$$

Equation 3.6

where ε is the dielectric constant, ζ is the zeta potential, (ka) is typically 1.5 for an aqueous solution or 1 for a non-polar solution, and η is the medium viscosity. The instrument used

consists of a laser beam split into two arms: one passes through the sample, while the other is a reference beam. The scattering light at a specific angle is collected, detected and then processed in a computer program to measure the electrophoretic mobility and thus the zeta potential.

The zeta potential was reported for HgTe QDs passivated with thioglycerol [23] as having a value of -28.1 mV. The more negative the value of the zeta potential, the more negative the ions surrounding the QDs. The literature contains no single study investigating zeta potential for MPA- or DDT-capped HgTe QDs. However, the study for HgTe QDs [23] also studied the zeta potential for a dihydrolipoic acid (DHLA) passivated sample – the structure of which is given below in Figure 3.20.

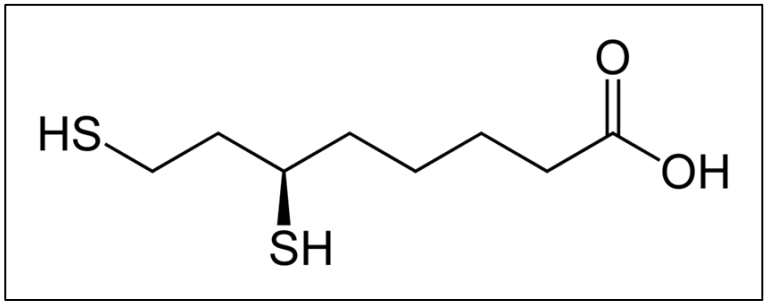

Figure 3.20 Chemical structure of dihydrolipoic acid (DHLA) ligand.

DHLA has a carboxylic acid group similar to that of MPA and hence both are expected to have a broadly similar zeta potential value, since they both combine thiolate group(s) with a carboxyl group, $-COO^-$, i.e. a deprotonated carboxylic acid group [21]. The reported value for DHLA was -43.4 mV, significantly more negative than thioglycerol [23]. The study also showed that DHLA passivation resulted in a longer PL lifetime than for capping with thioglycerol, indicating a reduced amount of the non-radiative recombination associated with traps and hence better passivation.

The zeta potential for CdTe nanocrystals passivated with MPA was measured to be -37.5 mV at 12 pH [24]. This high negative value was found to coincide with the presence

of the carboxyl group in the ligand. A study of CdTe QDs synthesised in water capped with thioglycolic acid (TGA) ligands measured their zeta potential [25]. It has found that TGA ligands resulted in a zeta potential value of -50 mV at 10 pH which was attributed to the negative carboxyl group. It should be noted that TGA and MPA are of the same family, with MPA having one more CH_2. Not only do the zeta potential measurements support our findings, but the PL QY and lifetime measurements do also. One study compared CdTe NCs capped with TGA to those with MPA [26]. PL lifetime measured for MPA and TGA-passivated CdTe NCs were similar and the PL quantum yield was comparable, which could explain how both ligands have the same way of capping the surface and suppressing trap states. The study compared TGA-capped CdTe PL quantum efficiency with that of thioglycerol-capped. A ligands/Cd ratio of 1.3:1 resulted in 40-60% quantum yield for TGA while thioglycerol was just 25%, which means that TGA resulted in better passivation and fewer trap states. The above discussion suggests that MPA ligands worked best in the passivation of HgTe QDs due to their carboxylic acid group which enables them to donate more charge density to the trap sites.

3.7 MEG

3.7.1 MPA-capped QDs

To create an additional eh pair by MEG, the conservation of energy should be applied. This means the threshold pump photon energy required to form one additional pair in Equation 1.5 is at least equivalent to twice the band edge ($2E_g$), and each additional pair above that requires further energy at least equal to the band edge. At this limit, if the photon energies are between $2E_g$ and $3E_g$, then MEG can result only in the formation of a bi-exciton. The bi-exciton then decays into a single exciton on a sub-nanosecond time scale (10s of ps). Therefore, the form of the transmittance transients from the peak to a plateau observed for

low pump fluences is demonstrated as a sub-nanosecond mono-exponential decay. Low pump fluences correspond to a negligible probability of a QD absorbing more than one photon per pump pulse, as at high pump fluences a bi-exciton can also be formed by the absorption of two photons per QD per pump pulse. Furthermore, vanishing the pump fluences in Equation 3.5, and, therefore, the value of $\langle N \rangle$, allows the R value to become equivalent to the QY, with a value greater than 1 corresponding to MEG.

MEG can be confused with other processes, such as trion decay and direct surface trapping. However, our analyses have shown that the sample under study is free of any PA and its transient decays at sufficiently low pump fluences are also free of trion formation. Hence, MEG in these HgTe QDs can be reliably identified and its resulting quantum yield confidently assessed from the vigorously stirred samples throughout the experiment (at low pump powers to ensure that no bi-exciton was formed by absorbing two photons per QD per pump pulse). MEG assessment is also limited to the transients with peaks that decay mono-exponentially to a plateau with a constant lifetime (or just a plateau, as in the case of low fluence pumping below the MEG threshold).

The occurrence of MEG in the literature has been identified by one of two methods. The first method is to compare transients pumped at photon energies above and below the MEG threshold but at similar levels of average excitation, i.e., $\langle N \rangle$ [27], while the second method relies on deducing MEG from the R values obtained from the transients over a range of excitation levels and extrapolating to a vanishing pump fluence [13]. However, the pump-induced fractional transmittance change, $\Delta T/T$, depends on both $\langle N \rangle$ and the sample optical density at the pump wavelength [2], as seen below in Equation 3.7

$$\frac{\Delta T}{T} = \frac{A_{pr}}{A}\frac{\langle N \rangle}{g}(1 - e^{-A})$$

Equation 3.7

where A_{pr} and A are the sample absorbance at the probe and the pump wavelengths, respectively, and g is the degeneracy of the conduction band minimum. Therefore, if the first method is used, we need to take into account the variation of the absorbance of the sample at the pump wavelength, A, and hence ensure that the excitation levels below and above the MEG threshold wavelengths are indeed comparable. Equation 3.7 explains the dependence of $\Delta T/T$ on arbitrary values of A (without it, it is necessary to prepare a new sample for each pump wavelength keeping the concentration of each adjusted to compensate for any increase in the absorption coefficient due to decreasing the wavelength and hence A becomes the same for both). This allows us to express the transmittance transients in terms of only the occupation of the probed state, $F = \langle N \rangle / g$ and hence to compare the transients obtained for different pump wavelengths directly. The inset in Figure 3.21 shows such a comparison of occupation transients resulting from pump beams of the same power but for different wavelengths, corresponding to excitation below ($1.6E_g$) and above ($3.1E_g$) the MEG threshold.

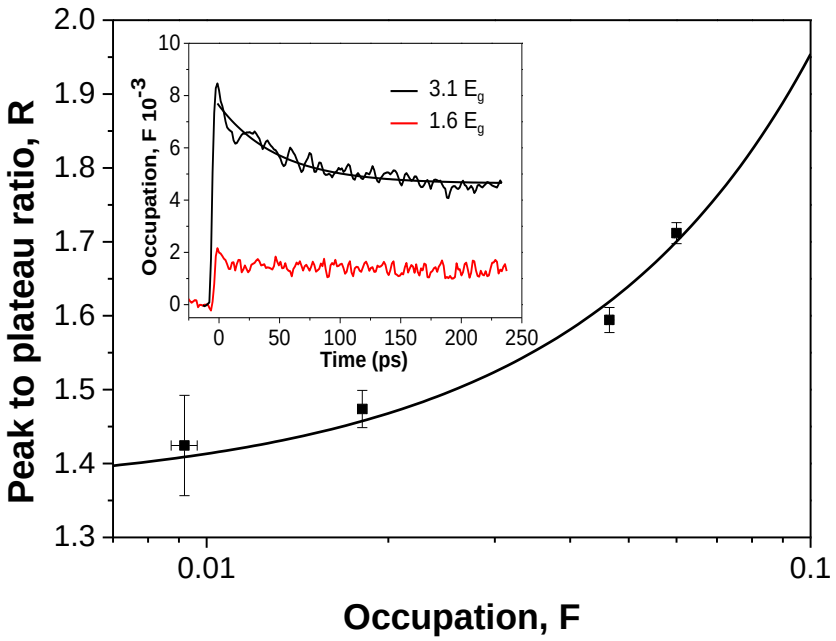

Figure 3.21 Peak-to-plateau ratio, R, of the transmittance transients induced by a pump beam of wavelength $3.1E_g$ for MPA-capped HgTe QDs as a function of the occupation of the probe state, F; the fit shown is to Equation 3.5. Inset: Comparison of the occupation transients induced by a pump power of 0.5 mW and wavelengths $1.6E_g$ and $3.1E_g$. The fit shown is to a mono-exponential decay function with a time constant of 49 ps.

After initial excitation, the below-threshold transient shows no decay in the 250 ps window, i.e., just a plateau, demonstrating that the sample is free of any trion decay or direct surface trapping which can be confused with MEG and confirms that F is sufficiently low to ensure that the probability of absorbing two photons by a single QD per pump pulse is negligible. In contrast, pumping the sample above the threshold of MEG to an occupation level of the same order resulted in a clear bi-exciton decay feature, corresponding to a value of R clearly greater than 1. Figure 3.21 also shows the variation of R with the occupation, F, for above-threshold pumping. The data fit very well to Equation 3.5, which also supports the attribution of the observed decay feature in the transient to bi-exciton recombination. The fit also allows the determination of the QY yielding a value of 1.36 ± 0.04 for excitation at $3.1E_g$, which confirms the occurrence of MEG.

Allan and Delerue [2] calculated QY as a function of pump photon energy for three different phonon cooling lifetimes: 1, 3, and 10 ps as shown in Figure 3.22; the experimentally measured QY is also shown in magenta for comparison.

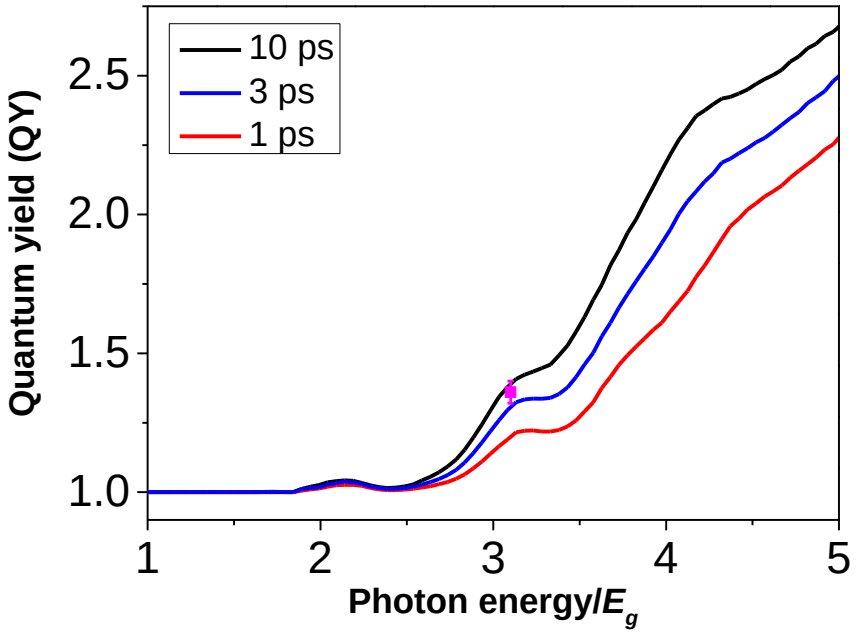

Figure 3.22 MEG quantum yield of 3.5 nm diameter HgTe QDs calculated for three different phonon cooling lifetimes. The point shown in magenta is the experimentally measured quantum yield for comparison.

It is clear that the measured QY agrees well with the one calculated, indicating that the phonon cooling lifetime of the sample under study is between 3 and 10 ps, and is consistent with the ~6 ps rise time of the transients after photoexcitation, shown in Figure 3.23, which corresponds to the cooling time of hot excitons to the band edge. Figure 3.22 also shows that MEG occurs only for photon energy, $h\nu$, greater than $2E_g$, the minimum allowed by conservation of energy, but its QY does not begin to rise notably until $h\nu$ reaches ~$2.5E_g$. It also shows an important result, indicating how the QY of MEG can vary with the rate of carrier cooling. This is important to consider when studying MEG in imperfectly passivated QDs in which surface-related cooling processes can be significant, leading to an increase in the total rate of carrier cooling, which competes with MEG and thus

to a reduction in the resultant QY, which complicates comparison with the efficiency of bulk impact ionisation [12, 28].

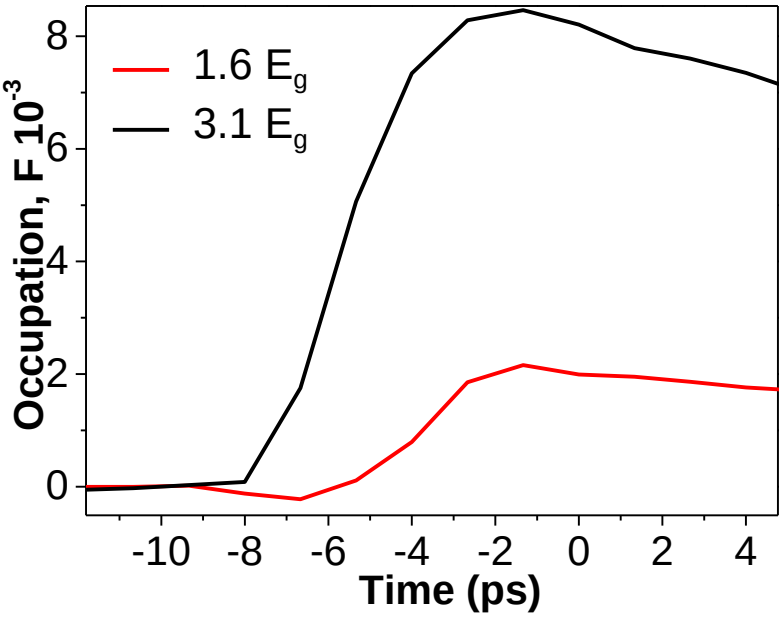

Figure 3.23 Initial bleach rise for MPA-capped HgTe QDs when pumped with photon energies above and below the MEG threshold

The performance of HgTe QDs MEG is comparable with that of most other QD types studied to date and discussed in section 2.3.2, especially QDs that take into account the influence of the trion formation and direct surface trapping processes which can be confused with MEG. For example, MPA-capped HgTe QDs demonstrate better performance than Pb-chalcogenide QDs, which have shown a QY of ~1.2 when pumped with photon energy of ~3E_g [29]. InP QDs [30] have shown an efficiency that is similar to that reported here for HgTe QDs. However, their band edge was beyond the optimum range for exploitation of the solar spectrum. A quantum yield of ~2 has been reported for closely-packed arrays of Si nanocrystals in SiO_2 when using pump photon energy greater than 2.6E_g [31]. However, the mechanism used there was different from the one used here, since an additional exciton is generated in an adjacent QD.

We have just seen the high QY that HgTe QDs exhibit at low photon energy compared to other materials. They also benefit from size-tunability over the optimum range for exploitation of the solar spectrum. One more advantage that HgTe QDs have over some other QDs is insensitivity to water and air exposure. All the samples studied here during the experimental measurements were prepared and diluted in water and open to the atmosphere, while there are some QDs that are susceptible to oxidation [32], which requires the use of anhydrous solvents and preparation under inert atmospheres. Oxidisation was found, for example, to be able to convert 50% of the outer volume of a QD into an oxide shell with a large band edge surrounding a core of unoxidised PbSe [33], which in turn leads to blue-shifting the absorption edge and eliminates extracting charges from the core of the QD. Such issues can affect the performance of solar cells and, therefore, researchers are likely to have had special requirements, such as a helium atmosphere [34], when making solar cells to ensure that the QDs are sealed from the atmosphere. This special requirement can, notably, increase the cost of solar cells based on this type of QD. However, MPA-capped HgTe QDs are chemically stable, which enables these steps to be bypassed and hence is likely to reduce the cost of solar cells based on QDs. The literature reports MPA ligands diluted with methanol used to passivate PbS CQDs for solar cell measurements [35]. The power conversion efficiency achieved was 5.1%. The QDs were prepared using a layer-by-layer method to make film deposited with PbS QDs and 5 drops of MPA were used in each layer. Such a good level of efficiency achieved by using MPA in addition to the results we obtained should turn researchers' attention to those ligands which could improve the QD solar cell field.

3.7.2 DDT-capped QDs

As mentioned earlier, DDT-capped HgTe QDs could be considered as an example of how MEG could be overestimated. Here, a measurement of the QY is assessed based on the TA results and compared to the theoretical value already expected for these QDs. The probability of a QD absorbing more than one photon per pump pulse is negligible at low pump fluences and the measurements of QY here are limited to the vigorously stirred samples throughout the experiment and to the transients with peaks that decay mono-exponentially to a plateau with a constant lifetime. The method we will use here to assess MEG is similar to one already used [13], which relies on deducing MEG from the R values obtained from the transients over a range of excitation levels (above and below the MEG threshold) but when vanishing the pump fluence. The transmittance transients can be expressed in terms of the occupation of the probed state, F, where it is $7.25\Delta T/T$ for pumping with $1.6E_g$ and $16.13\Delta T/T$ when exciting with $3.2E_g$ (see Equation 3.7). Figure 3.24 a) shows the peak-to-plateau ratio, R, of the transmittance transients induced by a pump beam of wavelength $1.6E_g$ (below the MEG threshold, which is at least twice the band edge) for DDT-capped HgTe QDs as a function of the occupation of the probe state, F. The fit shown is to Equation 3.5 and has a quantum yield value of 1.14 ± 0.17. In comparison, when pumping the sample above the MEG threshold ($3.2E_g$), as shown in Figure 3.24 b), the magnitude of R becomes significantly greater than 1. The data fit reasonably to Equation 3.5, yielding a QY value of 1.56 ± 0.11. This experimental value of the QY contradicts the theoretical value of 1.1, suggesting that direct surface trapping influences the value here, which supports our conclusion to refer the decay of the transients shown in Figure 3.17 to being due to surface-related processes.

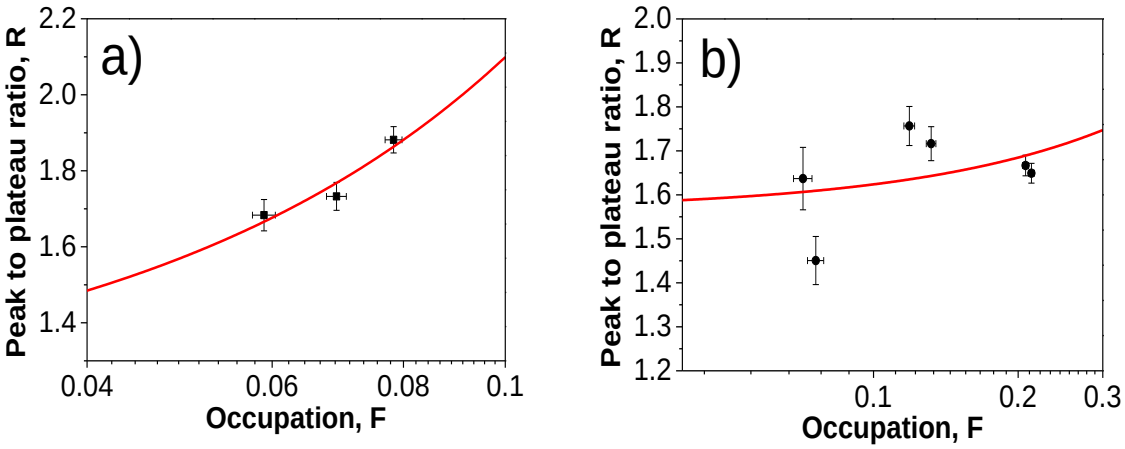

Figure 3.24 Peak-to-plateau ratio, R, of the transmittance transients for DDT-capped HgTe QDs as a function of the occupation of the probe state, F. QDs are induced by a pump beam of wavelengths a)1.6E_g and b) 3.2 E_g; the fit shown is to Equation 3.5.

3.8 Summary

UTA spectroscopy has been used here in the study of charge dynamics in HgTe QDs capped by 1-thioglycerol, MPA and DDT ligands. Under experimental conditions, the sign of PA in the spectra superimposed with a bleach was attributed to charges trapped in the QD surface characterised by a decay lifetime near 30 ps. None of the samples' transmittance transients showed any sign of trion recombination at low pump powers but this was evident at high pump powers in some samples. A discussion of the chemical structures of the ligands has suggested that the carboxylic acid group played an important role in the passivation processes, enabling greater donation of the electron density that suppresses trap states for the MPA-capped samples. In this chapter, MEG was measured for the first time in semimetal QDs with a QY of 1.36 for excitation at 3.1E_g.

3.9 References

1. Peterson, M.D., et al., *The Role of Ligands in Determining the Exciton Relaxation Dynamics in Semiconductor Quantum Dots.* Annual Review of Physical Chemistry, Vol 65, 2014. **65**: p. 317-339.
2. Al-Otaify, A., et al., *Multiple exciton generation and ultrafast exciton dynamics in HgTe colloidal quantum dots.* Physical Chemistry Chemical Physics, 2013. **15**(39): p. 16864-16873.
3. Koktysh, D., et al., *Near-infrared electroluminescence from HgTe nanocrystals.* ChemPhysChem, 2004. **5**(9): p. 4.
4. Kovalenko, M.V., et al., *Colloidal HgTe Nanocrystals with Widely Tunable Narrow Band Gap Energies: From Telecommunications to Molecular Vibrations.* Journal of the American Chemical Society, 2006. **128**(11): p. 3516-3517.
5. Lhuillier, E., S. Keuleyan, and P. Guyot-Sionnest, *Optical properties of HgTe colloidal quantum dots.* Nanotechnology, 2012. **23**(17): p. 175705.
6. Allan, G. and C. Delerue, *Tight-binding calculations of the optical properties of HgTe nanocrystals.* Physical Review B, 2012. **86**(16): p. 165437.
7. McElroy, N., et al., *Increasing Efficiency with Multiple Exciton Generation.* Quantum Dot Solar Cells, 2014. **15**: p. 233-253.
8. Liu, H., S. Keuleyan, and P. Guyot-Sionnest, *n- and p-Type HgTe Quantum Dot Films.* Journal of Physical Chemistry C, 2012. **116**(1): p. 1344-1349.
9. Cadirci, M., et al., *Ultrafast exciton dynamics in Type II ZnTe-ZnSe colloidal quantum dots.* Physical Chemistry Chemical Physics, 2012. **14**(39): p. 13638-13645.
10. Tyagi, P. and P. Kambhampati, *False multiple exciton recombination and multiple exciton generation signals in semiconductor quantum dots arise from surface charge trapping.* The Journal of Chemical Physics, 2011. **134**(9): p. 094706-10.
11. Cadirci, M., *Ultrafast charge dynamics in novel colloidal quantum dots*, in *Faculty of Engineering and Physical ScienceSchool of Physics and Astronomy*. 2014, The University of Manchester: Manchester, UK. p. 202.
12. Binks, D.J., *Multiple exciton generation in nanocrystal quantum dots - controversy, current status and future prospects.* Physical Chemistry Chemical Physics, 2011. **13**(28): p. 12693-12704.
13. Beard, M.C. and R.J. Ellingson, *Multiple exciton generation in semiconductor nanocrystals: Toward efficient solar energy conversion.* Laser & Photonics Reviews, 2008. **2**(5): p. 377-399.
14. Klimov, V.I., ed. *Semiconductor and Metal Nanocrystals*. 2004, Marcel Dekker: New York. 484.
15. Kambhampati, P., *Hot Exciton Relaxation Dynamics in Semiconductor Quantum Dots: Radiationless Transitions on the Nanoscale.* Journal of Physical Chemistry C, 2011. **115**(45): p. 22089-22109.
16. Cadirci, M., et al., *Ultrafast exciton dynamics in InAs/ZnSe nanocrystal quantum dots.* Physical Chemistry Chemical Physics, 2012. **14**(43): p. 15166-15172.
17. McGuire, J.A., et al., *New Aspects of Carrier Multiplication in Semiconductor Nanocrystals.* Accounts of Chemical Research, 2008. **41**(12): p. 1810-1819.
18. Midgett, A.G., et al., *Flowing versus Static Conditions for Measuring Multiple Exciton Generation in PbSe Quantum Dots.* The Journal of Physical Chemistry C, 2010. **114**(41): p. 17486-17500.
19. McGuire, J.A., et al., *Apparent Versus True Carrier Multiplication Yields in Semiconductor Nanocrystals.* Nano Letters, 2010. **10**(6): p. 2049-2057.
20. Kershaw, S., *HgTe QDs*. 2015.

21. Zane, A.P., *The Synthesis and Behavior of Positive and Negatively Charged Quantum Dots*. 2011, The Ohio State University.
22. Kaszuba, M., et al., *High-concentration zeta potential measurements using light-scattering techniques.* Philosophical Transactions of the Royal Society of London A: Mathematical, Physical and Engineering Sciences, 2010. **368**(1927): p. 4439-4451.
23. Zhang, W.-H., J. Yang, and J.-S. Yu, *Synthesis of stable near-infrared emitting HgTe/CdS core/shell nanocrystals using dihydrolipoic acid as stabilizer*. Journal of Materials Chemistry, 2012. **22**(13): p. 6383-6388.
24. Mundra, P., et al., *Automated setup for spray assisted layer-by-layer deposition.* Review of Scientific Instruments, 2013. **84**(7): p. 074101.
25. He, R., et al., *Synthesis of CdTe colloidal quantum dots (QDs) in water*. Frontiers of Chemistry in China, 2008. **3**(3): p. 325-329.
26. Rogach, A.L., et al., *Aqueous Synthesis of Thiol-Capped CdTe Nanocrystals: State-of-the-Art.* The Journal of Physical Chemistry C, 2007. **111**(40): p. 14628-14637.
27. Ben-Lulu, M., et al., *On the Absence of Detectable Carrier Multiplication in a Transient Absorption Study of InAs/CdSe/ZnSe Core/Shell1/Shell2 Quantum Dots.* Nano Letters, 2008. **8**(4): p. 1207-1211.
28. Padilha, L.A., et al., *Carrier Multiplication in Semiconductor Nanocrystals: Influence of Size, Shape, and Composition.* Accounts of Chemical Research, 2013. **46**(6): p. 1261-1269.
29. Stewart, J.T., et al., *Comparison of Carrier Multiplication Yields in PbS and PbSe Nanocrystals: The Role of Competing Energy-Loss Processes.* Nano Letters, 2011. **12**(2): p. 622-628.
30. Stubbs, S.K., et al., *Efficient carrier multiplication in InP nanoparticles.* Physical Review B, 2010. **81**(8): p. 081303.
31. Trinh, M.T., et al., *Direct generation of multiple excitons in adjacent silicon nanocrystals revealed by induced absorption.* Nat Photon, 2012. **6**(5): p. 316-321.
32. Hardman, S.J.O., et al., *Electronic and surface properties of PbS nanoparticles exhibiting efficient multiple exciton generation.* Physical Chemistry Chemical Physics, 2011. **13**(45): p. 20275-20283.
33. Sykora, M., et al., *Effect of Air Exposure on Surface Properties, Electronic Structure, and Carrier Relaxation in PbSe Nanocrystals.* Acs Nano, 2010. **4**(4): p. 2021-2034.
34. Semonin, O.E., et al., *Peak External Photocurrent Quantum Efficiency Exceeding 100% via MEG in a Quantum Dot Solar Cell.* Science, 2011. **334**(6062): p. 1530-1533.
35. Pattantyus-Abraham, A.G., et al., *Depleted-Heterojunction Colloidal Quantum Dot Solar Cells.* ACS Nano, 2010. **4**(6): p. 3374-3380.

Chapter 4 Ultrafast exciton dynamics in CdHgTe alloy QDs

4.1 Introduction

Ultrafast exciton dynamics in cadmium mercury telluride ($Cd_xHg_{(1-x)}Te$) alloy QDs are investigated in this chapter. Firstly, the fundamental optical properties are studied, including steady state absorption, photoluminescence, and pump-induced transmittance change spectra. Then the excitonic dynamics of the sample are investigated in detail, including the transmittance transients above and below the expected MEG threshold, and the shape of the transients obtained for stirred and static samples. All of the possible mechanisms that can be involved in sub-nanosecond transients are discussed. Finally, a MEG quantum yield is determined and compared to a study recently published.

4.2 Samples under study

The $Cd_xHg_{(1-x)}Te$ alloy QDs used here were synthesised by Dr. S. V. Kershaw, our collaborator in The Centre for Functional Photonics, Department of Physics and Material Science at City University of Hong Kong. The synthesis process is described in Ref. [1], but here we provide a brief description. CdTe QDs were firstly synthesised and their solution precipitated, and then the QDs were dispersed in deionised water. When getting to this stage, different amounts of Hg^{2+} solution were added. Samples were made by what is known as ion exchange in water, which then can be transferred into organic solution to ensure that the QDs are properly dispersed as individual QDs.

4.3 Characterisation

Figure 4.1 shows the absorption and PL spectra for a typical sample of $Cd_xHg_{(1-x)}Te$ alloy QDs. It can be seen that the PL spectrum has a peak at ~1043 nm and an FWHM of

about 150 nm (narrower than the PL for HgTe QDs shown in the previous chapter), while the absorption spectrum shows a broad shoulder Stokes-shifted from the PL peak by 100–150 nm to shorter wavelengths and centred at about 920 nm. Narrow PL FWHM is said to be achieved in alloy QDs as the broadening of the PL is usually because of the fluctuation of the QDs' size, which is highly decreased in alloyed QDs [2]. The FWHM of the PL spectrum for $Cd_xHg_{(1-x)}Te$ alloy QDs shown in Figure 4.1 supports such a theory.

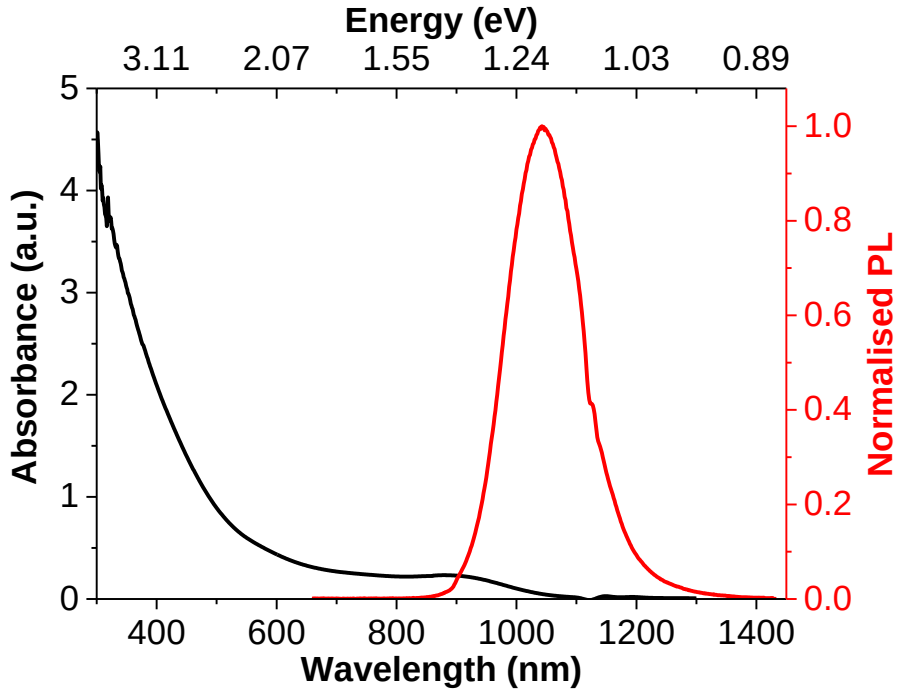

Figure 4.1 Absorbance (black) and PL (red) spectra of $Cd_xHg_{(1-x)}Te$ alloy QDs.

Our strategy is then to examine the sample's differential spectrum to gain information regarding bleach and PA, if there is any, behaviour. Figure 4.2 shows the pump-induced transmittance change, $\Delta T/T$, spectrum obtained for a sample of $Cd_xHg_{(1-x)}Te$ alloy QDs taken at the time when it was at its maximum amplitude. As expected, the spectrum shows a feature at ~920 nm, which is referred to as a bleach located in the same position of the shoulder seen in the steady state absorption spectrum in Figure 4.1, i.e. the 1S position, but this shoulder is followed by a peak at ~1050, which is attributed to the sample's PL. Note that PL contributes to the measured spectrum because it produces additional pump-induced

photons at the detector. However, it can be distinguished from pump-induced changes in the absorption because it is independent of the pump-probe delay and, thus, appears as a constant background in kinetic traces (see inset in Figure 4.2).

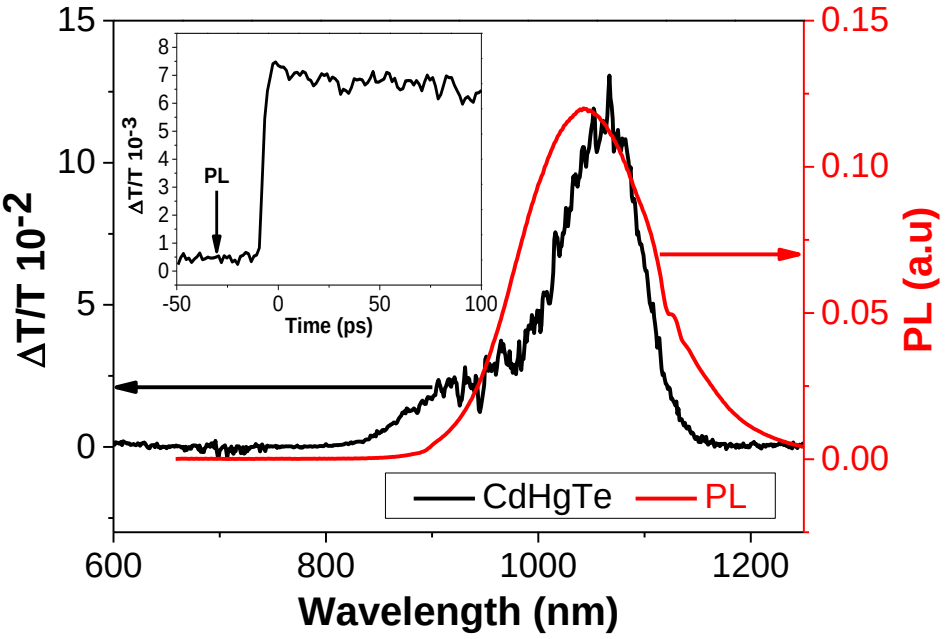

Figure 4.2 Pump-induced transmittance change, ΔT/T, spectrum taken with 500 nm pump wavelength of $Cd_xHg_{(1-x)}Te$ alloy QDs (black). PL (red) is shown in an arbitrary units for comparison. Inset: an example of a transient showing the PL as a background.

4.4 Excitonic dynamics of $Cd_xHg_{(1-x)}Te$ alloy QDs

The QDs' exciton dynamics, including MEG, were studied by measuring the transmittance transients of the bleach. Different excitation wavelengths were used, below the expected MEG threshold for the QDs used and above it. Figure 4.3 shows the measured transmittance transients of the bleach of the $Cd_xHg_{(1-x)}Te$ alloy QDs when probing at 920 nm and pumping with 400 nm (above the MEG threshold of ~2.6 E_g) using average pump powers of 0.175, 0.235, 0.300 and 0.450 mW. A global fit to the transients from the peak to the plateau, using Equation 3.2 to a mono-exponential decline, yielded a time constant of 91±1 ps. Note that the fit for the highest pump power used is not as good as the others at the first couple of ps of the decay, i.e. it starts to deviate from being mono-exponential,

suggesting that trion formation begins to appear, which limits our measurements to this value and lower. Similar behaviour was seen for HgTe QDs, as described in the last chapter.

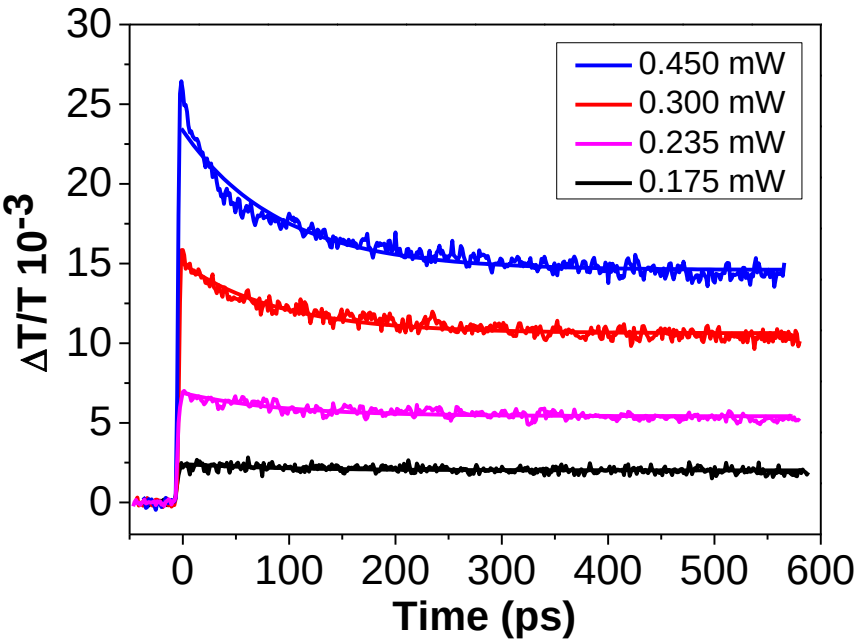

Figure 4.3 Transmittance transients obtained for the $Cd_xHg_{(1-x)}Te$ alloy QDs at a probe wavelength of 920 nm. The transients were induced by 400 nm of the powers shown in the legends. The fits shown are global and for a mono-exponential decay with a time constant of 91±1 ps.

A single wavelength is not enough to study exciton dynamics such as MEG; therefore, the bleach transmittance transients of the $Cd_xHg_{(1-x)}Te$ alloy QDs were also taken when probing at the same probe wavelength, 920 nm, but induced by a 750 nm wavelength of 0.26, 0.32, 0.40 and 1.00 mW. This wavelength is, based on Equation 1.5, below the MEG threshold at ~1.4 E_g. Figure 4.4 shows the resultant transients in a 550 ps window. A global fit to the transients well describes the peak-to-plateau decay with a mono-exponential decay with the same time constant as for Figure 4.3, i.e. 91 ps.

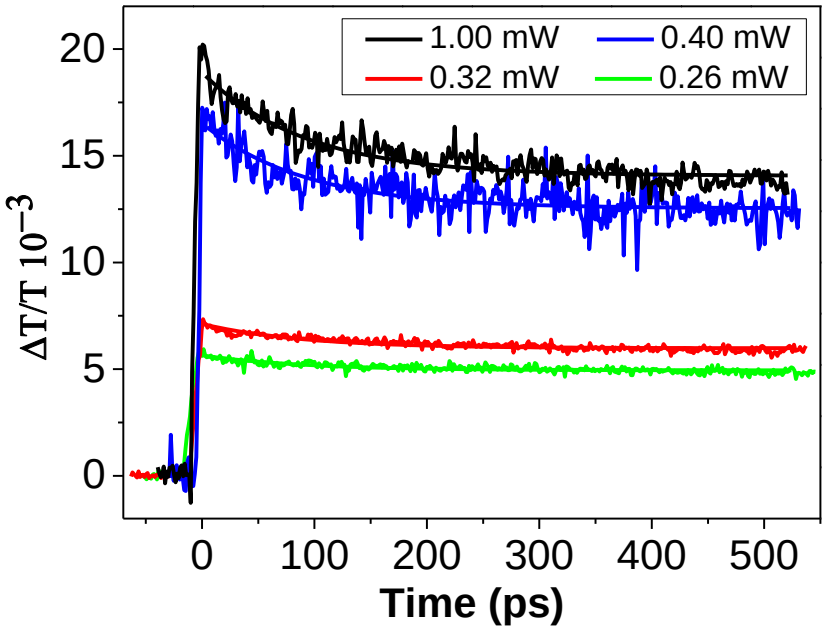

Figure 4.4 Transmittance transients obtained for the $Cd_xHg_{(1-x)}Te$ alloy QDs at a probe wavelength of 920 nm when pumped with 750 nm of the powers shown in the legends. The fits to the data shown resulted in a decay lifetime of 91 ps.

Bleach transients were measured at two more wavelengths: 470 nm (~2.2 E_g) and 370 nm (~2.8 E_g). The expected MEG threshold of the $Cd_xHg_{(1-x)}Te$ alloy QDs can be calculated from Equation 1.5. The effective masses of the electron and hole are 0.064 m_0 and 0.35 m_0, respectively, where m_0 is the electron mass [3] and, thus, the expected MEG threshold is ~2.18 E_g. It means that the 470 nm wavelength is almost located at the threshold for MEG, while the 370 nm wavelength is above it. Figure 4.5 shows in a 600 ps window the transients of the $Cd_xHg_{(1-x)}Te$ alloy QDs when probing and pumping with 920 nm and 470 nm, respectively. The average pump powers used were 0.25, 0.40 and 0.60 mW. The fit shown is for a mono-exponential decay with a time constant of 91 ps. The deviation from being mono-exponential which was seen in the highest pump power fit is a sign of the limitation in the pump power used, as in this power the trion formation starts to add an extra component to the transients.

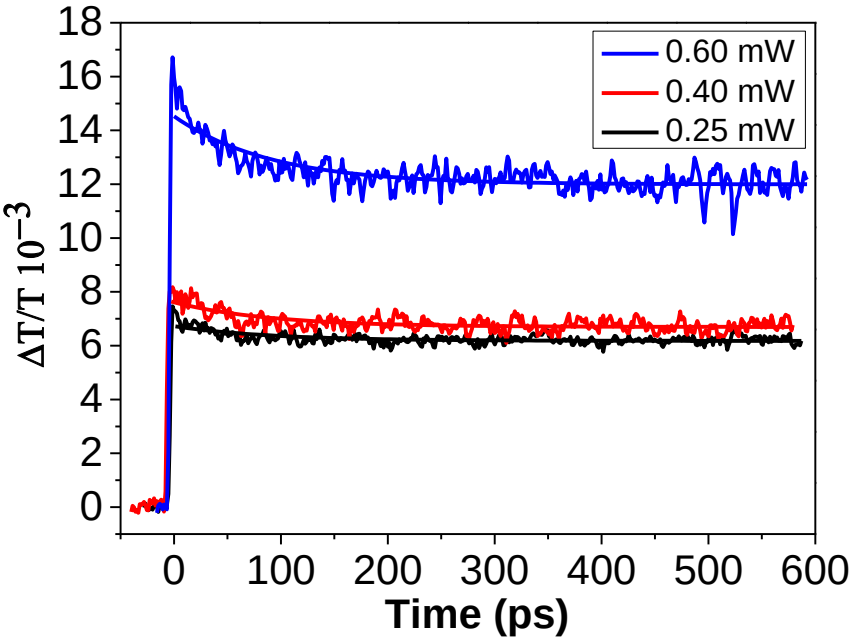

Figure 4.5 Fractional transmittance change, ΔT/T, transients for $Cd_xHg_{(1-x)}Te$ alloy QDs induced by a pump beam of a 470 nm wavelength with a range of average powers shown in the legends. A global mono-exponential fit to the decays is also shown yielding a time constant of 91 ps.

Similarly, Figure 4.6 shows the transmittance transients for $Cd_xHg_{(1-x)}Te$ alloy QDs induced by a pump wavelength of 370 nm, with average pump powers ranging from 0.15 mW to 0.60 mW. Also shown is the global fit to a mono-exponential decay using Equation 3.2 with a time constant of 91 ps. The measurements were taken on different days on which the overlap between the pump and probe beams is not necessarily exactly the same. The overlap between the two beams is part of the daily experimental preparations before taking the measurements; thus, it could differ. Therefore, not all of the measured power of the pump spot might be used to overlap with the probe spot, which then can affect the pump power trend as shown in Figure 4.6. However, the transients in our measurements can be obtained even if the overlap of the pump is not perfectly achieved in the centre of the probe beam. Furthermore, we do not study the maximum of the transient against the pump powers or even the overlap between pump and probe beams; rather, we study the decay of the maximum value of the transients. The deviation from the mono-exponential fit is also seen in

Figure 4.6, and it is that trion formation beginning to appear at that pump power which limits our measurements, which is the same reason discussed earlier in Figure 4.3 and Figure 4.5.

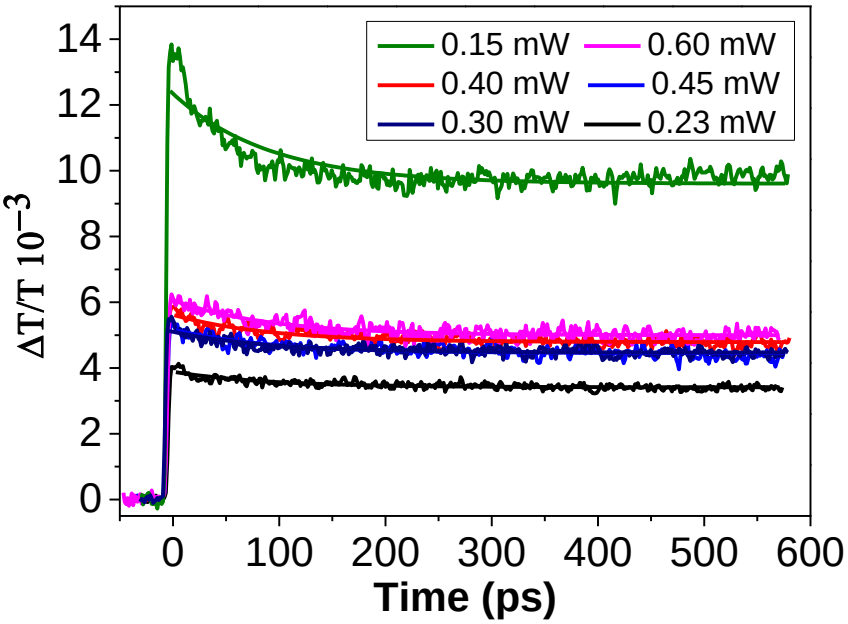

Figure 4.6 Fractional transmittance change, ΔT/T, transients obtained for $Cd_xHg_{(1-x)}Te$ alloy QDs induced by 370 nm with a range of average powers shown in the legends. A global mono-exponential fit to the decays is also shown yielding a time constant of 91 ps.

4.4.1 Stirring effect on $Cd_xHg_{(1-x)}Te$ alloy QDs

We have just seen how transients at low pump powers are described by a mono-exponential decay, but the stirring effect on the sample has not been shown yet. This gives an idea about photocharging of the $Cd_xHg_{(1-x)}Te$ alloy QDs. The literature has shown no study of this effect, although determining the degree of trion formation is very important in ensuring MEG yield is assessed reliably. Figure 4.7 compares pump-induced transmittance transients for a 0.235 mW pump power at a wavelength of 400 nm obtained for static and stirred samples of $Cd_xHg_{(1-x)}Te$ alloy QDs. The power used here is in the low pump power range and no difference can be seen between the transients for a static and stirred sample, indicating that trion formation is eliminated in these alloy QDs, which will result in a reliable MEG assessment.

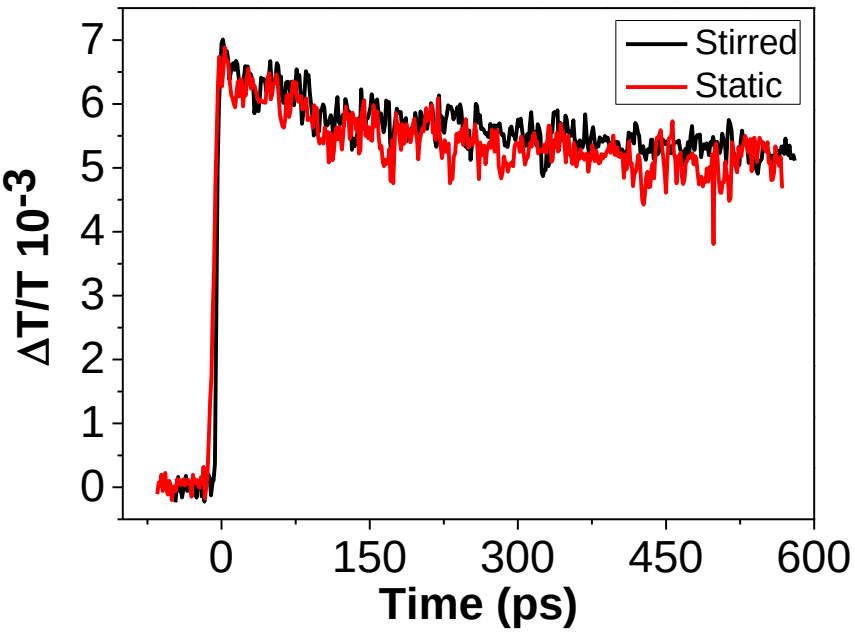

Figure 4.7 Comparison of pump-induced transmittance transients for the same pump power, 0.235 mW, at a wavelength of 400 nm obtained for static and stirred samples of $Cd_xHg_{(1-x)}Te$ alloy QDs.

4.5 Discussion of the possible mechanisms

Transients shown in Figure 4.3 have a lifetime of 91 ps, which could be due to multi-exciton recombination either by MEG or by the absorption of multi-photons upon the excitation process. However, it has been already discussed that there are two other processes which can lead to a sub-nanosecond decay similar to that shown in Figure 4.3 with a similar time-scale: trion decay and direct surface trapping, which were studied in different types of QDs [4-9]. However, it is well known that trion formation can be eliminated by a vigorous stirring or flowing of the sample [8-10]. All of the samples used for the study were stirred at 1000 rpm using a magnetic stirrer to supress any trion formation. Moreover, Figure 4.7 has shown that at low pump powers the transients obtained for stirred and static samples were almost the same (no significant difference between them is evident) and they possess the same mono-exponential decay, meaning that trion decay was not the cause of the transients obtained above the MEG threshold, i.e. the ones shown in Figure 4.3 and Figure 4.6. Direct surface trapping is the other possible mechanism that can lead to transients similar to the

ones shown above. However, it is always characterised by PA near to the band edge [5-7]. The pump-induced transmittance change spectrum of $Cd_xHg_{(1-x)}Te$ alloy QDs measured in this study (see Figure 4.2) has shown no sign of any PA in the sample, indicating that direct surface trapping is also not the reason behind the transients obtained in Figure 4.3 and Figure 4.6. Therefore, we conclude that the bleach decay of the $Cd_xHg_{(1-x)}Te$ alloy QDs is dominated by bi-exciton recombination. As the transients below the MEG threshold show significant decays (see Figure 4.4), we attribute them to bi-exciton recombination created by two photons, while in the above MEG threshold case the decay of the transients is attributed to bi-exciton recombination due to both the absorption of two photons and MEG.

4.5.1 MEG

Energy conservation is applied in the formation of MEG, which means that a photon energy equivalent to at least twice the band edge ($2E_g$), according to Equation 1.5, is required to create any extra exciton, with each additional exciton on top of that requiring further energy at least equal to the band edge. Based on this limit, any photon with energy between $2E_g$ and $3E_g$ is capable of producing just a bi-exciton, which then decays into a single exciton on a sub-nanosecond time-scale (10s of ps). For vanishing pump fluences, and thus $\langle N \rangle$ in Equation 3.5, the value of R becomes equivalent to the QY, which is greater than 1 if MEG occurs. We stated earlier that the transients obtained for $Cd_xHg_{(1-x)}Te$ alloy QDs are free of any PA and trion formation at sufficiently low pump fluences. Therefore, MEG in this sample can be identified and its resulting quantum yield can be assessed.

MEG in the literature has been identified either by comparing transients obtained at similar levels of average excitation, i.e. $\langle N \rangle$, and pumped at photon energies above and below the MEG threshold [11] or by extracting the MEG quantum yield from R values obtained from the transients over a range of excitation levels for both above and below the MEG

threshold, and extrapolating to the vanishing pump fluence [12]; the latter method is used here. Equation 3.7 explained the dependence of $\Delta T/T$ on arbitrary values of A, and allows us to express the transients in terms of the occupation of the probed state. We managed to study the variation of the peak-to-plateau ratio, R, with the occupation, F, for both above and below MEG threshold pumping. Figure 4.8 shows R as a function of F for the transmittance transients obtained for $Cd_xHg_{(1-x)}Te$ alloy QDs when induced by a pump beam of wavelengths: a) $1.4E_g$ (below the MEG threshold) and b) $2.2E_g$ (almost at the MEG threshold). F is $3.3\Delta T/T$ in the case of $1.4E_g$ (as the optical density at the probe wavelength was 0.4, while it was 0.44 at the pump wavelength). In contrast, F is $6.1\Delta T/T$ when exciting with $2.2E_g$ (where the optical density at the pump wavelength was 2.16) (see Equation 3.7). The PL lifetime of the alloyed QDs used here was measured as being ~55 ns [13] extracted from a stretched exponential fit to the PL decay with a β factor of 0.79; thus, any single-exciton decay should be considered when investigating a MEG quantum yield.

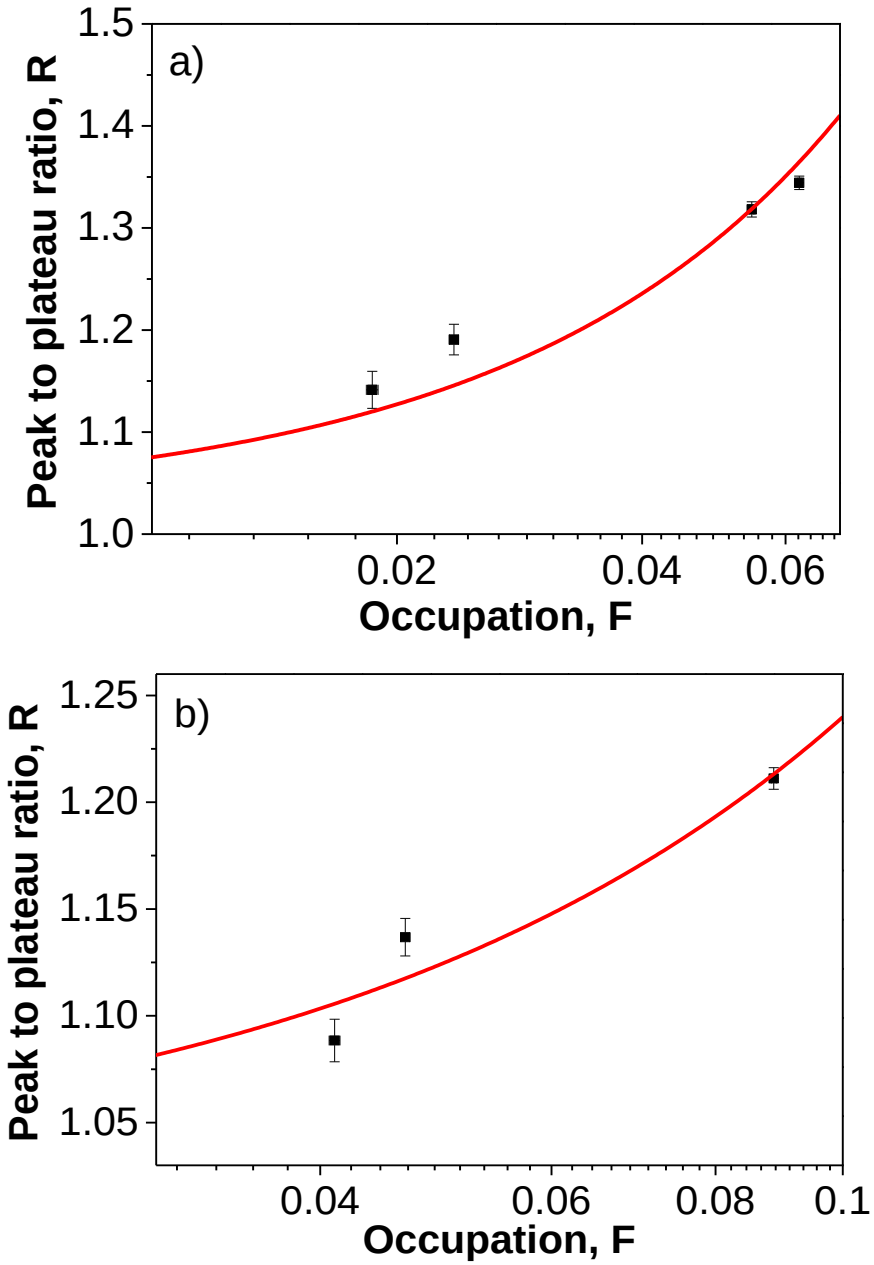

Figure 4.8 Peak-to-plateau ratio, R, of the transmittance transients induced by a pump beam of wavelengths a) 1.4E_g and b) 2.2E_g for $Cd_xHg_{(1-x)}Te$ alloy QDs as a function of the occupation of the probe state, F; the fit shown is to Equation 4.1.

Beard *et al.* [12] have defined the peak-to-plateau ratio in the presence of any single-exciton decay as:

$$R = \frac{\delta . \langle N \rangle . QY}{1 - exp(-\langle N \rangle)}$$

Equation 4.1

where QY is the quantum yield, $\langle N \rangle$ is the average number of absorbed photons per pulse per QD, and δ is a factor that takes into account the single-exciton decay during the experiment. It is given by:

$$\delta = exp\left(\frac{t_{plateau} - t_{peak}}{\tau_{PL}}\right)^{\beta}$$

Equation 4.2

where $(t_{plateau} - t_{peak})$ is the time by which the decay is completed and assumed to be 0.5 ns in this study, and both the PL lifetime, τ_{PL}, and β are parameters resulting from the stretched exponential fit to the PL decay, which gives δ a value of ~1.025; this value is used from now on and applied for quantum yield measurements in all of the cases above and below the MEG threshold. Therefore, the fit shown in Figure 4.8 is to Equation 4.1 and yields a QY of 1.01±0.01 for the a) case and 0.99±0.04 for the b) case. The two cases logically follow the nature of MEG, as the quantum yield is expected to be 1 below the threshold and then starts to increase gradually. This allows one not to expect any significant increase in the quantum yield at the MEG threshold.

In comparison, when photo-exciting the $Cd_xHg_{(1-x)}Te$ alloy QDs with photon energy above the MEG threshold, i.e. $2.6E_g$ and $2.8E_g$ (as shown in Figure 4.9 a) and b), respectively), the magnitude of R becomes significantly greater than 1. The data fit very well to Equation 4.1, which results in a QY value of 1.12±0.01 and 1.05±0.02 for $2.6E_g$ and $2.8E_g$, respectively. The peak-to-plateau ratio, R, of the transmittance transients in Figure 4.9 is plotted against the occupation of the probe state, F, which is $9.71\Delta T/T$ in the $2.6E_g$ case (as the optical density at the pump wavelength was 3.8). In comparison, it is $11.9\Delta T/T$ when exciting with $2.8E_g$ (where the optical density at the pump wavelength was 4.72).

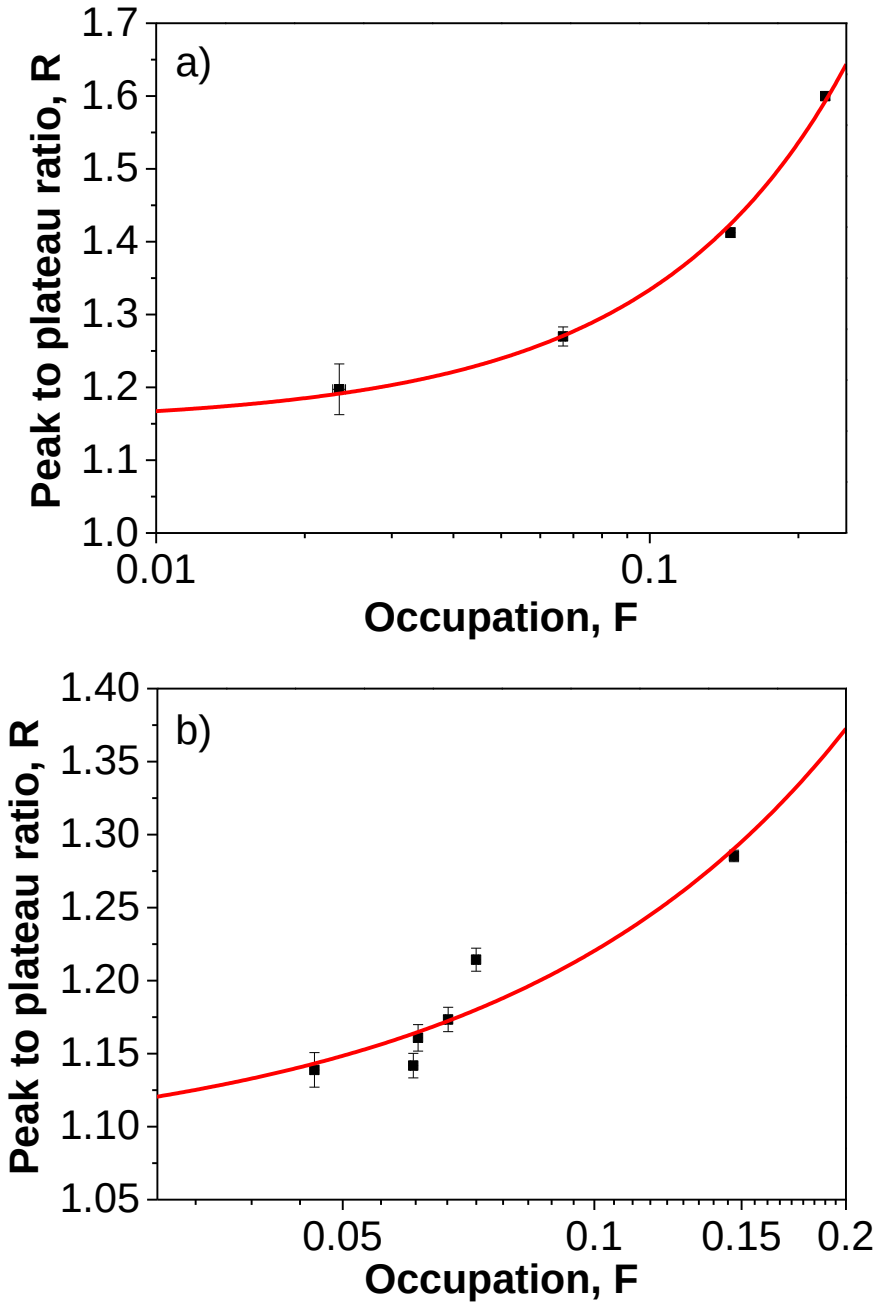

Figure 4.9 Peak-to-plateau ratio, R, of the transmittance transients induced by a pump beam of wavelengths a) 2.6E_g and b) 2.8E_g for $Cd_xHg_{(1-x)}Te$ alloy QDs as a function of the occupation of the probe state, F; the fit shown is to Equation 4.1.

The drop in the QY value when photo-exciting with 2.8E_g could be due to a similar behaviour to that reported previously for HgTe QDs [14], and was discussed in Chapter 3. The QY there starts at the threshold, and then it drops off (before it rises again). The QY experimental results also support the attribution of the transients obtained in both Figure 4.3 and Figure 4.6 to be due to bi-exciton recombination and to confirm the occurrence of MEG.

All of the transients shown above were obtained when the delay stage was set to 0.2 mm, which corresponds to a time-resolution of about 1.33 ps. Clearly, this is not sufficient to accurately study the early stage rise time of the transients, typically less than 6 ps; thus, for more accuracy a higher resolution is required. Figure 4.10 shows the initial rise time of the $Cd_xHg_{(1-x)}Te$ alloy QD's bleach, which corresponds to the cooling time of hot excitons to the band edge at three different excitation levels: $1.4E_g$, $2.6E_g$ and $2.8E_g$. The resolution used here was 10 times higher than that used for previous figures. The rise times are significantly longer for excitation at $2.6E_g$ and $2.8E_g$ at ~4 ps and ~5 ps, respectively, in comparison to ~1.1 ps for pumping at $1.4E_g$. This is attributed to the significantly greater amount of excess energy to be dissipated by cooling in the former two cases, i.e. $1.6E_g$ and $1.8E_g$, compared to $0.4E_g$.

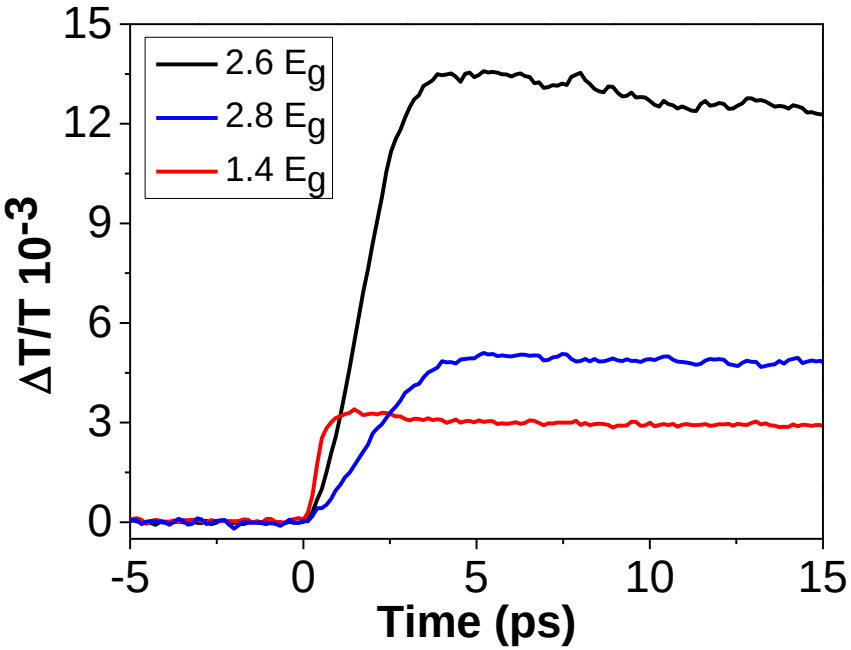

Figure 4.10 Initial bleach rise for $Cd_xHg_{(1-x)}Te$ alloy QDs when pumped with photon energies above and below the MEG threshold (shown in legend).

Our investigations have shown that the quantum yield has the highest value of 1.12±0.01 when photo-excited with $2.6E_g$. After completing MEG measurements for this study, and during the preparation of the work for submission to a journal, a study regarding

MEG in $Cd_xHg_{(1-x)}Te$ alloy QDs was published. The study reported a quantum yield of 199±19% when using pump energy of 4.28 eV (290 nm), which is equivalent to three times the band gap for $Cd_xHg_{(1-x)}Te$ alloy QDs (as shown in Figure 4.11) [15] with a MEG threshold of 2.15 times the band gap. Here, we compare MEG QY in both studies and then we highlight the novelty of our work.

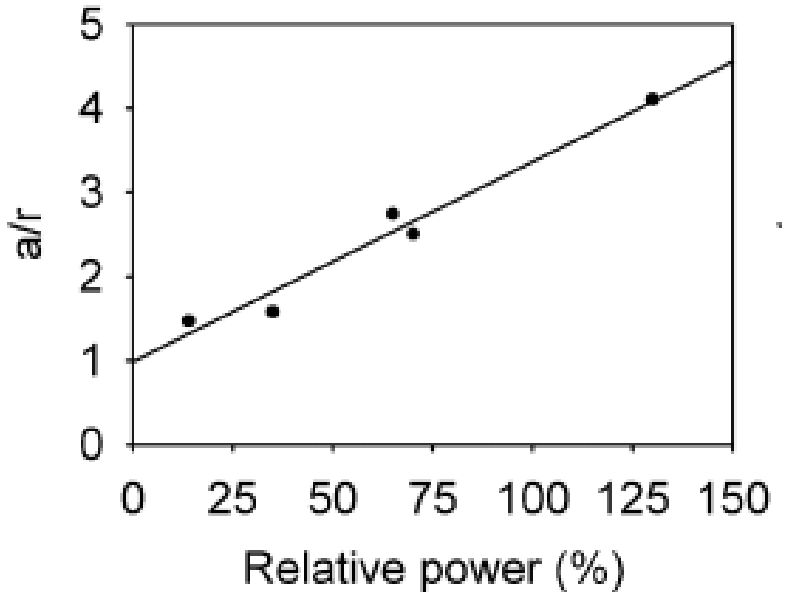

Figure 4.11 Peak-to-plateau ratio against relative power for $Cd_xHg_{(1-x)}Te$ alloy QDs. The MEG quantum yield here is 100(1+a/r)%. "Reproduced from [15] with permission of the PCCP Owner Societies."

The analysis method used in Ref. [15] considered the 1S transition as a measure of the band gap rather than the PL peak, as we do. If a comparison is made between the two results, the strategy utilised for the measurement of the photon energy used for excitation with respect to the band gap should be the same. Therefore, here we explain their measurement first and then make a comparison. The PL maximum for the sample used in Ref. [15] was 1001 nm (1.24 eV), and the photon energy used for pumping was 4.28 eV, which means that the pump photon has an energy equivalent to ~3.5E_g. Now the quantum yield of 199±19% obtained for photons with energy of 3.5E_g can be compared to our result, i.e. a quantum yield of 112±1% when pumping with 2.6E_g. Therefore, the quantum yield obtained in Ref. [15] is

almost 1.8 times the one we have measured but with more energetic photons. The calculated quantum yield for HgTe QDs in Chapter 3 as a function of pump photon energy for three different phonon cooling lifetimes can explain the dramatic increase in the quantum yield when photo-exciting with $3.5E_g$ (compared to $2.6E_g$) (see Figure 4.12, reproduced here from Chapter 3 for convenience). Clearly, photons with energy of 3.5 eV can increase the quantum yield by a factor of ~1.7 (compared to 2.6 eV) (note that the band gap used for the HgTe QDs was 1 eV). If the MEG QY for CdHgTe QDs behaves similarly, then both sets of results are consistent.

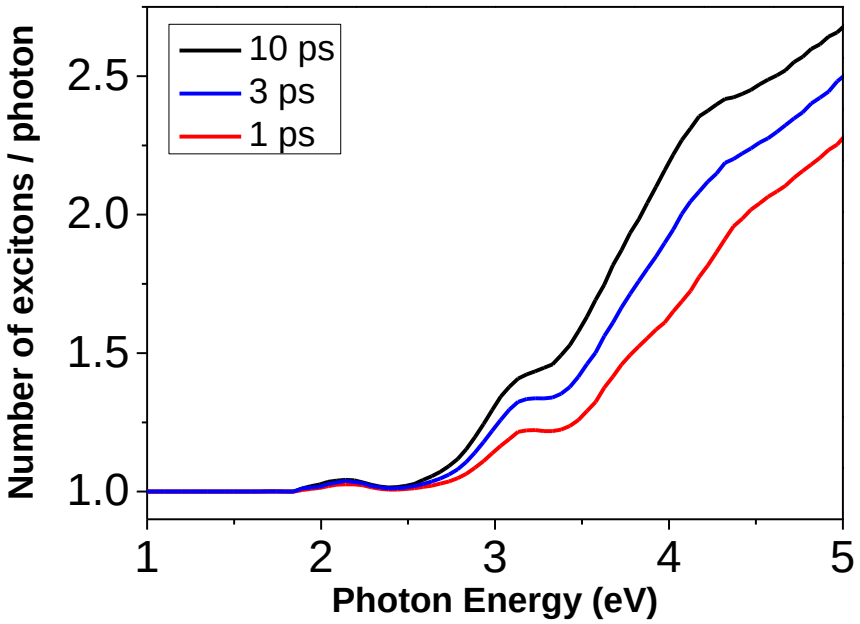

Figure 4.12 MEG quantum yield of 3.5 nm (diameter) HgTe QDs calculated for three different phonon cooling lifetimes.

Three main points highlight the novelty of our study. Firstly, the accuracy as the error in QY measurements here is 1%, while it is 19% in Ref. [15]. The more accurate result could come from the instrument used or the amount of averaging in transients' measurements. Secondly, the stirring effect on the sample was studied here as being represented by the comparison between transients for stirred and static samples, which the reported study did not cover. It is known how important such aspects of study are to determine whether stirring

could eliminate the possibility of photo-charging. Finally, this study was also able to identify the rate of carrier cooling from the transient rise times while the reported study did not.

4.6 Summary

We have used ultrafast transient absorption spectroscopy to investigate the exciton dynamics in $Cd_xHg_{(1-x)}Te$ alloy QDs. The pump-induced transmittance change spectrum has shown bleach at the band gap. Four different wavelengths have been used to study the decay of the transmittance transients; two of them are above the MEG threshold. We have found that the sample is free of photo-induced absorption and photo-charging. Therefore, we attributed the decay of the transients obtained above the MEG threshold for well-stirred samples at low pump powers to biexciton recombination. MEG has been assessed and its quantum yield was measured as being 1.12±0.01 when photo-excited with 2.6 times the band gap.

4.7 References

1. Gupta, S., et al., *$Cd_xHg_{(1-x)}Te$ Alloy Colloidal Quantum Dots: Tuning Optical Properties From the Visible to Near-Infrared by Ion Exchange.* Particle & Particle Systems Characterization, 2013. **30**: p. 346-354.
2. Bera, D., et al., *Quantum Dots and Their Multimodal Applications: A Review.* Materials, 2010. **3**(4): p. 2260-2345.
3. Bouazzi, A., Y. Marfaing, and J. Mimilaarroyo, *Optimization of Graded Band-Gap CdHgTe Solar-Cells.* Revue De Physique Appliquee, 1978. **13**(3): p. 145-154.
4. Kambhampati, P., *Hot Exciton Relaxation Dynamics in Semiconductor Quantum Dots: Radiationless Transitions on the Nanoscale.* Journal of Physical Chemistry C, 2011. **115**(45): p. 22089-22109.
5. Tyagi, P. and P. Kambhampati, *False multiple exciton recombination and multiple exciton generation signals in semiconductor quantum dots arise from surface charge trapping.* The Journal of Chemical Physics, 2011. **134**(9): p. 094706-10.
6. Cadirci, M., et al., *Ultrafast exciton dynamics in InAs/ZnSe nanocrystal quantum dots.* Physical Chemistry Chemical Physics, 2012. **14**(43): p. 15166-15172.
7. Cadirci, M., et al., *Ultrafast exciton dynamics in Type II ZnTe-ZnSe colloidal quantum dots.* Physical Chemistry Chemical Physics, 2012. **14**(39): p. 13638-13645.
8. McGuire, J.A., et al., *New Aspects of Carrier Multiplication in Semiconductor Nanocrystals.* Accounts of Chemical Research, 2008. **41**(12): p. 1810-1819.
9. Midgett, A.G., et al., *Flowing versus Static Conditions for Measuring Multiple Exciton Generation in PbSe Quantum Dots.* The Journal of Physical Chemistry C, 2010. **114**(41): p. 17486-17500.
10. McGuire, J.A., et al., *Apparent Versus True Carrier Multiplication Yields in Semiconductor Nanocrystals.* Nano Letters, 2010. **10**(6): p. 2049-2057.
11. Ben-Lulu, M., et al., *On the Absence of Detectable Carrier Multiplication in a Transient Absorption Study of InAs/CdSe/ZnSe Core/Shell1/Shell2 Quantum Dots.* Nano Letters, 2008. **8**(4): p. 1207-1211.
12. Beard, M.C. and R.J. Ellingson, *Multiple exciton generation in semiconductor nanocrystals: Toward efficient solar energy conversion.* Laser & Photonics Reviews, 2008. **2**(5): p. 377-399.
13. Kershaw, S., *Lifetimes*. 2014.
14. Al-Otaify, A., et al., *Multiple exciton generation and ultrafast exciton dynamics in HgTe colloidal quantum dots.* Physical Chemistry Chemical Physics, 2013. **15**(39): p. 16864-16873.
15. Kershaw, S.V., et al., *Multiple exciton generation in cluster-free alloy CdxHg1-xTe colloidal quantum dots synthesized in water.* Physical Chemistry Chemical Physics, 2014. **16**(47): p. 25710-25722.

Chapter 5 Size-dependence of ultrafast charge dynamics in TiO_2-Au system

5.1 Introduction

This chapter studies the ultrafast charge dynamics in different sizes of monodisperse Au nanoparticles supported on colloidal TiO_2 spheres. First, brief information about the samples under study is provided including the synthesis method used, the sizes of the nanoparticles and some images for them. Then, samples are characterised in terms of their steady state absorption (including bare Au nanoparticles), PL and pump-induced transmittance change spectra. Following that, the charge dynamics are investigated using ultrafast transient absorption spectroscopy. In particular, the effect of the NP size on the charge dynamics in this system is studied.

5.2 Samples under study

The results of this study were published in the journal *Physical Chemistry Chemical Physics* [1]. The samples studied here are colloidal TiO_2 spheres decorated with monodisperse Au nanoparticles of three different sizes. They have been synthesised by Dr. Pedro H. C. Camargo, our collaborator in the Departamento de Quı´mica Fundamental, Instituto de Quı´mica, Universidade de Sa˜o Paulo in Brazil. The synthesis process is described elsewhere [1, 2] but here we provide brief information regarding the sizes and the denotations. TiO_2 colloidal spheres with a diameter of ~220 nm were synthesised then used as templates for deposition of the Au nanoparticles. In the first stage, sample 'TiO_2-Au1' was formed after three hours of adding 3 mL of 1 mM of $AuCl_4^-$ solution to the TiO_2. In the second stage, the same amount of the solution was added to TiO_2-Au1 to form 'TiO_2-Au2' and finally in the third stage, 'TiO_2-Au3' was formed from TiO_2-Au2 in the same way. The

average diameters of the Au nanoparticles over the surface of the TiO_2 colloidal sphere were found (by our collaborators) to be 12.2±2.2 nm, 19.3±2.3 nm and 24.5±2.8 nm for samples TiO_2-Au1, TiO_2-Au2 and TiO_2-Au3, respectively. Washing the samples several times with water was part of the synthesis process during all the different stages, and they can be diluted in water. Figure 5.1 shows the steps of the synthesis and SEM images of the TiO_2-Au1, TiO_2-Au2 and TiO_2-Au3 samples. The Au nanoparticles display monodisperse sizes and uniform distribution over the TiO_2 surface. This well-controlled size enables a reliable study of the ultrafast charge dynamics in TiO_2-Au NPs as a function of NP diameter, clarifying the conflicting results currently reported in the literature, as discussed in Chapter 1.

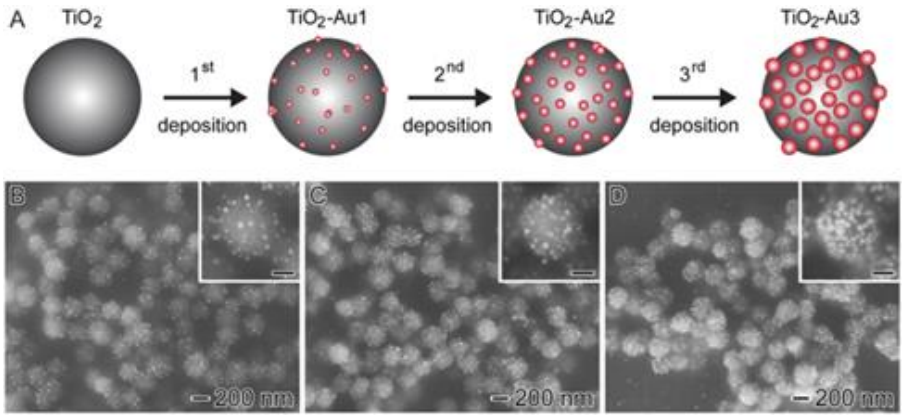

Figure 5.1 (A) Synthesis steps of TiO_2 colloidal spheres decorated with well-controlled sizes of Au NPs having uniform distribution over the TiO_2 surface. (B-D) SEM images of TiO_2-Au colloidal spheres that were obtained after the first (B, TiO_2-Au1), second (C, TiO_2-Au2) and third (D, TiO_2-Au3) deposition steps. The scale bars in the insets correspond to 100 nm.

5.3 Optical characterisation

We start with measuring both the absorption and PL spectra for TiO_2 and all three TiO_2-Au samples. The samples (TiO_2, TiO_2-Au1, TiO_2-Au2 and TiO_2-Au3) were first diluted in deionised water to achieve an optical density of ~ (0.2 to 0.5) and placed in cuvettes to be optically characterised. Figure 5.2 (a) and (b) show the steady state absorption and PL spectra for all the samples, respectively. In order for the relative contribution of the Au NPs to be emphasised in Figure 5.2 (a), each spectrum has been normalised to zero at 700 nm and to 1 at 370 nm as the absorbance of the TiO_2 at these wavelengths is known to be

dominant [3]. Furthermore, the absorption of the Au NPs at 370 nm is almost the same as 470 nm, as shown in Figure 5.3 (taken by Dr. Marina A. Leontiadou); similar absorption spectrum behaviour for Au NPs has been already reported [4]. That means that if there is an absorption by the Au NPs species in the system, we know that it is almost the same for 370 nm and 470 nm (the wavelengths used for photo-excitation in the experiment).

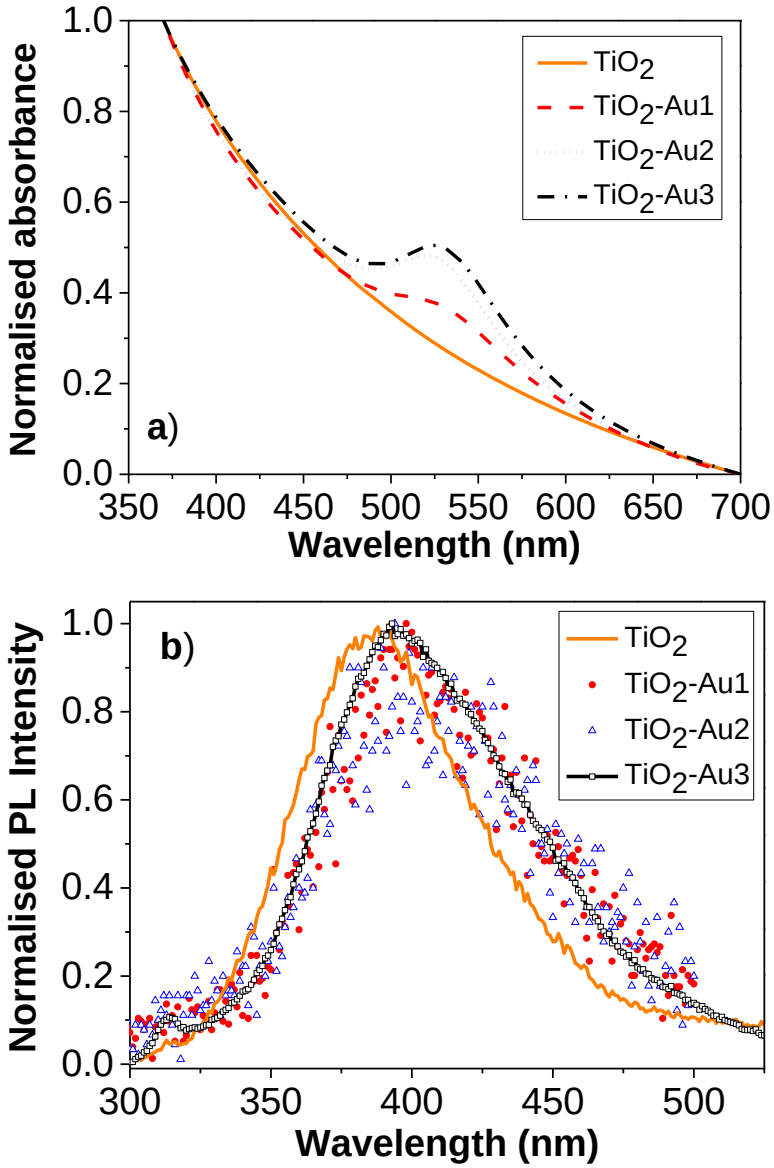

Figure 5.2 ***(a)*** *Normalised absorbance and* ***(b)*** *PL spectra of TiO_2 and TiO_2-Au NP samples.*

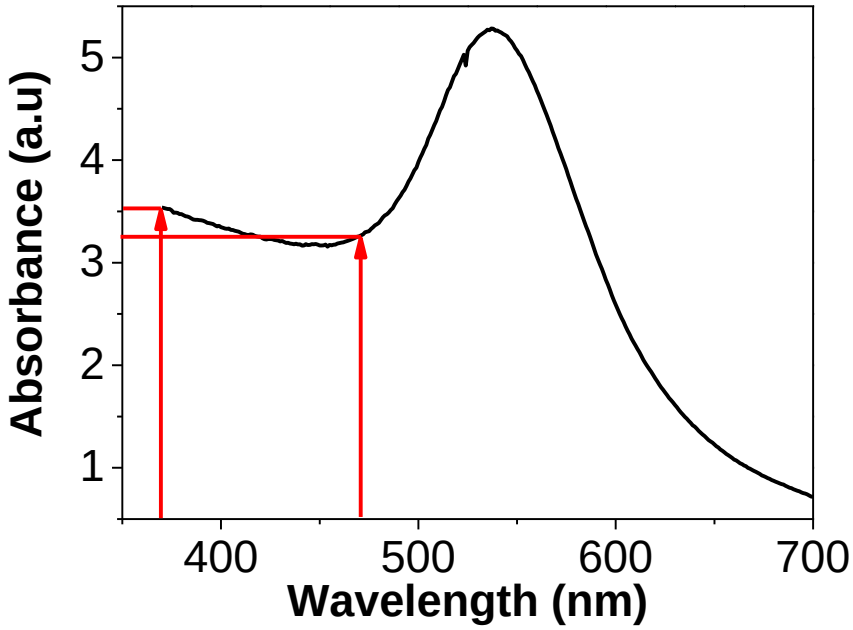

Figure 5.3 Steady state absorption spectrum of Au NPs. Red arrows show the 370 nm and 470 nm wavelengths.

It can be seen that an absorption peak is evident in Figure 5.2 (a) for the TiO_2-Au samples centred at ~530 nm, corresponding to the peak seen for the Au NPs on their own (as shown in Figure 5.3) and attributed to the plasmon resonance [5]; apart from that, a rise in absorption is seen with the decrease of wavelengths. In contrast, the feature at 530 nm cannot be seen for the TiO_2 only sample, indicating that these features are due to the presence of the gold NPs in the system. The PL spectra shown in Figure 5.2 (b) have a FWHM of ~75 nm and feature a broad peak centred at about 387 nm which corresponds to band edge recombination in TiO_2 whereas it shifts to about 395 nm on the addition of the Au-NPs. The red-shift in the position of the PL peak on the addition of the Au is consistent with the equilibration of the Fermi levels when exciting with UV light, as reported in the literature [5]. The PL intensity was significantly weaker for the TiO_2-Au1 and TiO_2-Au2 than for the TiO_2 sample, seen in the normalised data as an increase in the fluctuation of their signal in Figure 5.2 (b) which is attributed to electron injection into the Au NPs, leading to a reduction in the recombination at the band edge of TiO_2. In comparison, the PL spectrum for TiO_2-Au3 is more intense than for the other TiO_2-Au samples which is seen as a less noisy

normalised spectrum and this is consistent with reducing the shift of Fermi level for larger NP diameters reported previously [5], making the injection of the electron less energetically favourable at equilibrium. The absorption spectrum of the TiO_2 shown in Figure 5.2 (a) is extended beyond its band edge energy due to a scattering from the colloidal TiO_2 spheres with a diameter of ~220 nm and also because of nitrogen, N^-, and fluorine, F^-, impurities [6].

Figure 5.4 shows the pump-induced transmittance change, $\Delta T/T$, spectra for the TiO_2 and TiO_2-Au samples taken at the time immediately after pumping when the change is a maximum for excitation at a wavelength of 370 nm with an average pump power of 1 mW. It can be seen that the TiO_2 spectrum shows no response over this spectral region while the TiO_2-Au1, TiO_2-Au2 and TiO_2-Au3 spectra have features observed over the spectral region corresponding to the plasmonic absorption peaks i.e. ~530 nm (see Figure 5.2 (a)). Note that no change in the form of the spectra was observed after repeated measurement.

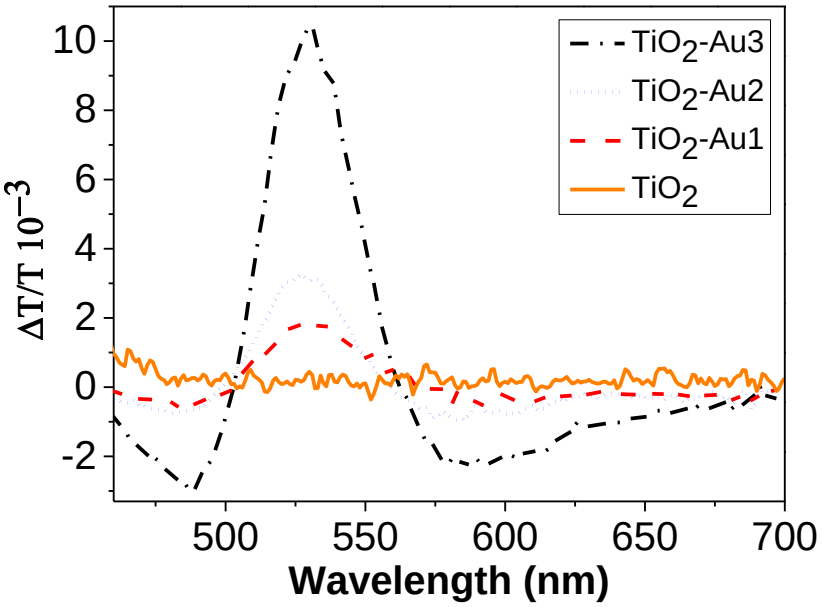

Figure 5.4 Pump-induced transmittance change, ΔT/T, spectra of TiO_2 colloidal spheres and TiO_2-Au samples for a 370 nm excitation wavelength and an average pump power of 1 mW (measured at the position of the sample). Each spectrum took approximately 30 minutes to collect.

The spectra for the TiO_2-Au samples comprises a bleach peak over the region from 500 nm to 560 nm centred at the plasmon resonance combined with two regions of photo-induced absorption (PA) to either side of the bleach. The PA is evident from approximately 560 nm to 700 nm and for wavelengths shorter than 500 nm. Such an overall shape has been previously observed in directly-excited Au NPs [7-12] and also in samples where gold is combined with CdS [9, 10, 13]. For example, when gold NPs were photoexcited by a 400 nm pump beam and probed at the plasmon resonance, the broadening of the surface plasmon band occurred as a bleach superimposed with two wings of absorption features at shorter and longer wavelengths [10, 11]. The features in general are attributed to the increase in electron temperature produced either by direct photoexcitation of the Au or by photoexcitation of the CdS followed by electron injection into the Au NPs. What happens here is that the high temperature of the electrons spectrally broadens the plasmonic response, leading to a reduction in the absorption at the peak (producing the observed bleach) and it increases the absorption at the wings (resulting in the PA clearly seen) [10, 11].

A recent study has used ultrafast transient absorption spectroscopy to test the electron injection dynamics from gold NPs to the conduction band of TiO_2 films when probing at 3440 nm [14]. Interestingly, they claimed that interband transition from the d-band to the sp-band in the gold overlaps with the plasmon band at the peak. Hence, the spectra shown in Figure 5.4 could be due to interband transitions in gold NPs generated by direct photoexcitation; however, this explanation can be ruled out in our case. First, the holes in the d-band of a gold NP can recombine with the excited electrons in a very fast time scale of tens of fs [11, 15] due to the high density of electrons in the conduction band [11] while the spectra shown were taken after few ps of pumping. Second, this time is much faster than the duration of the laser pulses used in our system (~100 fs) which makes it impossible to detect here if it is due to interband transitions in gold NPs. Moreover, absorption at 370 nm by the

TiO_2 is significant, as already discussed and shown in Figure 5.2 (a). Also, the absorption at 370 nm and 470 nm by the Au NPs is already stated as nearly the same. Therefore, to confirm that the absorption by the TiO_2 is primarily accountable for the observed transient transmittance changes in our case, the samples were also pumped at 470 nm at the same power. The 470 nm wavelength is closer to the plasmon resonance feature, hence if direct absorption of photons by the Au NPs is important then a larger response would be expected. Figure 5.5 shows the resultant pump-induced transmittance change spectra of TiO_2-Au samples taken with 470 nm excitation wavelength. Clearly, the response to 470 nm pumping is reduced for all samples compared to that found for 370 nm pumping, for example, reduced by a factor of two for the TiO_2-Au3 sample. This is instead consistent with the reduced absorbance by the TiO_2 at this wavelength (see Figure 5.2 (a)) and demonstrates that we are largely photo-exciting the TiO_2 in this experiment. As a result, we attribute the observed excitation of the Au NPs to the capture of electrons that were initially created in the TiO_2.

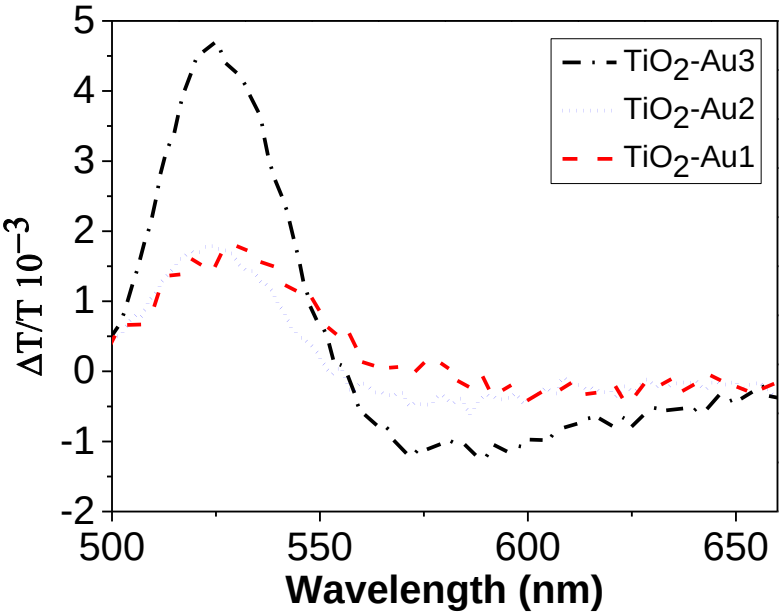

Figure 5.5 Pump-induced transmittance change spectra of TiO_2-Au samples taken with 470 nm excitation wavelength. The power intensity of the pump beam was 1mW at the position of the sample. Each spectrum took approximately 30 minutes to collect.

5.4 Ultrafast charge dynamics

Previous studies [7-12] have shown that the amplitude of the plasmonic response in Au NPs broadly changes while the spectral shape does not change with time and hence the behaviour of its transient can be investigated by measuring the pump-induced transmittance change at a single wavelength. Figure 5.6 (a) shows in a 300 ps window the fractional transmittance changes, $\Delta T/T$, transients for the TiO_2-Au2 sample when induced by different pump powers of 0.2 (pink), 0.4 (blue), 0.7 (red) and 1mW (black) using 370 nm and 530 nm as pump and probe wavelengths, respectively.

The decay of the pump-induced transmittance transients shown in Figure 5.6 (a) consists of two decay components at all the different powers, here called fast and slow. We can see from Figure 5.6 that the majority of the decay is associated with the fast component. The increment in path length difference between the pump and probe beams used here was 0.5 mm and corresponds to a time-resolution of ~3.3 ps which is suitable for the slow decay component. However, if the fast decay component is to be investigated, then a higher resolution is required. Figure 5.6 (b) shows the early stage of the transient at 1 mW pump power recorded at higher temporal resolution when the delay stage is set at 0.1 mm, which corresponds to less than 1 ps (~0.67 ps). An exponential fit to this high resolution early part of the decay yields a time constant of 2.3±0.1 ps for the fast component. To extract the time constant for the slow decay component, a global fit of a bi-exponential decay function was used to fit the longer time-scale transients shown in Figure 5.6 (a), but here using the 2.3 ps value for the fast component time constant which then yielded a slow component time constant of 107±5 ps. These two time constants fit and describe very well the decays for each pump power of the transients shown in Figure 5.6 (a).

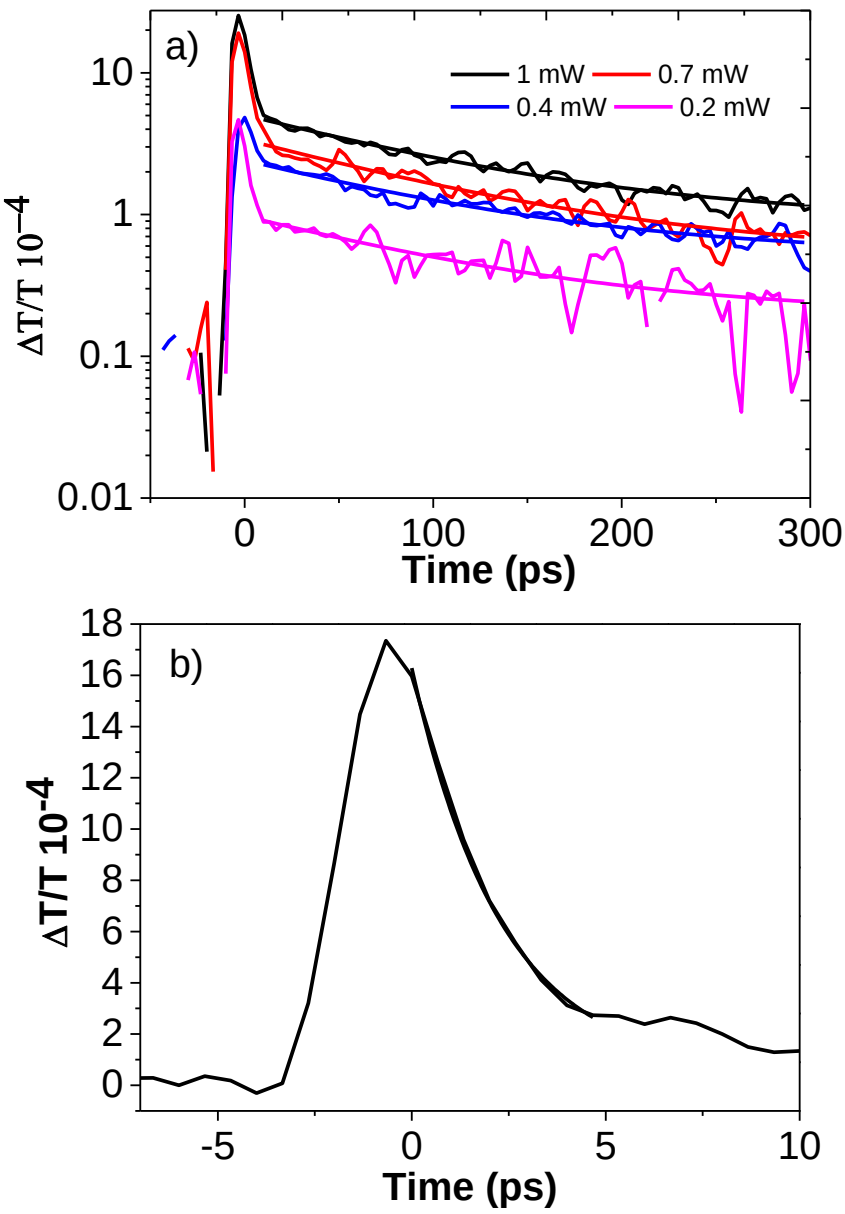

Figure 5.6 a) Transmittance transients for TiO_2-Au2 sample when induced by 370 nm pump beam and 530 nm probe beam for different pump powers as shown in the legend. Each of the transients shown is the average of nine scans and the delay line step size was 0.5 mm. Solid lines are the global fit to the transients and the time constants are 2.3±0.1 ps and 107±5 ps. b) The initial part of the transient at 1 mW when using small delay step sizes of 0.1mm between the pump and probe beams. Solid line represents the fit.

Similarly, Figure 5.7 shows the transmittance transients induced by different pump powers shown in the legends for (a) TiO_2-Au1 and (b) TiO_2-Au3 samples. In each case, the pump and probe beams were 370 nm and 530 nm, respectively. A similar procedure to that used for the TiO_2-Au2 sample was also used to determine the time constants for the fast and

slow components of the decays, here yielding time constants of 2.1±0.1 ps and 49±3 ps, respectively for the TiO_2-Au1 sample, and 2.3±0.1 ps and 128±6 ps for the TiO_2-Au3.

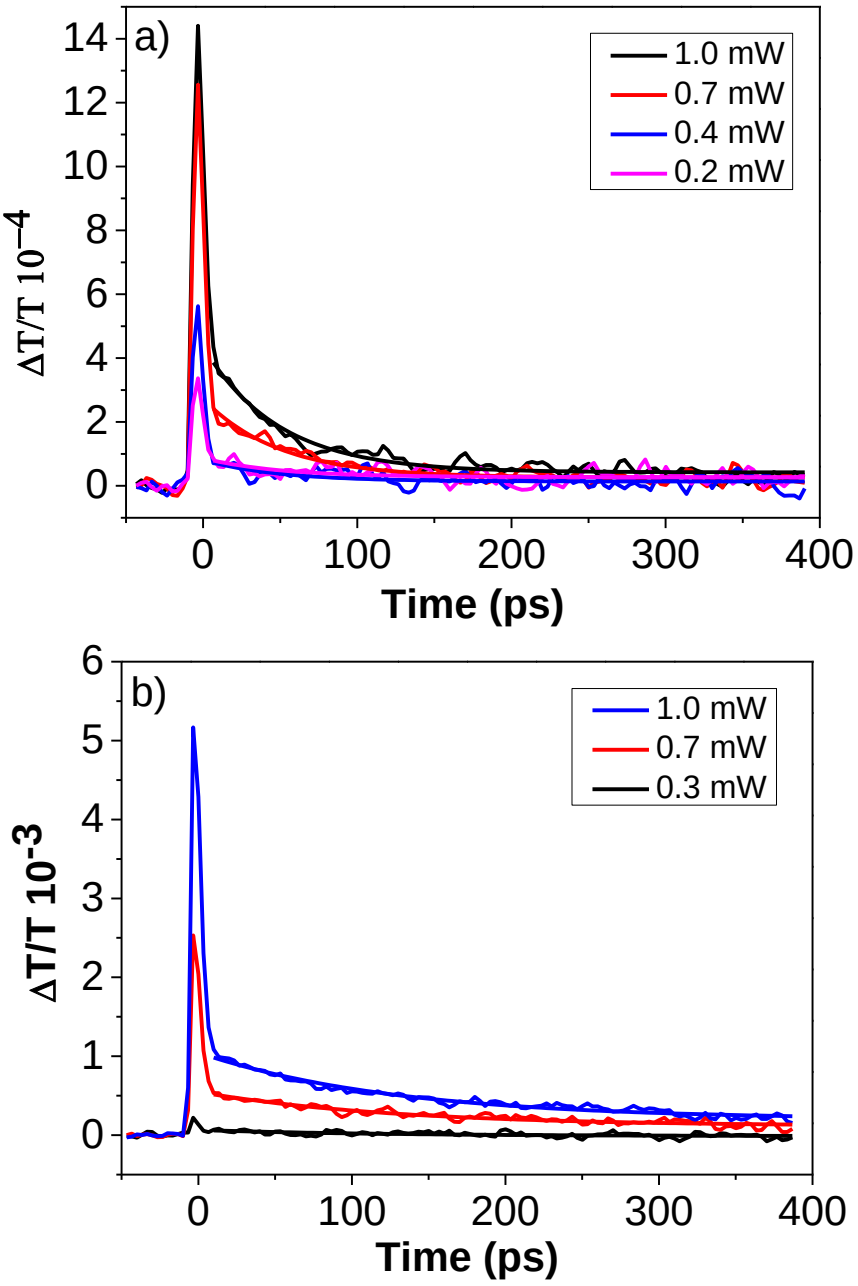

Figure 5.7 Transmittance transients when probing at 530 nm induced by 370 nm wavelength of different pump powers shown in the legends for (a) TiO_2-Au1 sample with time constants of 2.1±0.1 ps and 49±3 ps, and (b) TiO_2-Au3 sample with time constants of 2.3±0.1 ps and 128±6 ps. Solid lines are the global fit to the transients.

All the transients shown above were obtained for vigorously stirred samples at ~1000 rpm. However, our observations revealed that the shape of the pump-induced transmittance transients is independent of the stirring and hence also the time constants extracted from

them. Figure 5.8 shows an example of comparison between transients transmittance obtained for stirred and static samples of a) TiO_2-Au3 using a low pump power of 0.4 mW and b) TiO_2-Au2 using a high pump power of 1.5 mW.

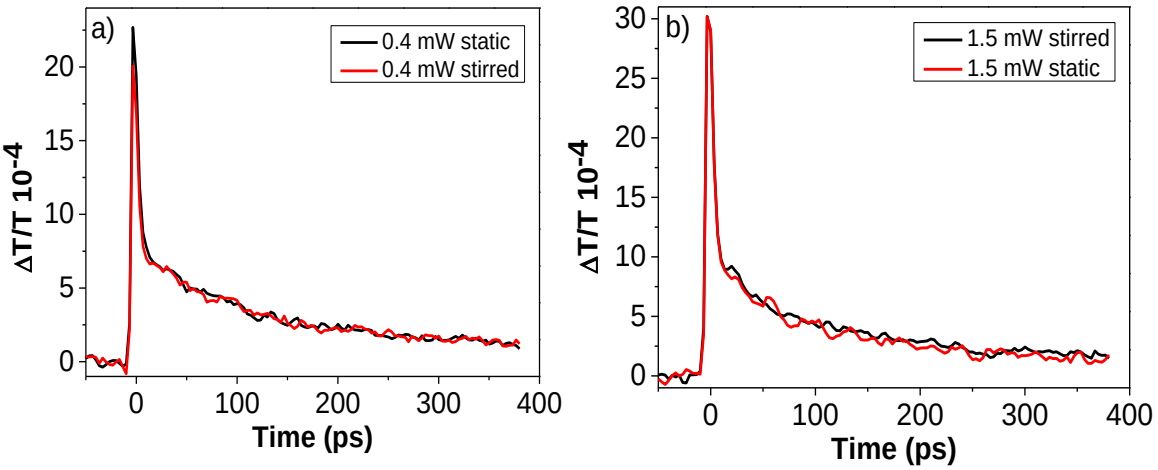

Figure 5.8 Comparison of transmittance transients of stirred and static samples induced by 370 nm at the bleach for a) TiO_2-Au3 using low pump power of 0.4 mW and b) TiO_2-Au2 using high pump power of 1.5 mW.

The three samples' transient decays are compared in Figure 5.9 and the rise of their bleaches at 530 nm are shown in detail in Figure 5.10. Clearly, the rise is completed in about 1 ps in each case and there is no significant variation between the three samples.

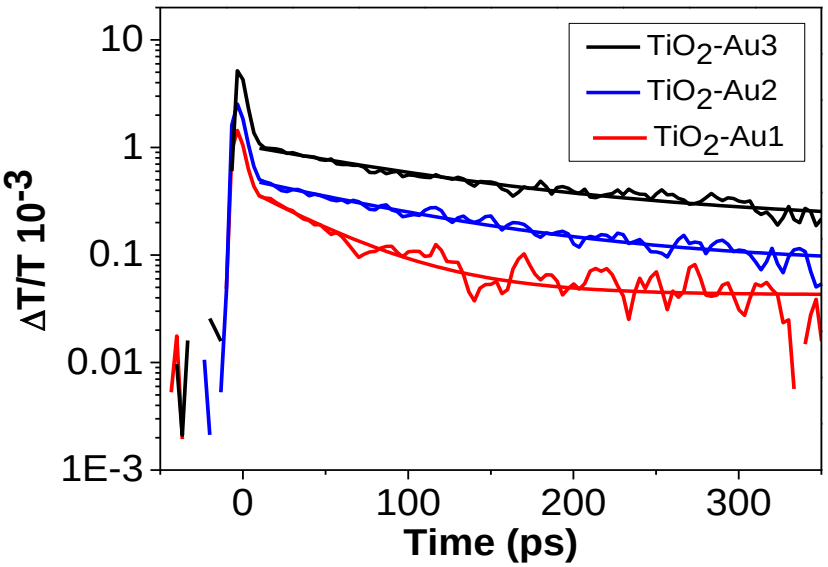

Figure 5.9 Comparison of transmittance transients obtained for different samples of TiO_2-Au when pumped by an average power of 1 mW at a wavelength of 370 nm.

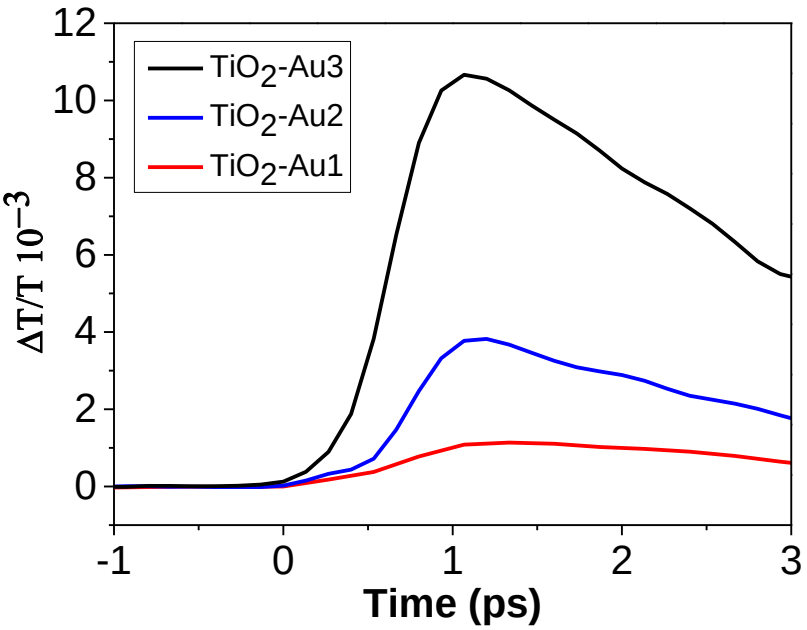

Figure 5.10 Initial rise time of the bleach at 530 nm for TiO_2-Au samples using a 370 nm excitation wavelength.

When a metal, in particular Au NPs, is involved in the sample studied then the changes induced by the pump pulses in a UTA experiment are due to changes of temperature as electrons cool by a three-step process [9, 11, 14]. In other words, the recovery of the bleach directly monitors the dynamics of these three steps. Initially, hot electrons are created either by direct photo-excitation of the NP or by injection from elsewhere, and these electrons undergo electron-electron scattering over a period on the order of 100 fs. This results in an elevated electronic temperature and thus a change in the plasmonic response, as has been previously described. The subsequent step for the electron gas is to cool by electron-phonon scattering on a time-scale of (1-10 picoseconds). Finally, the heat is dissipated to the surrounding materials over ~100 ps.

The rise of the bleach signal in all the transients obtained above is attributed to the charge injection process from the TiO_2 to the Au NPs. However, the lack of variation in the initial rise time of the bleach between the samples shown in Figure 5.10 indicates that charge injection is independent of the size of the Au NPs over this range and under the experiment conditions. Now we can relate the three-step cooling process to our transients. First, the

electron-electron process occurs on a similar time-scale to the duration of our pump and probes pulses (~100 fs) and so is not resolvable in this experiment. In contrast, the resolution of our experiment enables us to detect both electron-phonon and heat dissipation, which are represented by the fast and slow decay components observed in the transmittance transients, respectively. From the results seen in Figure 5.6 and Figure 5.7 we conclude that there is no significant difference in the rate of electron-phonon scattering, represented by the fast decay, between the samples; however, the heat dissipation lifetime does change appreciably. We have already mentioned that the average diameters were found to be 12.2±2.2 nm, 19.3±2.3 nm and 24.5±2.8 nm for samples TiO_2-Au1, TiO_2-Au2, and TiO_2-Au3, respectively, hence we can study how the time constant associated with heat dissipation varies with the NP diameter in the TiO_2-Au system. Figure 5.11 illustrates how the Au nanoparticle diameter is related to the heat dissipation lifetime in the samples under study. Therefore, we can conclude that the rate of heat dissipation, by which the energy associated with the electrons injected from the TiO_2 is dissipated, is reduced by increasing the size of the Au NPs.

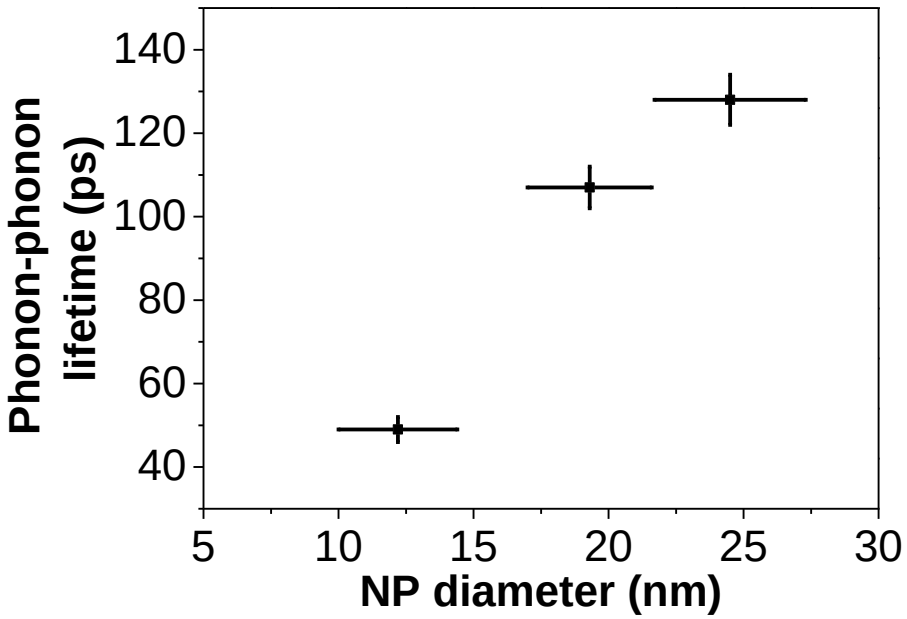

Figure 5.11 Phonon-phonon time constant against NP diameter in TiO_2-Au samples.

As we have already done with pump-induced transmittance change spectra of TiO_2-Au samples when we used a 470 nm excitation wavelength as a point closer to the plasmon resonance, here also we study the transmittance transients of TiO_2-Au samples, probing at 530 nm and photo-exciting with 1 mW pump power of 470 nm wavelength. An example of the transmittance transients for TiO_2-Au2 sample is shown in Figure 5.12. The time constants obtained for the 370 nm case were found to fit very well with the 470 nm one under the conditions of the experiment.

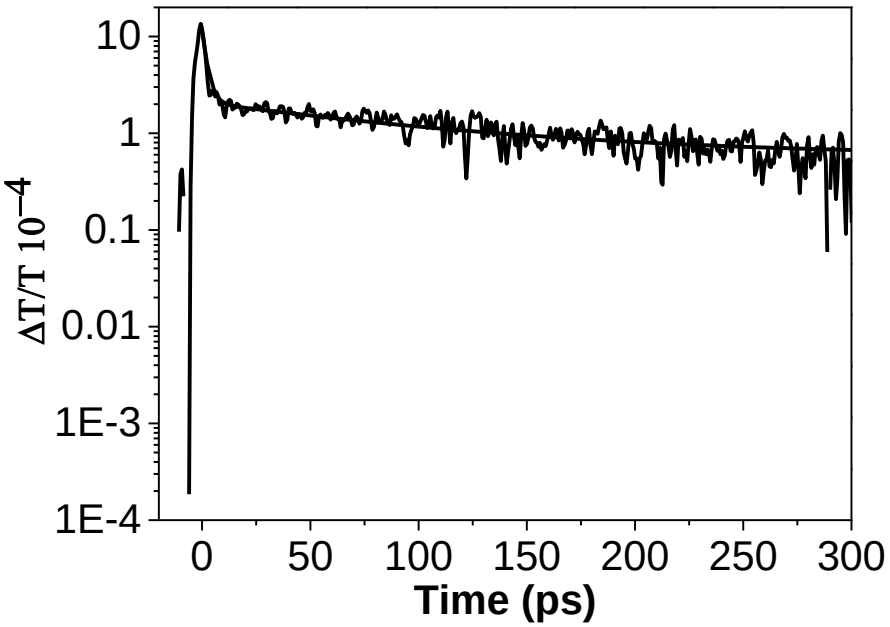

Figure 5.12 Transmittance transients for TiO_2-Au2 sample when induced by 470 nm pump beam with bi-exponential fit shown with time constants of 2.3 ps and 107 ps.

Moreover, the rise time in each sample at both excitation wavelengths, 370 nm and 470 nm, was also investigated. Figure 5.13 compares the initial rise of the bleach for the TiO_2-Au1 sample at 530 nm when photo-excited with 370 and 470 nm wavelengths. These measurements were obtained at high resolution as the delay stage was set to 0.04 mm which is equivalent to ~267 fs. No difference can be seen in Figure 5.13 between the rises of the two transients, and similar results were obtained for other samples (in some cases there were tens of fs differences which is within the pulse duration of the experiment). Our observations confirmed that the amplitude of the transient at 370 nm is always larger than that of 470 nm

at all cases and for all samples, except the one shown in Figure 5.13 which is attributed to mis-centring the pump beam spot at the probe beam when setting the experiment for measurements. Therefore, this emphasises that the response of the TiO_2-Au samples has a significant contribution due to direct absorption by the TiO_2.

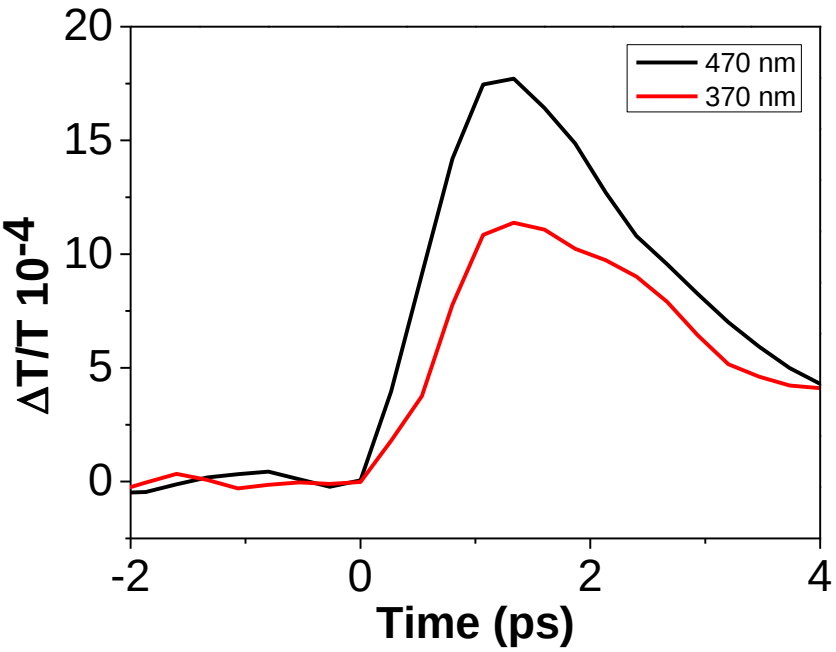

Figure 5.13 Initial bleach rises for TiO_2-Au1 sample at 530 nm when photo-excited with 370 and 470 nm wavelengths.

All the above results and observations allow us to draw some conclusions about the effect of NP size on photo-catalytic activity. Here, the ability of the Au NPs to capture photo-generated electrons efficiently from the TiO_2 plays an important role in the successful usage of colloidal TiO_2 spheres decorated with Au NPs as a photo-catalyst. However, studies demonstrated that electrons can also be efficiently transferred from Au NPs to the TiO_2 following direct photo-excitation of the Au NPs at the plasmonic resonance [14]. This electron transfer from the NPs to the TiO_2 can occur within 50 fs, which could be before or during the electron-electron scattering phase [14]. Therefore, if a high electron capture yield by the Au NPs is required, then the rate of electron cooling should be higher than that of the re-injection of captured electron back into the TiO_2 and, at this limit, any change in NP size

that notably influences the cooling of electrons might determine the optimum NP diameter. Here, however, we have shown that the rate of electron-electron and electron-phonon scattering is not significantly affected by NP diameter over this size range while the rate of heat dissipation is affected. Furthermore, we have seen in Figure 5.6, Figure 5.7 and Figure 5.9 that most of the injected energy is lost by electron-phonon scattering, represented by the large relative amplitude of the fast decay components compared to the small amplitude of the slow component associated with heat dissipation. Hence, although the rate of heat dissipation is dependent on the Au NP diameter, the electrons have largely cooled when it becomes a significant process. Therefore, heat dissipation is not likely to affect the yield of electron capture and so the choice of NP diameter in this size range is not restricted by electron cooling rate considerations. This enables NP size to be optimised for other properties such as storing captured electrons.

5.5 Summary

The plasmon bleach recovery in TiO_2 colloidal spheres decorated with different sizes of Au NPs has been studied using ultrafast transient absorption spectroscopy. The pump-induced transmittance change spectra obtained immediately after pumping have shown a broadening of the surface plasmon band resulting in bleaches at the plasmon band maximum superimposed with two wings of absorption features at shorter and longer wavelengths. Furthermore, the transmittance transients were well-described by bi-exponential decay with a very quick decline of a few ps associated with electron–phonon scattering, followed by a slower decay over a few tens of ps associated with heat dissipation. Of the electron cooling steps, only the heat dissipation rate was found to be dependent on the size of the Au NPs; however, it was found to be a minor component of the overall electron cooling process and hence does not place a restriction on NP size.

5.6 References

1. Al-Otaify, A., et al., *Size dependence of ultrafast charge dynamics in monodisperse Au nanoparticles supported on TiO2 colloidal spheres.* Physical Chemistry Chemical Physics, 2014. **16**(27): p. 14189-14194.
2. Damato, T.C., et al., *A Facile Approach to TiO2 Colloidal Spheres Decorated with Au Nanoparticles Displaying Well-Defined Sizes and Uniform Dispersion.* Langmuir, 2013. **29**(5): p. 1642-1649.
3. Subramanian, V., E. Wolf, and P.V. Kamat, *Semiconductor−Metal Composite Nanostructures. To What Extent Do Metal Nanoparticles Improve the Photocatalytic Activity of TiO2 Films?* The Journal of Physical Chemistry B, 2001. **105**(46): p. 11439-11446.
4. Link, S. and M.A. El-Sayed, *Size and temperature dependence of the plasmon absorption of colloidal gold nanoparticles.* Journal of Physical Chemistry B, 1999. **103**(21): p. 4212-4217.
5. Subramanian, V., E.E. Wolf, and P.V. Kamat, *Catalysis with TiO2/Gold Nanocomposites. Effect of Metal Particle Size on the Fermi Level Equilibration.* Journal of the American Chemical Society, 2004. **126**(15): p. 4943-4950.
6. Li, Q. and J.K. Shang, *Self-Organized Nitrogen and Fluorine Co-doped Titanium Oxide Nanotube Arrays with Enhanced Visible Light Photocatalytic Performance.* Environmental Science & Technology, 2009. **43**(23): p. 8923-8929.
7. Ahmadi, T.S., S.L. Logunov, and M.A. El-Sayed, *Picosecond Dynamics of Colloidal Gold Nanoparticles.* The Journal of Physical Chemistry, 1996. **100**(20): p. 8053-8056.
8. Aruda, K.O., et al., *The role of interfacial charge transfer-type interactions in the decay of plasmon excitations in metal nanoparticles.* Physical Chemistry Chemical Physics, 2013. **15**(20): p. 7441-7449.
9. Kamat, P.V., *Photophysical, Photochemical and Photocatalytic Aspects of Metal Nanoparticles.* The Journal of Physical Chemistry B, 2002. **106**(32): p. 7729-7744.
10. Khon, E., et al., *Suppression of the Plasmon Resonance in Au/CdS Colloidal Nanocomposites.* Nano Letters, 2011. **11**(4): p. 1792-1799.
11. Link, S. and M.A. El-Sayed, *Shape and size dependence of radiative, non-radiative and photothermal properties of gold nanocrystals.* International Reviews in Physical Chemistry, 2000. **19**(3): p. 409-453.
12. Logunov, S.L., et al., *Electron dynamics of passivated gold nanocrystals probed by subpicosecond transient absorption spectroscopy.* Journal of Physical Chemistry B, 1997. **101**(19): p. 3713-3719.
13. Mongin, D., et al., *Ultrafast Photoinduced Charge Separation in Metal–Semiconductor Nanohybrids.* ACS Nano, 2012. **6**(8): p. 7034-7043.
14. Du, L., et al., *Ultrafast plasmon induced electron injection mechanism in gold–TiO2 nanoparticle system.* Journal of Photochemistry and Photobiology C: Photochemistry Reviews, 2013. **15**(0): p. 21-30.
15. Pawlik, S., M. Bauer, and M. Aeschlimann, *Lifetime difference of photoexcited electrons between intraband and interband transitions.* Surface Science, 1997. **377–379**(0): p. 206-209.

Chapter 6 Summary, conclusions & future work

6.1 Summary and conclusions

The ultrafast charge dynamics in a number of nanostructured materials relevant to the production of renewable energy were investigated using ultrafast transient absorption spectroscopy. The materials investigated could have applications either in next-generation solar cells or as photocatalysts for photolysis of water.

An investigation of the absorption spectra of HgTe QDs passivated with MPA, 1-thioglycerol and DDT ligands, coupled with the spectra calculated by the tight-binding model similar to that used in [1], has allowed us to draw the following conclusions. The band edge transition was found to be very weak in these QDs and was obscured by the stronger next highest transition. The peak of the absorption shoulder was attributed either to a transition from VBM to CBM-1 or to a CBM transition, but from deeper within the valance band, and a comparison with the literature [1-3] has allowed us to estimate the diameter of these QDs to be in the range of 3–4 nm.

Ultrafast transient absorption spectroscopy has been used to study the charge dynamics for HgTe QDs. The pump-induced transmittance change spectra shape has varied depending on the ligands used for passivation. An MPA-capped HgTe QD spectrum has shown strong bleach evident at wavelengths corresponding to the absorption shoulder peak with no sign of any PA. At low pump fluences and for well-stirred samples, the transmittance transients were found to be free of any trion formation, as biexciton recombination governed the decay observed for these QDs. However, at high pump fluences or for unstirred samples, another process combined with biexciton recombination was found to contribute to the decay, and was identified as a photo-charging process.

In comparison, the differential spectra of thioglycerol-capped HgTe QDs have shown a broad PA increase superimposed with a bleach at the band gaps of the samples, which was attributed to state filling. The transmittance transients of these QDs at different pump wavelengths and powers have shown two different behaviours: one at the bleach described by bi-exponential decay, and the other away from it and described by a mono-exponential decline. The decay lifetimes of these features, in addition to the broad PA feature, were found to be consistent with surface charge trapping observed in CdSe CQDs [4]. Furthermore, no sign of long-lived surface trapping was found from the comparison of the fractional transmittance transients of stirred and unstirred samples.

The DDT-capped HgTe QDs have been considered as a case in between the two other samples. There was a drop in the differential spectrum just before the bleach attributed to PA. The decay lifetime obtained for these QDs was shorter than that obtained for the MPA-capped HgTe QDs, while they had a longer PL wavelength and, therefore, should have had a longer lifetime. The lifetime was found to be similar to that for thioglycerol-capped QDs, which, in addition to the above reasons, has enabled us to attribute the decay of the transients here to direct surface trapping.

This study has suggested that the carboxylic acid group in MPA is the reason behind having better passivation in MPA-capped HgTe QDs. Each of the three ligands used has the ability to donate electron density to the QD surface to passivate the traps associated with unsaturated Hg bonds through their deprotonated thiol groups. However, this ability is enhanced by the additional deprotonated carboxylic acid group in MPA, which increases the overall negative charge on the ligand. The resultant greater ability to donate negative charge is consistent with the greater zeta potentials reported for QD-ligand complexes passivated by thioacids, such as MPA, relative to thiols. This greater negative charge donation supresses surface states and the non-radiative processes associated with surface states. The study has

also shown that MEG cannot be reliably measured if there is a sign of any surface-related processes, i.e. how MEG can be overestimated if surface trapping-related processes were ignored. Therefore, we limited MEG measurement to MPA-capped QDs. Our analysis has allowed the determination of MEG for the first time in HgTe QDs, giving the quantum yield a value of 1.36±0.04 for excitation at $3.1E_g$. MEG performance of these QDs was found to have advantages over Pb-chalcogenide QDs and InP QDs, in addition to the possibility of size tunability over the optimum range for exploitation of the solar spectrum and insensitivity to water and air exposure.

$Cd_xHg_{(1-x)}Te$ alloy QDs have been studied for their ultrafast exciton dynamics using a UTA experiment. The investigation of the pump-induced transmittance change spectrum has shown two features at the shoulder position of the steady state absorption and at the PL peak. Exciton dynamics have been studied using four different wavelengths, of which two were above the expected MEG threshold. The transients have been found to be free of any photo-charging or trion recombination. The assessment of MEG in these alloy QDs suggested the attribution of the decay of the transients obtained above the MEG threshold to biexciton recombination due to MEG for the well-stirred samples at low pump powers. It has revealed a quantum yield of 1.12±0.01 when photo-exciting with 2.6 times the band gap. The study resulted in a measurement of the quantum yield of MEG with higher accuracy than previously reported, in addition to the investigation of the stirring effect and the measurement of the relaxation time to the band edge.

Finally, our measurements for TiO_2 colloidal spheres decorated with different sizes of Au NPs have shown absorption peaks at ~530 nm for the TiO_2-Au samples, corresponding to the plasmon band. The UTA experiment has been used to study the plasmon bleach recovery in these materials. The differential spectra obtained immediately after pumping the samples with 370 nm and 470 nm have shown a broadening of the surface plasmon band,

resulting in a bleach at the plasmon band maximum superimposed with two wings of absorption features at the sides. The shape of the transmittance transients was well described by bi-exponential decay with two components: a very quick decline of a few ps, followed by a slower decay over a few 10s of ps. The former was associated with electron–phonon scattering, while the latter was associated with heat dissipation as the electron–electron scattering was not detected in our experiment. Only the heat dissipation rate of the three electron cooling steps was found to vary with the size of the Au NPs. However, it represented just a minor component of the overall transients obtained; therefore, we did not place a restriction on NP size.

6.2 Future work

Proceeding from the results obtained throughout the whole thesis, here we outline some possible future works. It is known that the surface of the QDs plays an important role in the relaxation dynamics of excitons [5, 6], allowing surface-related processes which have lifetimes similar to that of MEG, not only to compete with MEG but also to be mistaken for MEG, leading to an overestimation of its quantum yield. This issue has affected different QD materials, such as CdSe, CdTe [7], InAs [8, 9], and InAs/CdSe/ZnSe core/shell1/shell2 [10]. However, passivation of the QDs is capable of reducing the possibility of trapping hot charges to the surfaces [4, 11-13], giving advantages to other relaxation routes, including MEG. We have already seen in this thesis how HgTe QDs showing significant surface trapping, i.e. those with 1-thioglycerol and DDT ligands, do not exhibit measureable MEG, whilst the well-passivated MPA-capped QD does. This suggests that further improving passivation by capping HgTe QDs with a CdS or ZnS shell [14] could reduce ultrafast trapping, consequently improving the efficiency of MEG in HgTe QDs.

A further forward step in the study of the ultrafast dynamics of HgTe QDs is to examine a type-II heterostructure. A recent thesis by Dr. Musa Cadirci [15] has shown that the efficiency of MEG has been improved by a factor of 3 in type-II CdSe/CdTe/CdS and CdTe/CdSe/CdS core/shell1/shell2 systems and CdTe/CdS core/shell systems, compared with previously reported studies [16-18]. This improvement was attributed to two factors. Firstly, the type-II heterostructure reduces the electron–hole overlap and, therefore, the Auger cooling rate, which competes with MEG. Secondly, consistent with the point made above, the CdS shell was found to result in the suppression of surface trapping of hot carriers, which competes with MEG. Finally, using these QDs in solar cells also needs investigation to identify what efficiency could be obtained using them in practise.

Regarding $Cd_xHg_{(1-x)}Te$ alloy QDs, it is known that both the band gap and the split-off energies change with composition variation [19], which, at a certain point, become equal, and charge multiplication can be favoured [20]. Further work needs to be done in the search for the composition point at which the two energies are in resonance for numbers of QD sizes. The measurements of MEG here could allow the determination of the best combination of sizes and compositions to optimise the exploitation of the solar spectrum. Finally, we have seen from the ultrafast charge dynamics of the plasmon band maximum that the heat dissipation rate varied with the size of the Au NPs in TiO_2-Au systems. However, the investigation of both electron–electron and electron–phonon scattering could be achieved with a UTA experiment of higher time resolution, which could be a direction for future study.

6.3 References

1. Allan, G. and C. Delerue, *Tight-binding calculations of the optical properties of HgTe nanocrystals.* Physical Review B, 2012. **86**(16): p. 165437.
2. Kovalenko, M.V., et al., *Colloidal HgTe Nanocrystals with Widely Tunable Narrow Band Gap Energies: From Telecommunications to Molecular Vibrations.* Journal of the American Chemical Society, 2006. **128**(11): p. 3516-3517.
3. Lhuillier, E., S. Keuleyan, and P. Guyot-Sionnest, *Optical properties of HgTe colloidal quantum dots.* Nanotechnology, 2012. **23**(17): p. 175705.
4. Tyagi, P. and P. Kambhampati, *False multiple exciton recombination and multiple exciton generation signals in semiconductor quantum dots arise from surface charge trapping.* The Journal of Chemical Physics, 2011. **134**(9): p. 094706-10.
5. Nozik, A.J., *Spectroscopy and hot electron relaxation dynamics in semiconductor quantum wells and quantum dots.* Annual Review of Physical Chemistry, 2001. **52**(1): p. 193-231.
6. Peterson, M.D., et al., *The Role of Ligands in Determining the Exciton Relaxation Dynamics in Semiconductor Quantum Dots.* Annual Review of Physical Chemistry, Vol 65, 2014. **65**: p. 317-339.
7. Nair, G. and M.G. Bawendi, *Carrier multiplication yields of CdSe and CdTe nanocrystals by transient photoluminescence spectroscopy.* Physical Review B, 2007. **76**(8): p. 081304.
8. Pijpers, J.J.H., et al., *Carrier multiplication and its reduction by photodoping in colloidal InAs quantum dots (vol 111, pg 4146, 2007).* Journal of Physical Chemistry C, 2008. **112**(12): p. 4783-4784.
9. Pijpers, J.J.H., et al., *Carrier multiplication and its reduction by photodoping in colloidal InAs quantum dots.* Journal of Physical Chemistry C, 2007. **111**(11): p. 4146-4152.
10. Ben-Lulu, M., et al., *On the Absence of Detectable Carrier Multiplication in a Transient Absorption Study of InAs/CdSe/ZnSe Core/Shell1/Shell2 Quantum Dots.* Nano Letters, 2008. **8**(4): p. 1207-1211.
11. Bera, D., et al., *Quantum Dots and Their Multimodal Applications: A Review.* Materials, 2010. **3**(4): p. 2260-2345.
12. Kim, J.Y., et al., *25th Anniversary Article: Colloidal Quantum Dot Materials and Devices: A Quarter-Century of Advances.* Advanced Materials, 2013. **25**(36): p. 4986-5010.
13. Smith, C. and D. Binks, *Multiple Exciton Generation in Colloidal Nanocrystals* Nanomaterials, 2013. **4**(1): p. 19-45.
14. Li, L., et al., *Efficient Synthesis of Highly Luminescent Copper Indium Sulfide-Based Core/Shell Nanocrystals with Surprisingly Long-Lived Emission.* Journal of the American Chemical Society, 2011. **133**(5): p. 1176-1179.
15. Cadirci, M., *Ultrafast charge dynamics in novel colloidal quantum dots*, in *Faculty of Engineering and Physical ScienceSchool of Physics and Astronomy*. 2014, The University of Manchester: Manchester, UK. p. 202.
16. Gachet, D., et al., *An Upper Bound to Carrier Multiplication Efficiency in Type II Colloidal Quantum Dots.* Nano Letters, 2010. **10**(1): p. 164-170.
17. Schaller, R.D., et al., *High-efficiency carrier multiplication and ultrafast charge separation in semiconductor nanocrystals studied via time-resolved photoluminescence.* Journal of Physical Chemistry B, 2006. **110**(50): p. 25332-25338.

18. Kobayashi, Y., T. Udagawa, and N. Tamai, *Carrier Multiplication in CdTe Quantum Dots by Single-photon Timing Spectroscopy*. Chemistry Letters, 2009. **38**(8): p. 830-831.
19. Kershaw, S.V., et al., *Multiple exciton generation in cluster-free alloy CdxHg1-xTe colloidal quantum dots synthesized in water*. Physical Chemistry Chemical Physics, 2014.
20. Norton, P., *HgCdTe infrared detectors (Reprinted from Electrochem Soc. Proc., pg 48-70, 1999).* Opto-Electronics Review, 2002. **10**(3): p. 159-174.